Springer Theses
Recognizing Outstanding Ph.D. Research

Manuel Ross

Atomic Diffusion in Glasses Studied with Coherent X-Rays

Springer

Springer Theses

Recognizing Outstanding Ph.D. Research

Aims and Scope

The series "Springer Theses" brings together a selection of the very best Ph.D. theses from around the world and across the physical sciences. Nominated and endorsed by two recognized specialists, each published volume has been selected for its scientific excellence and the high impact of its contents for the pertinent field of research. For greater accessibility to non-specialists, the published versions include an extended introduction, as well as a foreword by the student's supervisor explaining the special relevance of the work for the field. As a whole, the series will provide a valuable resource both for newcomers to the research fields described, and for other scientists seeking detailed background information on special questions. Finally, it provides an accredited documentation of the valuable contributions made by today's younger generation of scientists.

Theses are accepted into the series by invited nomination only and must fulfill all of the following criteria

- They must be written in good English.
- The topic should fall within the confines of Chemistry, Physics, Earth Sciences, Engineering and related interdisciplinary fields such as Materials, Nanoscience, Chemical Engineering, Complex Systems and Biophysics.
- The work reported in the thesis must represent a significant scientific advance.
- If the thesis includes previously published material, permission to reproduce this must be gained from the respective copyright holder.
- They must have been examined and passed during the 12 months prior to nomination.
- Each thesis should include a foreword by the supervisor outlining the significance of its content.
- The theses should have a clearly defined structure including an introduction accessible to scientists not expert in that particular field.

More information about this series at http://www.springer.com/series/8790

Manuel Ross

Atomic Diffusion in Glasses Studied with Coherent X-Rays

Doctoral Thesis accepted by
University of Vienna, Austria

Springer

Author
Dr. Manuel Ross
Faculty of Physics
University of Vienna
Vienna
Austria

Supervisor
Prof. Bogdan Sepiol
Dynamics of Condensed Systems
University of Vienna
Vienna
Austria

ISSN 2190-5053 ISSN 2190-5061 (electronic)
Springer Theses
ISBN 978-3-319-28644-0 ISBN 978-3-319-28646-4 (eBook)
DOI 10.1007/978-3-319-28646-4

Library of Congress Control Number: 2015959930

Printed on acid-free paper

This Springer imprint is published by SpringerNature
The registered company is Springer International Publishing AG Switzerland

Parts of this thesis have been published in the following journal article:

Ross, M., Stana, M., Leitner, M., and Sepiol, B. 2014. Direct observation of atomic network migration in glass. *New J. Phys.,* **16**(9), 093042.

Supervisor's Foreword

The fundamental dynamics of glasses are often seen as one of the great unsolved problems of physics and understanding them on an atomic level has been a long-standing challenge in many scientific disciplines. For a long time, scientists have been developing methods to better understand structural and dynamic properties of this material class on this fundamental scale. Although the network description for the underlying components provided a good structural model, the dynamics stayed unclear. The importance of these structural changes is evident, as the dynamics of the basic network components of glasses can play a key role for many properties of this material class.

Very different from these small scales is the spatial extent of the machines, which turn out to be particularly suitable to study these very dynamics. Major experimental insight of this work has been obtained at the leading synchrotron facilities ESRF in Grenoble and PETRA III in Hamburg. These huge devices, which are embedded in large international research centres, easily span diameters of multiple hundreds of metres. Their unique property making them indispensable for this research is their ability to create radiation of very small wavelengths with a very high coherence. When the first dedicated coherent beamlines were proposed, scientists had the future vision in mind that one day, unravelling insight into atomic dynamics in glasses could become possible. Coherent X-ray measurements have been improved ever since by innovations in technological and methodological ways.

This work shows for the first time how such a study can be realized. It contributes significantly to the field of photon science, particularly to the synchrotron research of material properties of glasses. In the course of this research, the new method of *atomic-scale X-ray Photon Correlation Spectroscopy* (aXPCS) has been extended to the amorphous regime. This novel coherent technique has only recently been proven to be able to capture diffusion processes with atomic resolution in crystal systems. By extending and further developing this method and by establishing the method in glasses, this research brings together the two important

scientific disciplines of coherent synchrotron physics and fundamental glass research.

For this thesis, two prototypic glass systems have been chosen. As a first focus of study, lead glasses are known to undergo significant structural changes with composition. Accordingly, changes in dynamics are to be expected and unravelling details about them should help understand the causes for the changes in structure. Additionally, the mix of elements in this glass with a high electronic contrast makes them a very good material for a scattering technique like the applied approach. Therefore, this glass is an ideal material for the endeavour of establishing a new experimental method in the class of amorphous materials. The second object of study was the fascinating material type of fast ionic conductors. Glasses are typically known for being electrical insulators. However, in this type of glasses, electric conduction can be measured. Very differently from the predominant electronic conduction in, e.g. metals, the conduction process in this material is caused by the rapid movements of charges in the form of ions. As the charges are directly linked to the moving ions, studying atomic dynamics can give direct insight into the conduction process. This makes them a particularly rewarding object of study.

This work pushes forward the frontiers of science in three ways. First of all, the feasibility of atomic diffusion studies in glasses is demonstrated with highly coherent synchrotron radiation. Second, by showing that the method is also feasible at very low temperatures, atomic jump processes far below the glass transition temperature are evidenced. As a third key insight, the dependence of atomic diffusion speeds on the thermal history is shown for certain glass compositions. With this new means of studying atomic diffusion in amorphous systems, new insight into basic processes in a wide range of intriguing materials, such as fast ionic conductors, can be obtained. This opens up the door for a tailored adjustment of conductivities of fast ionic conductors. The obtained insight can help to further technically highly relevant solutions, particularly in the field of battery technologies.

Vienna
November 2015

Prof. Bogdan Sepiol

Abstract

Glasses have been known for thousands of years, yet their underlying properties stay enigmatic till today. Many efforts have been made to understand the structural and dynamic processes of these amorphous materials on the atomic level. Still, no experimental method has been able to capture glassy dynamics at this scale, rendering it impossible to gain a complete picture of the atomic transport processes. Here, a novel approach for gaining insight into the fundamental mechanisms governing glassy dynamics is demonstrated.

Various researchers have utilised the powerful new technique of XPCS to study dynamics in a range of amorphous systems and also in crystalline materials. While XPCS previously covered scales down to the nanometre range, recent efforts enabled direct study of diffusion on the fundamental atomic scale in crystals. The range of this new approach, coined as aXPCS, is extended to amorphous materials in this thesis.

As a first step, the feasibility of aXPCS measurements in amorphous systems is demonstrated in a binary glass former. Particularly, it is shown that lead diffusion in lead silicate glasses changes drastically for different mixing ratios of lead oxide. The diffusion process changes from single jump processes between clusters in a low lead concentrated glass to multiple jump processes along network paths and through voids in a high lead concentrated glass. Up until now, such measurements were out of reach for temperatures below the glass transition. The results of this thesis show that the method and the models applied can help in gaining deeper understanding of atomic diffusion in a wide range of amorphous systems.

As a second step, the diffusion in the technical relevant material class of amorphous fast ionic conductors is studied with aXPCS at low temperatures. It is shown that the diffusion speed of ions in a glass matrix can be influenced by the synthesis process. This implies that aXPCS is a viable tool for obtaining direct insight into dynamics on a scale not observable with other methods and for helping to improve various material properties.

Acknowledgements

First and foremost, I want to thank my supervisor Bogdan Sepiol. Bogdan, you have inspired me with your universal knowledge and your enthusiasm for all new types of questions. Having a hands-on approach and getting things to work like you do is what sets apart a real physicist. Thank you for ideas, insight and for many good and enjoyable discussions. Also, thank you for the chance to present my research at international conferences and for your understanding of my projects outside the world of pure science.

A warm thank you also to Yvonne Simon. Yvonne, I admire your talent for organizing and your diplomatic skills. Thanks for helping me with settling in and with circumventing the shallow waters of bureaucracy and for all the good discussions.

I am thankful to Herwig Peterlik and Johanna-Masume Akbarzadeh Moghadam for the extensive help with all SAXS issues. Thanks to Stephan Puchegger for his readiness to help in all circumstances, for the EDX measurements and the pleasant discussions.

Also, a warm thank you to our emeritus Gero Vogl for numerous entertaining discussions about energy technology, about the Austrian opinion of "the Prussians" and of course about scientific questions. Gero, thanks for the opportunity to present our newest research results in Istanbul in your place.

I want to thank Michael Leitner for his many hints about data analysis and the numerous improvement suggestions for my manuscripts.

Thanks to Gerald Polt for the help with the DSC measurements. Also, thanks to Daniel Gitschthaler, Martina Rohrer, Peter Seebacher and the team of the construction workshop for the technical support.

Thanks go to Robert Richter for an enjoyable start at the research group. Robert, thanks for the introduction to the Austrian language variations.

A special thank you to research colleague and true friend Markus Stana. Markus, you always motivated me even after tiring beam times with your humorous ways. Thanks for all the ideas, for good discussions and for your hints for this work.

I want to thank all current and former members of our working group. You have made my time so wonderful and unforgettable.

Thanks go also to the Austrian Science Fund for the sponsorship of my scientific research.

I thank my whole family and particularly my brother. Daniel, I have learned a great deal from you in all these years. I owe my largest debt of gratitude towards my parents. You have taught me so much and given me so much good. You have been the best inspiration I can think of.

Contents

Abbreviations

AC	Alternating Current
ADU	Analog-to-Digital Unit
aXPCS	atomic-scale X-ray Photon Correlation Spectroscopy
CAD	Computer-Aided Design
CCD	Charge-Coupled Device
DC	Direct Current
DESY	Deutsches Elektronen-Synchrotron
DLSR	Diffraction-Limited Storage Ring
DSC	Differential Scanning Calorimetry
EDX	Energy-Dispersive X-ray spectroscopy
ERL	Energy Recovery Linac
ESRF	European Synchrotron Radiation Facility
EXAFS	Extended X-ray Absorption Fine Structure
IR	Infrared
KWW	Kohlrausch-Williams-Watts
MC	Monte Carlo
MCT	Mode-Coupling Theory
MD	Molecular Dynamics
NFS	Nuclear Forward Scattering
NMR	Nuclear Magnetic Resonance
PCS	Photon Correlation Spectroscopy
PETRA III	Positron-Elektron-Tandem-Ring-Anlage III
PID	Proportional-Integral-Derivative
QENS	Quasi-Elastic Neutron Scattering
RF	Radio Frequency
RFOT	Random First-Order Transition
RMC	Reverse Monte Carlo
SAXS	Small-Angle X-ray Scattering
SNR	Signal-to-Noise Ratio

XFEL	X-ray Free Electron Laser
XPCS	X-ray Photon Correlation Spectroscopy
XPS	X-ray Photoelectron Spectroscopy
XSVS	X-ray Speckle Visibility Spectroscopy

Chapter 1
Introduction

When Planck started his academic studies, he was discouraged from studying physics by his future teacher, who claimed that most problems of physics were already solved. Many ground-breaking new theories have disproved this view and many more mysteries remain unsolved to this day. A particularly puzzling field of physics are the properties of amorphous solids. Having been in focus of great research efforts for more than a century, fundamental properties of these materials are still not clear on a basic level. Especially the dynamic properties of glasses on the atomic scale are far from being understood. The atomic diffusion processes are the source of many important material properties and the nature of glasses has been described as one of the deepest unsolved problems in solid state theory (Anderson 1995).

The main goal of this thesis is to show how the atomic movements in glasses can be directly studied by a new technique called atomic-scale X-ray Photon Correlation Spectroscopy (aXPCS). This technique has been derived from the long-established method Photon Correlation Spectroscopy (PCS) and gained great momentum with the introduction of modern third generation synchrotron sources and recent advances in the creation of coherent X-rays. As a second goal, the practical application and potential future impact of this technique shall be demonstrated by revealing insight into fast ionic conducting glasses, relevant in fields such as energy storage applications.

We will first take a glimpse at the peculiar properties of glasses. Then, we will learn about the new method utilised in this thesis for obtaining deeper knowledge about this material class on the basic length scale.

1.1 A Long-Standing Challenge: Gaining Insight into Glass Fundamentals

In order to better understand the properties of glasses, we will look into the connection of structure and dynamics in this material class.

M. Ross, *Atomic Diffusion in Glasses Studied with Coherent X-Rays*,
Springer Theses, DOI 10.1007/978-3-319-28646-4_1

1.1.1 Glass Structure

Glasses have been known to mankind since ancient times. First used in their natural occurring form, it was later discovered how to produce these materials technically. However, the scientific approach to this material started much later. The 19th century can be seen as the beginning of systematic glass science, with important works of e.g. Fraunhofer, Schott, Abbe and Zeiss (Kurkjian and Prindle 1998).

There are multiple ways to define glasses (Fig. 1.1). What seems to be common ground for all views on this material class is the lack of a long-range order. The peculiarity about glass is the similarity in structure of the liquid and the glassy state. Cooling down from the liquid state faster than a certain rate (which would be necessary to allow for the material to crystallise) is the most common way to produce a glass. Macroscopically, the glass forming by lowering the temperature can be characterised using an empirical formula for the viscosity, the so-called Vogel-Fulcher-Tammann law (Shelby 2005)

$$\eta \propto \exp\left(\frac{C}{T - T_0}\right), \tag{1.1}$$

where C is a constant and T_0 the so-called Vogel temperature. At a certain viscosity, typically on the order of 10^{12} Pa s, the former liquid is defined to be in the solid state. The remarkable difference to crystallisation is the fact that there is no sharp phase transition for vitrification when cooling down from the melt. This behaviour

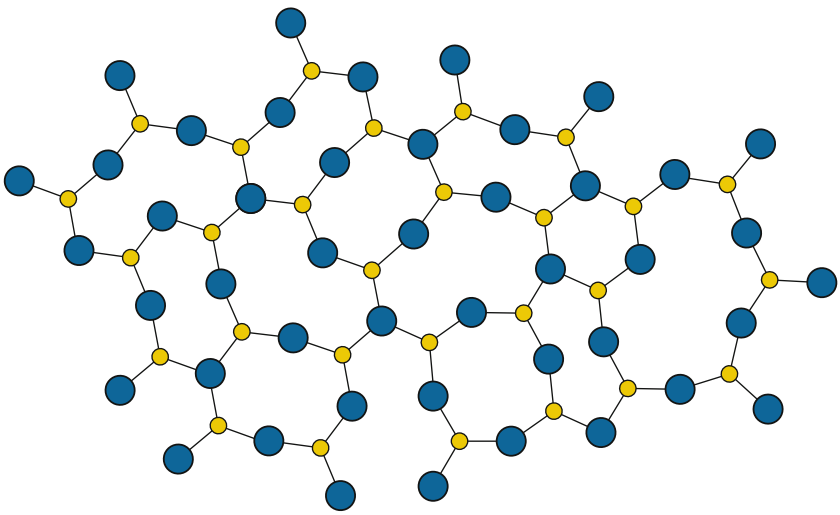

Fig. 1.1 Part of a network of randomly connected atomic motifs depicted in two dimensions, as envisioned by Zachariasen (1932). In this example, one atomic species may only have two connections and the other species has exactly three connections per atom

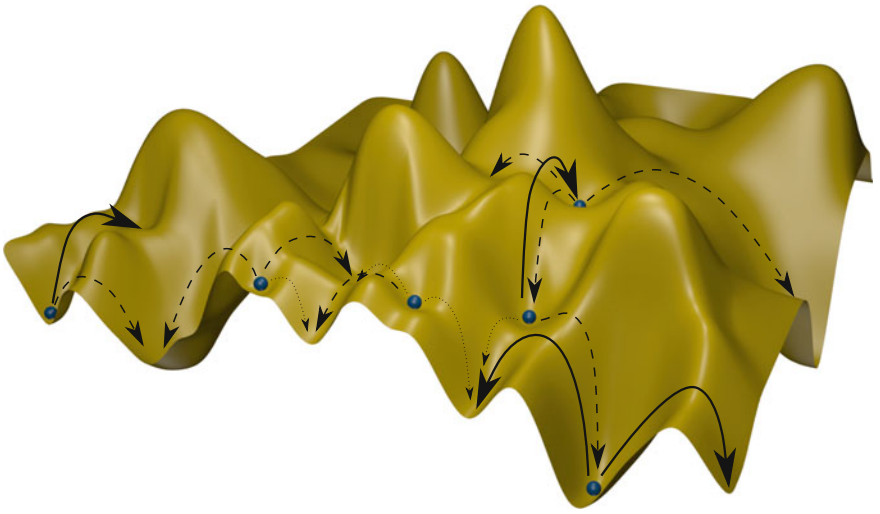

Fig. 1.2 Two-dimensional projection of a potential energy landscape. Atoms of the glass can be arrested in basins on different energy levels. On short time scales and for small thermal energies, only small energy barriers can be surpassed (*thin*, *dotted arrows*). On medium time scales and energy levels, higher energy barriers can be overcome (*dashed arrows*). On long time scales and with high thermal energies, even high potential energy barriers can be surpassed (*thick*, *continuous arrows*). Thus on longer time scales and with higher thermal energy, significantly more states can be reached. It is worth noting that the height of the potential energy peaks is not directly relevant for the diffusion but rather the saddle point height

can be understood as atoms being energetically trapped in an intermediate state (Parisi and Sciortino 2013), as the viscosity poses a kinetic barrier for further atomic rearrangements (see Fig. 1.2). Defining the glassy state based on the viscosity is convenient as this is a very accessible and comprehensible quality of this material class. However, there are other ways to synthesise materials in the glassy state, which cannot be explained by this viscosity approach. Among these methods are vapour deposition, sol-gel processing and neutron irradiation of crystalline materials (Shelby 2005; Mehrer 2007).

As oxide glasses belong to the technically relevant materials, it is highly desirable to understand their fundamental properties (Mehrer 2007). An oxide might act as a network former, a network modifier or an intermediate oxide. Network formers, such as SiO_2 and B_2O_3, can be vitrified as single component glasses. Network modifiers like the alkali oxides only produce glasses in combination with other materials and can also enable vitrification of elements which would otherwise crystallise. Intermediates like lead oxide can act both as former and as modifier (Mehrer 2007). All oxide glasses studied in this thesis can be readily produced by cooling from the melt, thus this approach has been utilised throughout.

First attempts to explain the glass structure on the microscopic level tried to incorporate the structural insight obtained from X-ray scattering at crystalline materials. An approach known under the term *random network theory*, proved to be successful in describing the formation of glasses and was ultimately also applied for describing glass structure. The foundations of this theory were laid by Zachariasen (1932) and Warren (1934). There has been much debate between whether crystallite or network theories describe the experimental data more appropriately (Wright 2013). The short-range order could be probed relatively easily by means of X-ray diffraction, the intermediate range order, however, is much more difficult to investigate. Many different methods like neutron scattering, Extended X-ray Absorption Fine Structure (EXAFS), Nuclear Magnetic Resonance (NMR) and spectroscopic methods like Infrared (IR) and Raman spectroscopy have eventually shed light on the structural details at this dimension (Greaves 1985; Rao 2002; Greaves and Sen 2007). The dynamics, however, are still much less clear.

1.1.2 Glassy Dynamics

Dynamics and structure of glasses are closely connected. From the vitrification by quenching perspective, the glass structure is not in thermal equilibrium, but in a metastable state, resembling an arrangement which would be equilibrated at a higher temperature, called the fictive temperature T_f (Lubchenko and Wolynes 2007). In that sense, the dynamics of glasses can be thought of as being ruled by a complex potential energy landscape with basins of different depths and widths (Parisi and Sciortino 2013), which is a subset of all energetic states that were reachable before quenching (see Fig. 1.2). Instead of being able to move rather freely between collisions, the atoms now interact mostly with the same group of neighbouring atoms. As a consequence, the motion of the atoms becomes confined within a cage-like arrangement. Atomic motions in this state are mostly of a vibrational nature. The much less frequent translational motions beyond a cage require displacement beyond certain energy thresholds, leading to discretised movements into new potential basins.

Glasses are in a metastable state in a twofold way: They can crystallise over long time scales and they can undergo a process called structural relaxation (Mehrer 2007). Structural relaxation implies that properties of glasses depend on their thermal history. We will see in Chap. 6 that this thermal history can influence the atomic dynamics.

Intense scientific effort has been put into the quest for explaining the glass transition, including Random First-Order Transition (RFOT) theory (Lubchenko and Wolynes 2007) and the Mode-Coupling Theory (MCT) approach (Götze 1999). The coexistence of slow and fast particles, also known as dynamic heterogeneity, plays an important role in the dynamics of glassy materials (Vollmayr-Lee et al. 2002; Chaudhuri et al. 2007). While these models are mostly concerned with the physics at and above the glass temperature, we will look into the deep glassy state below the temperature of glass transition. It should be noted that the field of glass physics

and especially the glass transition is subject to controversial discussion (Kurchan et al. 2011) and no single model has proved to be able to capture all experimental observations (Ediger et al. 1996).

Some properties of solid materials, like heat conductivity, can be readily explained without having to modify the image of a fixed structure aside vibrations around the centre of mass points of the atoms. Many other properties, however, like ionic conduction, could not be explained without the concept of slight changes in the structure taking place over time on the atomic level. In this thesis, the effects of atomic motion in the deep glassy state beyond vibrations shall be studied. For that, we will see that the new method of aXPCS can give insight into the dynamics of glasses and that it can reveal details of atomic motion with technical relevance (see Chaps. 5 and 6).

1.2 A New Method for Studying Dynamics: aXPCS

Many methods are being applied to study glasses. We will look at some of the most widely utilised methods for studying dynamics and see how aXPCS can extend the range of systems and states accessible for study.

1.2.1 Methods for Studying Diffusion

Diffusion in solids can be studied using a wide range of techniques. With respect to the thesis at hand, two dimensions are particularly important for the choice of method. Firstly, the spatial resolution needs to be in the angstrom regime in order to study atomic motions. Secondly, the frequency range of the technique needs to cover the relatively slow motions of the particles in solid materials. There are some techniques which entirely satisfy one of these demands but not the other, as shown in Fig. 1.3. The method capable of meeting both demands combined is aXPCS. One should note that the time dimension mentioned here can be translated into an energy dimension and is material and temperature dependent. Thus a given material sample could potentially be made available to certain measurement methods by increasing its temperature. However, this will not deliver comparable results if a change in the diffusion mechanism is taking place, which is particularly the case when the material starts melting or crystallising.

Some approaches, like the tracer method and many variants of NMR are able to study a wide range of diffusivities but are not spatially resolved. Other methods are primarily useful for studying atomic vibrations and phonons, like Raman and Brillouin spectroscopy.

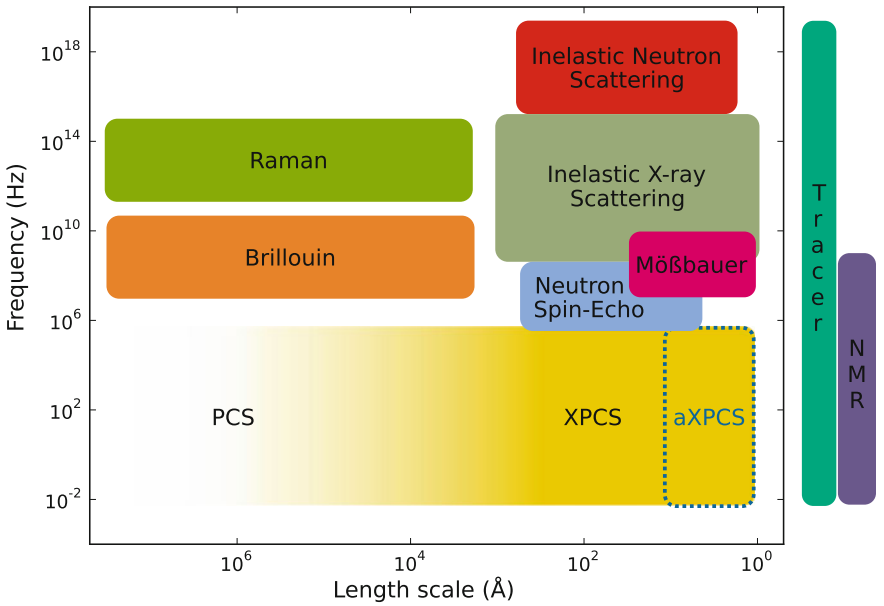

Fig. 1.3 Different methods for measuring diffusion, plotted with respect to the approximate length scales and frequency ranges covered. Macroscopic methods are plotted only with respect to the frequency ranges accessible to them

The method of X-ray Photon Correlation Spectroscopy (XPCS) can be compared in many respects to Quasi-Elastic Neutron Scattering (QENS). QENS works in the energy domain while aXPCS works in the time domain. However, both domains can be exchanged by Fourier transforming. There are two different versions of QENS, namely coherent and incoherent QENS. An important difference of both methods lies in the kind of correlations measured. The incoherent technique measures the self-correlation, which is the conditional probability that a specific atom is found at position $\mathbf{r}$ at time t if it was at $\mathbf{r} = 0$ for $t = 0$. Other widely used incoherent methods are Mössbauer spectroscopy and Nuclear Forward Scattering (NFS). Coherent QENS measures the pair-correlation, which is the probability that any atom is found at position $\mathbf{r}$ at time t if an atom was at $\mathbf{r} = 0$ for $t = 0$. This is typically described by the van Hove pair-correlation function $G(\mathbf{r}, t)$, as we will see in Sect. 2.2.1. In neutron scattering, the degree of coherence of the scattering depends on the isotope, thus the type of method applied can be chosen depending on the element and isotope. X-ray scattering does not distinguish between different isotopes of the same element but between different elements. Thus aXPCS does not measure the self-diffusion but the so-called chemical diffusion (Hempelmann 2000). We will come back to the connection of coherent and incoherent methods in Sect. 2.4.3.

1.2.2 The Development of aXPCS

Although aXPCS is a very recent method, it builds upon decades of scientific progress, especially in the fields of photon correlation techniques and coherent light sources.

Dynamics of Diffusing Particles: PCS

The technique of Photon Correlation Spectroscopy (PCS) is widely used to study the dynamics of soft condensed matter like particles suspended in liquids. Its underlying principle is that structural changes in the position of particles are directly connected to changes in the intensity of light scattered at these particles. The changes are detectable as fluctuations in the so-called speckle patterns. These interference patterns occur for coherent light being scattered at, or reflected from, disordered matter. While PCS is a very established technique, it has certain limitations like only being able to measure samples transparent to visible light and containing objects which should not be much smaller than its wavelength. This lead to the idea to extend the range of accessible systems by utilising radiation with a smaller wavelength.

Evolution of X-Ray Sources

One of the major experimental differences between PCS and XPCS is that PCS uses visible light and XPCS utilises X-rays. Due to the shorter wavelength of this radiation, smaller length scales can be studied. Additionally, multiple scattering of radiation is avoided as the scattering cross-section of X-rays in matter is very small compared to that of visible light. The scientific use of X-rays started after their discovery by Röntgen at the end of the 19th century. While X-rays found many applications in a broad range of disciplines, it was only towards the end of the 20th century that they were used for photon correlation spectroscopy techniques (Sutton et al. 1991; Brauer et al. 1995). This is due to the fact that the coherent intensity provided by X-ray sources was typically far too low to be utilised for this method and appropriate detectors where lacking. With the development of new X-ray sources this fact changed significantly. Particularly, the evolution of synchrotron sources lead to a huge improvement in many X-ray beam properties. The term *synchrotron radiation* in the context of this thesis will refer to radiation generated in synchrotrons with wavelengths exclusively in the X-ray regime, although in principle radiation with other wavelengths can also be provided by these facilities.

Initially, synchrotron radiation was just a byproduct of high-energy particle accelerators. Soon it was realised that the special properties of this type of radiation could have many potential applications. The facilities for using this radiation parasitically were later called first generation synchrotron sources. The so-called second generation synchrotron sources were, in contrast, facilities dedicated specifically to the production of this kind of radiation.

Striving for even more intense and superior synchrotron beams, advanced devices were developed, namely wigglers and particularly undulators (see Sect. 3.3.1). The first successful demonstration of the undulator principle dates back to the 1950s, producing microwave radiation. However, it was only in the 1980s that this principle could also be used for producing X-rays, mostly due to the development of new magnetic alloys necessary to create magnet arrays with small periodicity and high magnetic field strength (Willmott 2011). The large-scale application of these devices led to the third generation of synchrotron sources. The first of these facilities to be completed was the European Synchrotron Radiation Facility (ESRF) in Grenoble. In the following years, many methods around synchrotron radiation were established as scientific tools and applied in a wide range of scientific and industrial studies (Tolfree 1998; Willmott 2011). There is an ever increasing number of synchrotron sources, with more than 50 synchrotrons operational in 2005 (Bilderback et al. 2005). Notable new facilities include the largest synchrotron light source in the world, the Positron-Elektron-Tandem-Ring-Anlage III (PETRA III) at Deutsches Elektronen-Synchrotron (DESY) in Hamburg, which took up operation in 2009. We will look at the physical principle of these large-scale devices in Sect. 3.3.

The technique of using undulators to create coherent radiation has been developed further and new facilities called X-ray Free Electron Laser (XFEL) are being built and starting operation, leading to the creation of X-radiation with laser-like properties. New opportunities and challenges emerge from the extremely short and intense beam pulses produced by these devices. Other new developments include the Energy Recovery Linac (ERL) and the Diffraction-Limited Storage Ring (DLSR) (Bilderback et al. 2005; Shpyrko 2014), which will provide higher brilliance but a bunch structure similar to that of synchrotrons. The huge improvement of the brilliance (as defined in Sect. 3.3.1) in the course of the last decades (see Fig. 1.4) underlines the importance of X-rays as a versatile tool and the success of coherent methods like XPCS (Fig. 1.5).

Extension to the Atomic Regime: aXPCS

The technique of XPCS is a powerful tool for studying dynamics in disordered systems. Many works have gained insight into soft matter dynamics in the nanometre range, e.g. for magnetic nanoparticles (Robert et al. 2005), complex fluids (Leheny 2012), polymers (Guo et al. 2012), organic molecular glass formers (Chushkin et al. 2012) and a wide range of other systems (Grübel et al. 2008). The first proofs of concept of the method were achieved by Sutton et al. (1991) and Brauer et al. (1995). Leitner et al. (2009) proved recently that XPCS can resolve single atomic motion in condensed matter. In consecutive works, Stana et al. (2013) showed how to resolve atomic dynamics in less-ordered polycrystalline materials and coined the term aXPCS. Work on the metallic glass ZrNiCuAl showed that the diffusion in this material is out of equilibrium (Leitner et al. 2012). Recently it was shown that ultrafast dynamics on the atomic scale should be measurable with aXPCS (Hruszkewycz et al. 2012).

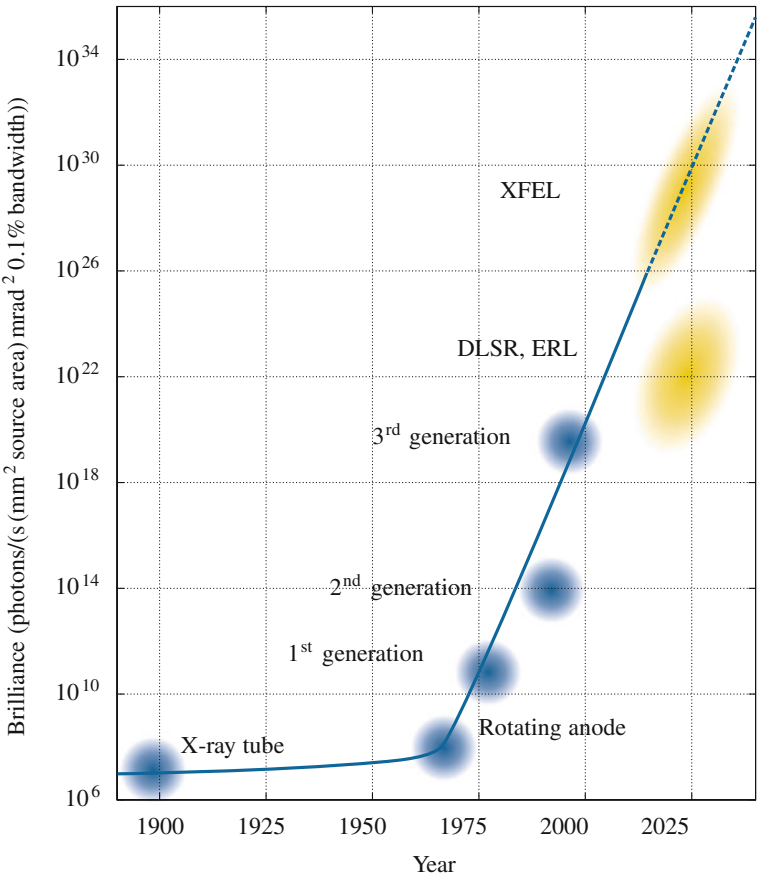

Fig. 1.4 Increase of brilliance with time, triggered by developments of new anodes, new synchrotron generations and new laser-like sources. Based on data and estimations from Altarelli and Salam (2004), García-Gutiérrez and Rueda (2009), Willmott (2011) and Shpyrko (2014)

Determining atomic dynamics of amorphous solids has been a long-standing issue because the lack of long-range translational and rotational symmetry renders it experimentally inaccessible for many conventional diffraction methods which can access the according length scales. We will see that the method of aXPCS can be used to tackle this challenge. In the subsequent chapters, the theoretical foundations of aXPCS will be explained and we will see how this new method can be experimentally realised for glasses and how the obtained data can be analysed to give insight into glassy dynamics on the atomic scale. We will then look into the systems selected

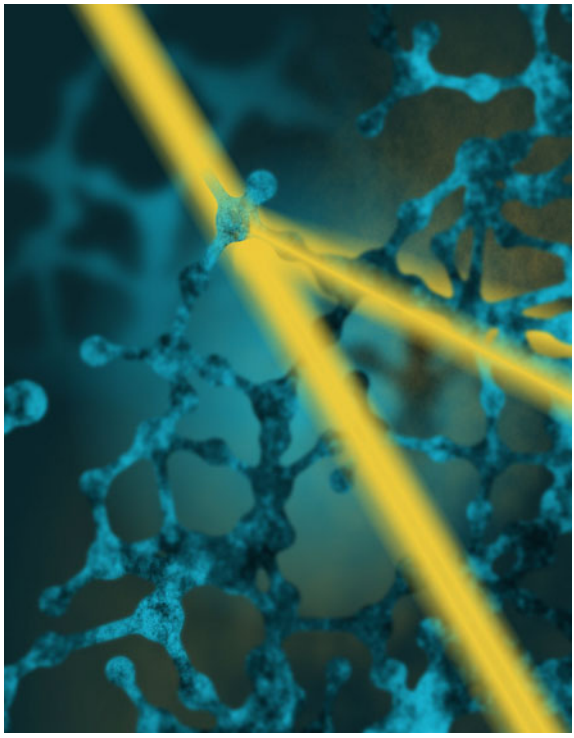

Fig. 1.5 Artistic visualisation of X-ray scattering in glass

for study and see what makes them particularly insightful as showcase materials. Finally, we will learn about the results obtained by the successful realisation of atomic diffusion studies in glasses.

References

Altarelli, M., & Salam, A. (2004). The quest for brilliance: Light sources from the third to the fourth generation. *Europhysics News*, *35*(2), 47–50.

Anderson, P. W. (1995). Through the glass lightly. *Science*, *267*(5204), 1615–1616.

Bilderback, D. H., Elleaume, P., & Weckert, E. (2005). Review of third and next generation synchrotron light sources. *Journal of Physics B: Atomic, Molecular, and Optical Physics*, *38*(9), 773–797.

Brauer, S., Stephenson, G., Sutton, M., Brüning, R., Dufresne, E., Mochrie, S., et al. (1995). X-Ray Intensity Fluctuation Spectroscopy Observations of Critical Dynamics in Fe_3Al. *Physical Review Letters*, *74*(11), 2010–2013.

Chaudhuri, P., Berthier, L., & Kob, W. (2007). Universal nature of particle displacements close to glass and jamming transitions. *Physical Review Letters*, *99*(6), 060604.

Chushkin, Y., Caronna, C., & Madsen, A. (2012). A novel event correlation scheme for X-ray photon correlation spectroscopy. *Journal of Applied Crystallography*, *45*(4), 807–813.

Ediger, M. D., Angell, C. A., & Nagel, S. R. (1996). Supercooled liquids and glasses. *Journal of Chemical Physics*, *100*(31), 13200–13212.

García-Gutiérrez, M. C., & Rueda, D. R. (2009). Bases of synchrotron radiation and light sources. In T. A. Ezquerra., M. C. García-Gutiérrez., A. Nogales, & M. A. Gómez (Eds.), *Applications of synchrotron light to scattering and diffraction in materials and life sciences* (pp. 1–22). Berlin: Springer.

Götze, W. (1999). Recent tests of the mode-coupling theory for glassy dynamics. *Journal of Physics Condensed Matter*, *11*(10A), A1–A45.

Greaves, G. N. (1985). EXAFS and the structure of glass. *Journal of Non-Crystalline Solids*, *71*(1–3), 203–217.

Greaves, G. N., & Sen, S. (2007). Inorganic glasses, glass-forming liquids and amorphizing solids. *Advances in Physics*, *56*(1), 1–166.

Grübel, G., Madsen, A., & Robert, A. (2008). X-ray photon correlation spectroscopy (XPCS). In R. Borsali., & R. Pecora (Eds.), *Soft-matter characterization* (pp. 935–995). Berlin: Springer.

Guo, H., Bourret, G., Lennox, R. B., Sutton, M., Harden, J. L., & Leheny, R. L. (2012). Entanglement-controlled subdiffusion of nanoparticles within concentrated polymer solutions. *Physical Review Letters*, *109*(5), 055901.

Hempelmann, R. (2000). *Quasielastic neutron scattering and solid state diffusion*. Oxford: oxford University Press.

Hruszkewycz, S. O., Sutton, M., Fuoss, P. H., Adams, B., Rosenkranz, S., Ludwig, K. F., et al. (2012). High contrast X-ray speckle from atomic-scale order in liquids and glasses. *Physical Review Letters*, *109*(18), 185502.

Kurchan, J., Langer, J. S., Witten, T. A., & Wolynes, P. G. (2011). Scientific interview (Chapter 1). In L. Berthier., G. Biroli., J.-P. Bouchaud., L. Cipelletti., & W. van Saarloos (Eds.), *Dynamical heterogeneities in glasses, colloids, and granular media* (pp. 1–38). Oxford: Oxford University Press.

Kurkjian, C. R., & Prindle, W. R. (1998). Perspectives on the History of glass composition. *Journal of the American Ceramic Society*, *81*(4), 795–813.

Leheny, R. L. (2012). XPCS: Nanoscale motion and rheology. *Current Opinion in Colloid and Interface Science (COCIS)*, *17*(1), 3–12.

Leitner, M., Sepiol, B., Stadler, L.-M., Pfau, B., & Vogl, G. (2009). Atomic diffusion studied with coherent X-rays. *Nature Materials*, *8*(9), 717–720.

Leitner, M., Sepiol, B., Stadler, L.-M., & Pfau, B. (2012). Time-resolved study of the crystallization dynamics in a metallic glass. *Physical Review B*, *86*(6), 064202.

Lubchenko, V., & Wolynes, P. G. (2007). Theory of structural glasses and supercooled liquids. *Annual Review of Physical Chemistry*, *58*(1), 235–266.

Mehrer, H. (2007). *Diffusion in solids*. Berlin: Springer.

Parisi, G., & Sciortino, F. (2013). Structural glasses: Flying to the bottom. *Nature Materials*, *12*(2), 94–95.

Rao, K. J. (2002). *Structural chemistry of glasses*. Amsterdam: Elsevier.

Robert, A., Wagner, J., Autenrieth, T., Härtl, W., & Grübel, G. (2005). Structure and dynamics of electrostatically interacting magnetic nanoparticles in suspension. *The Journal of Chemical Physics*, *122*(8), 084701.

Shelby, J. E. (2005). *Introduction to glass science and technology*. Cambridge: Royal Society of Chemistry.

Shpyrko, O. G. (2014). X-ray photon correlation spectroscopy. *Journal of Synchrotron Radiation*, *21*(5), 1057–1064.

Stana, M., Leitner, M., Ross, M., & Sepiol, B. (2013). Studies of atomic diffusion in Ni-Pt solid solution by x-ray photon correlation spectroscopy. *Journal of Physics: Condensed Matter*, *25*(6), 065401.

Sutton, M., Mochrie, S. G. J., Greytak, T., Nagler, S. E., Berman, L. E., Held, G. A., et al. (1991). Observation of speckle by diffraction with coherent X-rays. *Nature*, *352*(6336), 608–610.

Tolfree, D. W. L. (1998). Microfabrication using synchrotron radiation. *Reports on Progress in Physics*, *61*(4), 313–351.
Vollmayr-Lee, K., Kob, W., Binder, K., & Zippelius, A. (2002). Dynamical heterogeneities below the glass transition. *The Journal of Chemical Physics*, *116*(12), 5158.
Warren, B. (1934). The diffraction of X-rays in glass. *Physical Review*, *45*(10), 657–661.
Willmott, P. (2011). *Applications of synchrotron light to scattering and diffraction in materials and life sciences*. New York: Wiley.
Wright, A. C. (2013). The great crystallite versus random network controversy: A personal perspective. *International Journal of Applied Glass Science (IJAGS)*, *5*(1), 31–56.
Zachariasen, W. H. (1932). The atomic arrangement in glass. *Journal of the American Chemical Society*, *54*(10), 3841–3851.

Chapter 2
Theory

Let us look at the theoretical principles of XPCS and outline the connection of the actual measurements to the conclusions which can be drawn from them. We will see how intensity patterns arise from scattering at atoms, how these patterns over time can be interpreted to give information on correlations on atoms in real space and how these correlations can be interpreted to give insight into actual atomic movements. Finally we will look at some additional considerations on this method applied to the atomic dynamics in glasses.

2.1 Achieving Coherent Scattering

Crucial to any XPCS experiment is coherently scattered radiation. Let us see how scattering can be achieved in general, how sufficient intensities are reached and how coherence can be ensured.

2.1.1 Scattering Intensity and Speckle Patterns

When an at least partly coherent monochromatic beam of light scatters at a grid or an ensemble of slits or particles, a scattering pattern can be observed at a screen put downstream the propagation direction of the beam (see Fig. 2.1). This pattern is static if nothing changes in the setup and particularly as long as the grid stays unchanged. If the spacing of the grid is modified or parts of the grid are removed, then the scattering pattern will change accordingly. There is normally no straightforward way to directly deduce on the structure of a scatterer from the diffraction pattern. However, under certain circumstances it is possible to gain information on the changes in the structure from the time evolution of scattering intensity. This is the underlying principle of XPCS.

M. Ross, *Atomic Diffusion in Glasses Studied with Coherent X-Rays*,
Springer Theses, DOI 10.1007/978-3-319-28646-4_2

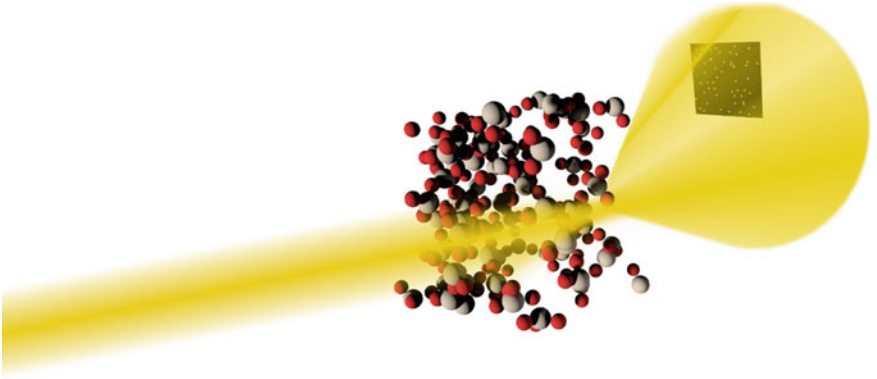

Fig. 2.1 Visualisation of X-rays scattered at an atomic arrangement. The detector on the right catches part of the scattered radiation

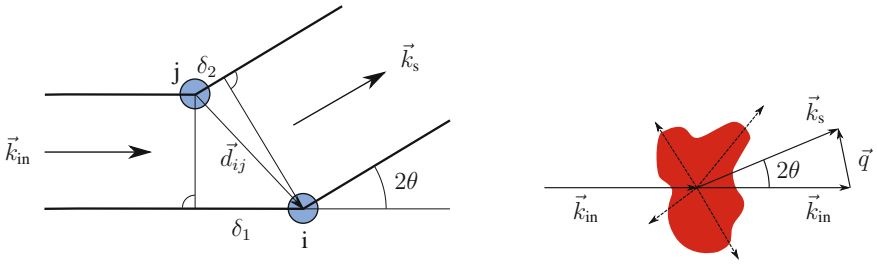

Fig. 2.2 Schematic of the scattering process in matter. *Left* The incident radiation with wave vector $\vec{k}_{in}$ is scattered at two atoms i and j. When observing the scattered radiation at angle 2θ, the scattered waves have a path difference of $\delta = \delta_1 - \delta_2$. *Right* The scattered radiation in the sample can be described in terms of the difference of the wave vectors of the incident radiation $\vec{k}_{in}$ and the scattered radiation $\vec{k}_s$, denoted as $\vec{q}$

The scattering pattern of coherent radiation is also called speckle pattern. This results from the fact that for elastically scattered radiation only the phases change but the frequencies stay the same, so by constructive and destructive interference a pattern is created which contains areas of different intensity. A schematic is shown in Fig. 2.2. Two waves scattered at different atoms under an angle 2θ will have a path difference of $\delta = \delta_1 - \delta_2$. This can be expressed in terms of the vector between the two scattering centres $\vec{d}_{ij}$ and the wave vectors. With the projections of $\vec{d}_{ij}$ on the wave vectors, $\vec{d}_{ij} \cdot \vec{k}_{in} = \delta_1$ and $\vec{d}_{ij} \cdot \vec{k}_s = \delta_2$ and with the position vectors to the scattering centres in an arbitrary basis $\vec{r}_i - \vec{r}_j = \vec{d}_{ij}$, the path difference can be described as

$$\delta = \vec{q} \cdot \left(\vec{r}_i - \vec{r}_j\right). \tag{2.1}$$

Here, $\vec{q} = \vec{k}_{in} - \vec{k}_s$ is called the scattering vector. Its length depends on the scattering angle, as

$$\sin\left(\frac{2\theta}{2}\right) = \frac{q}{2k_{\text{in}}}. \tag{2.2}$$

With $k_{\text{in}} = \frac{2\pi}{\lambda}$, the length of the scattering vector can be expressed as

$$q = \frac{4\pi}{\lambda}\sin\left(\frac{2\theta}{2}\right). \tag{2.3}$$

Considering the Abbe limit in the form $d = \frac{\lambda}{2\sin\theta}$, with structure size d, wavelength λ, and scattering angle 2θ (up to about 35° in the experiments conducted in the course of this thesis) shows that in order to be sensitive for atomic distances, the wavelength of the radiation needs to be in the angstrom regime. In the synchrotron experiments reported here, radiation with a wavelength of about 1.5 Å is used, which is equivalent to photon energies in the range of some 7–8 keV.

The intensity measured at a detector is the result of the interference of all waves scattered in the sample. We will restrict ourselves to elastic scattering (Rayleigh scattering), as only this type of scattering leads to the fixed phase relation of the scattered radiation required for XPCS. Thus the energy of the scattered radiation considered in the typical XPCS experiment is for all practical purposes unchanged. The electrical field far from the scattering centres is in principle the sum of all scattered waves

$$E(\vec{q},t) \propto \sum_{i=1}^{N} a_i \mathrm{e}^{\mathrm{i}\vec{q}\vec{r}_i(t)}, \tag{2.4}$$

with number of atoms N and scattering length a_i (which is implicitly also dependent on the scattering vector). It can also be expressed as the Fourier transform of the electron density, thus containing the information on the electron positions and consequently on the atomic positions. Unfortunately, the oscillations of the electrical field are too fast to be directly accessible in the experiment (for an X-ray photon with an energy of $h\nu \approx 8$ keV the oscillation frequency of the electromagnetic field is on the order of $10^{18}\,\mathrm{s}^{-1}$). However, what is readily detectable is the intensity. The intensity is proportional to the time average of the squared electrical field EE^*:

$$I(\vec{q}) = \left\langle E(\vec{q},t)E^*(\vec{q},t)\right\rangle_t \propto \left\langle \sum_{i=1}^{N}\sum_{j=1}^{N} a_i a_j^* \mathrm{e}^{\mathrm{i}\vec{q}(\vec{r}_i(t)-\vec{r}_j(t))}\right\rangle_t \tag{2.5}$$

Thus the intensity is taking into account the different phases due to different path lengths. This can be expressed with the phase factor from Eq. (2.1) as interference factor

$$\mathrm{e}^{\mathrm{i}\delta} = \mathrm{e}^{\mathrm{i}\vec{q}(\vec{r}_i-\vec{r}_j)}. \tag{2.6}$$

This shows that the intensity pattern contains information on the structural details of the material. However, it is normally not directly possible to access these details

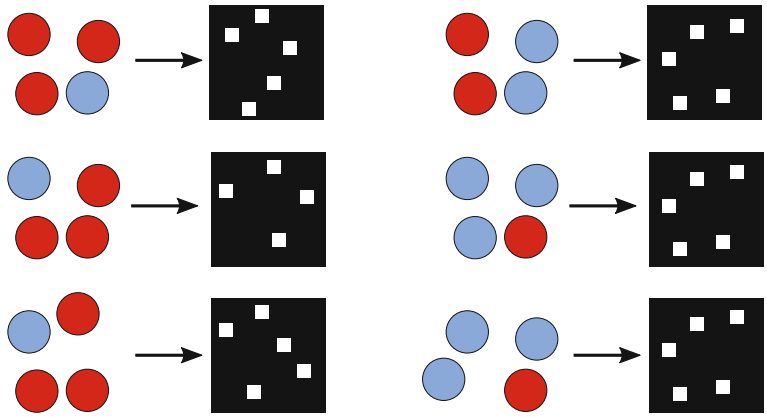

Fig. 2.3 Sketch of atomic arrangements (with two different element species) and resulting scattering patterns. *Left* A change in atomic arrangement leads to a change in the scattering pattern. *Right* It is possible that different arrangements produce the same scattering pattern. Thus it is not possible to directly deduce the structure from the scattering pattern

due to the lost phase information by averaging, or in other words, there is no direct way to invert Eq. (2.5). This is widely known as the phase problem, as depicted in Fig. 2.3. There are different approaches to circumvent this problem, notably in X-ray imaging (Marchesini et al. 2003). When investigating dynamics, the structure of the material is not of direct concern, but rather the *changes* in structure. We can thus ignore the structural details and use the time fluctuations of the scattering pattern instead to study the dynamics of the material. This fact is utilised by the method of XPCS. The principles of this method can be derived based on the van Hove pair correlation function, as we will see in Sect. 2.2.1.

2.1.2 Optimal Scattering Thickness

For any scattering experiment, it is important to find the optimal sample thickness W for the given geometry. An analytical expression can be derived for the scattered intensity I at a scattering angle 2θ relative to the direct beam with the absorption coefficient μ and the isotropic scattering factor s. Assuming the incident beam with intensity I_0 to be perpendicular to the sample surface and integrating over the scattered intensity in an infinitesimal interval of the sample,

$$\mathrm{d}I = I_0 \mathrm{e}^{-\mu x} s \mathrm{e}^{-\mu y} \mathrm{d}x, \tag{2.7}$$

we get

$$I = I_0 s \int_0^W \mathrm{e}^{-\mu(x+y)} \mathrm{d}x. \tag{2.8}$$

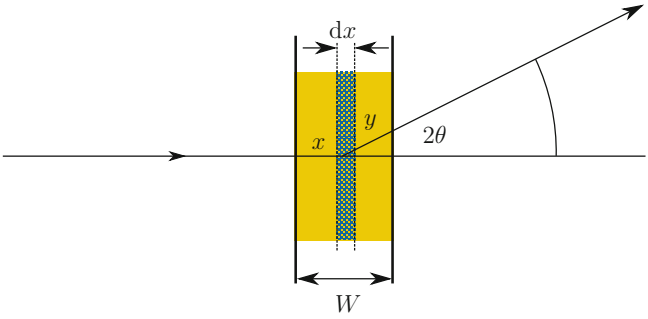

Fig. 2.4 Derivation of optimal sample thickness W by integration over infinitesimal intervals of the path length $\mathrm{d}x$, which is dependent on the scattering angle 2θ

As can be seen from Fig. 2.4, $y = \frac{W-x}{\cos 2\theta}$, which leads to:

$$\begin{aligned} I &= I_0 s \int_0^W \mathrm{e}^{-\mu\left(x+\frac{W-x}{\cos 2\theta}\right)} \mathrm{d}x \\ &= I_0 s \frac{\mathrm{e}^{-\frac{\mu W}{\cos 2\theta}} - \mathrm{e}^{-\mu W}}{\mu\left(1-\frac{1}{\cos 2\theta}\right)} \end{aligned} \tag{2.9}$$

The optimum can be found for $\frac{\partial I}{\partial W} = 0$ (and $\frac{\partial^2 I}{\partial^2 W} < 0$):

$$\frac{\partial I}{\partial W} = I_0 s \left(-\frac{\mathrm{e}^{-\frac{\mu W}{\cos 2\theta}}}{\cos 2\theta\left(1-\frac{1}{\cos 2\theta}\right)} + \frac{\mathrm{e}^{-\mu W}}{1-\frac{1}{\cos 2\theta}} \right) = 0 \tag{2.10}$$

Thus we get

$$\begin{aligned} \mathrm{e}^{-\mu W + \frac{\mu W}{\cos 2\theta}} &= \frac{1}{\cos 2\theta} \\ W &= \frac{\ln(\cos 2\theta)}{\mu\left(1-\frac{1}{\cos 2\theta}\right)}. \end{aligned} \tag{2.11}$$

For small angles Eq. (2.11) can be further simplified by rewriting Eq. (2.9) and expanding the exponential:

$$\begin{aligned} I &= I_0 s \mathrm{e}^{-\frac{\mu W}{\cos 2\theta}} \frac{1-\mathrm{e}^{-\mu W\left(1-\frac{1}{\cos 2\theta}\right)}}{\mu\left(1-\frac{1}{\cos 2\theta}\right)} \\ &\approx I_0 s \mathrm{e}^{-\frac{\mu W}{\cos 2\theta}} \frac{\mu W\left(1-\frac{1}{\cos 2\theta}\right)}{\mu\left(1-\frac{1}{\cos 2\theta}\right)} \\ &= I_0 s W \mathrm{e}^{-\frac{\mu W}{\cos 2\theta}} \end{aligned} \tag{2.12}$$

The optimum can be found analogously to Eq. (2.11). The calculation yields

$$W_{\text{small angles}} = \frac{\cos 2\theta}{\mu}. \tag{2.13}$$

This result is accurate with a relative deviation of less than 10 % for the angles which we will consider here.

The optimal thickness has been derived under the assumption that no multiple scattering occurs. While this is true for X-rays, it does not hold for other methods like neutron scattering. There, a lower sample thickness compared to Eq. (2.11) is necessary.

The thickness derived here is optimal for X-rays in that the amount of detected radiation is at a maximum at that thickness. However, the intensity is not the only factor which has to be considered in aXPCS. We will have to adjust the obtained result when taking coherence into account.

2.1.3 Coherence Properties

A very important property the scattered radiation must have is a high degree of coherence. We will later see that the Signal-to-Noise Ratio (SNR) is roughly proportional to the degree of coherence. The coherence properties of the incoming radiation can be characterised in terms of the longitudinal coherence length ξ_l and the transversal coherence length ξ_t. A detailed treatment of the criteria for coherent X-ray scattering can be found in Abernathy et al. (1998), Sandy et al. (1999) and Sutton (2006, 2008).

In order to have sufficient coherence in the scattered radiation, the scattered photons should not get out of phase while travelling on different optical paths through the sample. This can be achieved by having a maximum path length difference smaller than the longitudinal coherence length ξ_l. The radiation is not perfectly monochromatic. Typically, the wavelengths of the beam can be described by a spectral distribution with full width at half maximum $\Delta\lambda$. The longitudinal coherence length is defined as the distance after which radiation of wavelength λ is shifted by a phase of π (or in other words, half of a wavelength) from radiation of wavelength $\lambda + \Delta\lambda$ (see Fig. 2.5). Solving

$$\left(N + \frac{1}{2}\right)\lambda = N(\lambda + \Delta\lambda) \tag{2.14}$$

for N gives

$$N = \frac{\lambda}{2\Delta\lambda}. \tag{2.15}$$

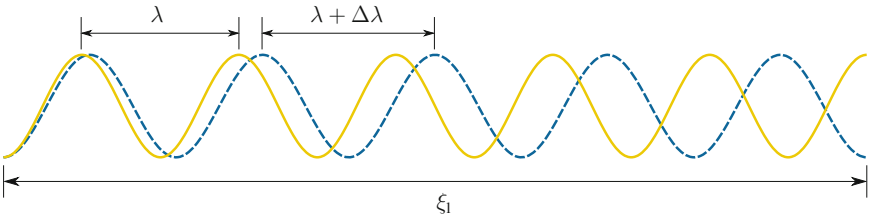

Fig. 2.5 Visualisation of the longitudinal coherence length ξ_l. As the beam radiation is not perfectly monochromatic, there is a spread of wavelengths, the extent of which can be characterised by $\Delta\lambda$. The longitudinal coherence length ξ_l is defined as the distance after which radiation of wavelength λ is shifted by a phase of π from radiation of wavelength $\lambda + \Delta\lambda$

With a typical monochromaticity of $\frac{\Delta\lambda}{\lambda} \approx 10^{-4}$, N is much greater than 1 and

$$\xi_l = \left(N + \frac{1}{2}\right)\lambda \approx N\lambda = \frac{\lambda^2}{2\Delta\lambda}. \tag{2.16}$$

The maximum path length difference is defined as the difference between the shortest and the longest geometrical path a photon of a beam with diameter d can travel through the sample with thickness W if being scattered under an angle 2θ. The two maximal paths are visualised in Fig. 2.6. The path length difference P is thus

$$P = p_1 + p_2 - p_3. \tag{2.17}$$

The sections of the paths can be derived from the geometrical relations

$$p_2 = (d + x)\sin 2\theta \tag{2.18}$$

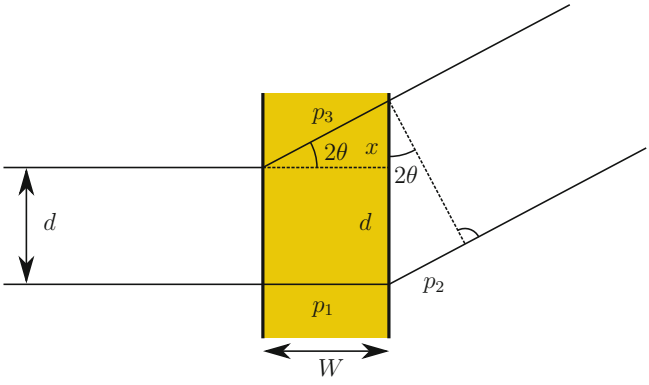

Fig. 2.6 Derivation of the maximum path length difference. The beam with maximal span d is scattered in the sample. The maximum path length difference for a certain scattering angle 2θ is the geometrical path difference between a directly scattered photon and a photon getting scattered after passing the entire sample thickness W

and

$$p_3 = \frac{W}{\cos 2\theta}. \tag{2.19}$$

With $p_3 = W^2 + x^2$, an expression for x can be found:

$$x = W\sqrt{\frac{1}{\cos^2 2\theta} - 1} = W\frac{\sin 2\theta}{\cos 2\theta} \tag{2.20}$$

Thus the maximum path length difference can be expressed as

$$\begin{aligned} P &= d\sin 2\theta + W\left(1 - \frac{1}{\cos 2\theta}\right) + W\frac{\sin^2 2\theta}{\cos 2\theta} \\ &= d\sin 2\theta + W\frac{\cos 2\theta - \cos^2 2\theta}{\cos 2\theta} \\ &= d\sin 2\theta + 2W\sin^2\theta. \end{aligned} \tag{2.21}$$

As we can see, the path length difference depends on the beam diameter, the scattering angle and the sample thickness. The smaller the path length difference, the higher the coherence of the scattered radiation will be. Thus for a given scattering angle, the coherence decreases with increasing beam diameter and increasing sample thickness. This shows that the sample thickness will have to be a compromise between scattering intensity and coherence. For typical values of $d \approx 10\,\mu\text{m}, 2\theta \approx 35°$ and $W \approx 10\,\mu\text{m}$, we obtain a maximum path length difference of $P \approx 7.5\,\mu\text{m}$.

Another condition for coherence is that the scattering centres should not be farther apart than the transversal coherence width perpendicular to the beam. This can be fulfilled by having the beam width in the order of the transversal coherence length ξ_t, which depends on the size σ_s and the distance R of the X-ray source. The transversal coherence length is defined to be the transversal distance within which two waves with the same wavelength originating from two points with distance σ_s will have a phase difference of π. From the geometrical considerations (see Fig. 2.7)

$$\sin\Delta\theta = \frac{\lambda}{2\xi_t} \tag{2.22}$$

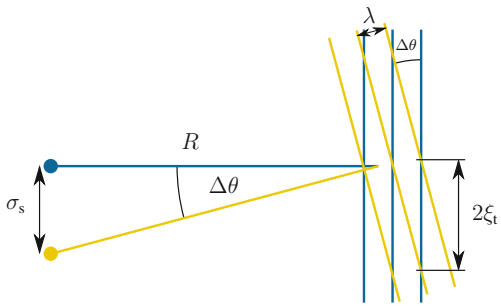

Fig. 2.7 Visualisation of the transversal coherence length ξ_t. Due to the angular beam divergence $\Delta\theta$, the waves originating from two points with distance σ_s will have a phase difference of π in a transversal distance which is defined to be the transversal coherence length ξ_t

and

$$\tan \Delta\theta = \frac{\sigma_\mathrm{s}}{R} \tag{2.23}$$

and taking into account that $\sin \Delta\theta \approx \Delta\theta$ and $\tan \Delta\theta \approx \Delta\theta$ as $\Delta\theta \ll 1$, the transversal coherence length can be derived:

$$\xi_\mathrm{t} = \frac{\lambda R}{2\sigma_\mathrm{s}} \tag{2.24}$$

Typically, the intensity profile of the beam is Gaussian shaped (Sinha et al. 2014) with the form

$$I(x, y) \propto \exp\left(-\frac{x^2}{2\sigma_x^2} - \frac{y^2}{2\sigma_y^2}\right), \tag{2.25}$$

which leads to two different transversal coherence lengths

$$\xi_{\mathrm{t}x} = \frac{\lambda R}{2\sigma_{\mathrm{s}_x}} \tag{2.26}$$

and

$$\xi_{\mathrm{t}y} = \frac{\lambda R}{2\sigma_{\mathrm{s}_y}}. \tag{2.27}$$

The coherence volume is defined as the volume spanned by the coherence lengths in all three spatial dimensions:

$$V_\mathrm{coh} = \xi_{\mathrm{t}x} \cdot \xi_{\mathrm{t}y} \cdot \xi_\mathrm{l} \tag{2.28}$$

At the coherence beamlines of the synchrotrons utilised in the course of this thesis, ξ_l was on the order of few microns while the transversal coherence lengths were on the order of 5–200 µm (Sinha et al. 2014). Comparing to the maximum path length difference (see Eq. (2.21)) we can see that the longitudinal coherence length is typically smaller than the maximum path length difference. This implies that coherence is partially lost. However, as the maximum path length difference only accounts for the most extreme case, large parts of the illuminated sample volume still scatter coherently. To evaluate the degree of coherence of the scattered radiation, we can think of the sample as being composed of individual scattering volumes with volume V_coh, each scattering coherently. The degree of coherence, also called contrast factor, can be roughly estimated by

$$\beta \approx \frac{V'_\mathrm{coh}}{V_\mathrm{illum}}, \tag{2.29}$$

where V_{illum} is the total sample volume illuminated by the beam and V'_{coh} is the volume spanned by either the coherence length or the beam size in each dimension, whichever smaller. If the transversal coherence widths are larger than the beam diameter, this implies that

$$\beta \approx \frac{\xi_{\mathrm{l}}}{W}. \tag{2.30}$$

The contrast can be approached more formally by considering the statistics of the scattered radiation. If the scattered radiation is fully coherent and the scattering amplitudes and phases are statistically independent, the probability distribution of the intensity of the resulting speckle patterns can be described by Eq. (2.31)

$$P(I) = \frac{\mathrm{e}^{-I/\langle I\rangle}}{\langle I\rangle}, \tag{2.31}$$

where $\langle I\rangle$ is the mean intensity (Goodman 2007). With the standard deviation $\sigma = \sqrt{\langle I^2\rangle - \langle I\rangle^2}$, we obtain the contrast factor $\beta = \sigma^2/\langle I\rangle^2$. We see that the contrast factor is unity for fully coherent radiation.

If we now have independently scattering subvolumes of the sample, the scattered radiation is only partially coherent and the statistics of the speckle intensities change accordingly. For M independent speckles in a continuous speckle pattern, the intensity distribution can be described by

$$P(I) = \left(\frac{MI}{\langle I\rangle}\right)^M \frac{\mathrm{e}^{-MI/\langle I\rangle}}{\Gamma(M)I}, \tag{2.32}$$

with the gamma function $\Gamma(M)$. Now the standard deviation is $\sigma = \langle I\rangle/\sqrt{M}$ and consequently the contrast factor is $\beta = 1/M$. We will see later on, that the SNR in the obtained intensity patterns is proportional to the contrast and come back to the contrast factor in Sect. 4.2.

2.2 Deducing Real-Space Time-Correlations from Intensity Pattern Series

As mentioned before, it is not possible to *directly* obtain real-space information from the scattering pattern. However, the changes in the pattern can be related to the changes which take place in real space. We will see how correlation functions can be used to describe these changes and to translate the intensity information into real-space information.

2.2.1 Van Hove Pair Correlation Function

Information about the dynamics of the particles of a material can be obtained by assessing the probability that a particle will be at $\vec{r}$ at time $t' + \Delta t$ given that a particle (the same or another) was at the origin at time t'. Formally, this can be written as

$$G(\vec{r}, \Delta t) = \left\langle \frac{1}{N} \sum_{a,b} \delta\left[\vec{r} - \left(\vec{R}_a(t') - \vec{R}_b(t' + \Delta t)\right)\right] \right\rangle_{t'} \tag{2.33}$$

and is known as the van Hove pair correlation function. Here, the indices of summation a and b run over all N particles with position vectors $\vec{R}_a$ and $\vec{R}_b$, but without summing over same indices (Hansen and McDonald 2006).

A very common function in dynamic light scattering is the so-called dynamic structure factor

$$S(\vec{q}, t) := \frac{1}{N} \sum_{a,b} \left\langle \mathrm{e}^{\mathrm{i}\vec{q}\left(\vec{R}_a(t') - \vec{R}_b(t'+t)\right)} \right\rangle_{t'}, \tag{2.34}$$

with summation indices running over all particles.

We can see that this function is the Fourier transform of the van Hove pair correlation function:

$$\begin{aligned} S(\vec{q}, t) &= \frac{1}{N} \sum_{a,b} \int \mathrm{d}\vec{r} \left\langle \mathrm{e}^{\mathrm{i}\vec{q}\vec{r}} \delta\left[\vec{r} - \left(\vec{R}_a(t') - \vec{R}_b(t' + t)\right)\right] \right\rangle_{t'} \\ &= \int \mathrm{d}\vec{r}\, \mathrm{e}^{\mathrm{i}\vec{q}\vec{r}} \left\langle \frac{1}{N} \sum_{a,b} \delta\left[\vec{r} - \left(\vec{R}_a(t') - \vec{R}_b(t' + t)\right)\right] \right\rangle_{t'} \\ &= \int \mathrm{d}\vec{r}\, \mathrm{e}^{\mathrm{i}\vec{q}\vec{r}} G(\vec{r}, t) \\ &= \mathcal{F}(G(\vec{r}, t)) \end{aligned} \tag{2.35}$$

Here it is disregarded that the original definition of the van Hove pair correlation function does not include summing over same indices. The dynamic structure factor is also known as intermediate scattering function. In XPCS it is not directly measurable. We will see that we can put it in context to the autocorrelation of the electrical field and in turn with the intensity.

2.2.2 Autocorrelation Functions

A generic time autocorrelation function can be seen as a generalisation of the time average:

$$\langle A(t)A(t+\Delta t)\rangle = \lim_{T\to\infty}\frac{1}{T}\int_{-\frac{T}{2}}^{\frac{T}{2}} \mathrm{d}t\, A(t)A(t+\Delta t) \tag{2.36}$$

The dependence of the autocorrelation function on the time lag Δt is an indicator for how fast a signal decorrelates or in other words, how fast a pattern decays. We can see that the autocorrelation function will always start at $\langle A^2\rangle$ for $\Delta t = 0$ and decay to $\langle A\rangle^2$ for $\Delta t \to \infty$, as there should be no connection between a signal at one point in time and at another at a much later time, as we are looking at non-periodic signals (see Fig. 2.8). Typically, this dependence will follow some kind of exponential decay, as we will see later on.

An important function is the normalised autocorrelation function of the electrical field

$$g^{(1)}(\vec{q},\Delta t) := \frac{\langle E(\vec{q},t)E^*(\vec{q},t+\Delta t)\rangle}{\langle E(\vec{q},t)E^*(\vec{q},t)\rangle}. \tag{2.37}$$

We can see that this function is connected to the van Hove pair correlation function via the dynamic structure factor:

$$\begin{aligned} g^{(1)}(\vec{q},\Delta t) &= \frac{\left\langle \left(\sum_{i=1}^{N} a_i \mathrm{e}^{\mathrm{i}\vec{q}\vec{r}_i(t)}\right)\left(\sum_{j=1}^{N} a_j^* \mathrm{e}^{-\mathrm{i}\vec{q}\vec{r}_j(t+\Delta t)}\right)\right\rangle}{\left\langle \left(\sum_{i=1}^{N} a_i \mathrm{e}^{\mathrm{i}\vec{q}\vec{r}_i(t)}\right)\left(\sum_{j=1}^{N} a_j^* \mathrm{e}^{-\mathrm{i}\vec{q}\vec{r}_j(t)}\right)\right\rangle} \\ &= \frac{\left\langle \sum_{i,j} a_i a_j^* \mathrm{e}^{\mathrm{i}\vec{q}\left(\vec{r}_i(t)-\vec{r}_j(t+\Delta t)\right)}\right\rangle}{\left\langle \sum_{i,j} a_i a_j^* \mathrm{e}^{\mathrm{i}\vec{q}\left(\vec{r}_i(t)-\vec{r}_j(t)\right)}\right\rangle} \\ &= \frac{\sum_{i,j}\left\langle \mathrm{e}^{\mathrm{i}\vec{q}\left(\vec{r}_i(t)-\vec{r}_j(t+\Delta t)\right)}\right\rangle a_i a_j^*}{\sum_{i,j}\left\langle \mathrm{e}^{\mathrm{i}\vec{q}\left(\vec{r}_i(t)-\vec{r}_j(t)\right)}\right\rangle a_i a_j^*} \end{aligned} \tag{2.38}$$

For identical scattering lengths, this simplifies to

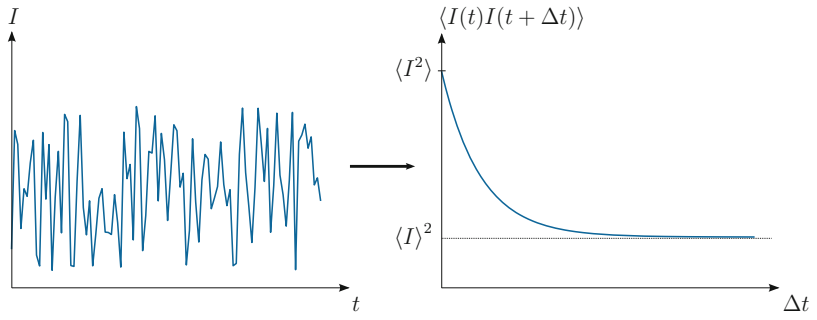

Fig. 2.8 *Left* Scattered intensity from a diffusive process. *Right* The autocorrelation function of the scattering intensity decays from $\langle I^2\rangle$ to $\langle I\rangle^2$ with increasing time lag Δt

$$g^{(1)}(\vec{q},\Delta t) = \frac{\sum_{i,j}\left\langle \mathrm{e}^{\mathrm{i}\vec{q}\left(\vec{r}_i(t)-\vec{r}_j(t+\Delta t)\right)}\right\rangle}{\sum_{i,j}\left\langle \mathrm{e}^{\mathrm{i}\vec{q}\left(\vec{r}_i(t)-\vec{r}_j(t)\right)}\right\rangle} = \frac{S(\vec{q},t)}{S(\vec{q},0)}. \tag{2.39}$$

2.2.3 Link Between Autocorrelation Functions of Measured Intensities and Those of Real-Space Information

As we have seen, we can directly deduce the van Hove pair correlation function from $g^{(1)}(\vec{q},\Delta t)$. As mentioned before, the electric field is not directly measurable. Instead, the intensity is experimentally obtained. We can link both dimensions using the normalised intensity autocorrelation function:

$$\begin{aligned} g^{(2)}(\vec{q},\Delta t) &:= \frac{\langle I(\vec{q},t)I(\vec{q},t+\Delta t)\rangle}{\langle I(\vec{q},t)\rangle^2} \\ &= \frac{\langle E(\vec{q},t)E^*(\vec{q},t)E(\vec{q},t+\Delta t)E^*(\vec{q},t+\Delta t)\rangle}{\langle E(\vec{q},t)E^*(\vec{q},t)\rangle^2} \end{aligned} \tag{2.40}$$

In the XPCS experiment, the time averaged time correlation function of the intensity is obtained. In equilibrated samples, the ergodic theorem should hold, claiming that the time average equals the ensemble average. This is true for systems where a representative fraction of states is reached within the measurement time.

The autocorrelation function can be simplified using Isserlis' theorem (Isserlis 1918), also known as Wick's theorem (Wick 1950), as the scattered amplitudes follow Gaussian statistics:

$$\begin{aligned} &\left\langle E(\vec{q},t)E^*(\vec{q},t)E(\vec{q},t+\Delta t)E^*(\vec{q},t+\Delta t)\right\rangle \\ &\quad= \left\langle E(\vec{q},t)E^*(\vec{q},t)\right\rangle\left\langle E(\vec{q},t+\Delta t)E^*(\vec{q},t+\Delta t)\right\rangle \\ &\qquad+ \left\langle E(\vec{q},t)E(\vec{q},t+\Delta t)\right\rangle\left\langle E^*(\vec{q},t)E^*(\vec{q},t+\Delta t)\right\rangle \\ &\qquad+ \left\langle E(\vec{q},t)E^*(\vec{q},t+\Delta t)\right\rangle\left\langle E^*(\vec{q},t)E(\vec{q},t+\Delta t)\right\rangle \end{aligned} \tag{2.41}$$

With $\langle EE\rangle \propto \left\langle \mathrm{e}^{-i2\omega t}\right\rangle = 0$ and $\langle E^*E^*\rangle \propto \left\langle \mathrm{e}^{-i2\omega t}\right\rangle = 0$, this simplifies to

$$\begin{aligned} &\left\langle E(\vec{q},t)E^*(\vec{q},t)\right\rangle\left\langle E(\vec{q},t+\Delta t)E^*(\vec{q},t+\Delta t)\right\rangle \\ &\qquad+ \left\langle E(\vec{q},t)E^*(\vec{q},t+\Delta t)\right\rangle\left\langle E^*(\vec{q},t)E(\vec{q},t+\Delta t)\right\rangle \\ &\quad= \left\langle E(\vec{q},t)E^*(\vec{q},t)\right\rangle^2 + \left\langle E(\vec{q},t)E^*(\vec{q},t+\Delta t)\right\rangle^2. \end{aligned} \tag{2.42}$$

This can be used to connect $g^{(1)}$ and $g^{(2)}$:

$$g^{(2)}(\vec{q}, \Delta t) = 1 + \left| \frac{\langle E(\vec{q}, t) E^*(\vec{q}, t + \Delta t) \rangle}{\langle E(\vec{q}, t) E^*(\vec{q}, t) \rangle} \right|^2 = 1 + |g^{(1)}(\vec{q}, \Delta t)|^2 \tag{2.43}$$

This connection is only true for perfect coherence under ideal conditions. In the experimental environment, the relation has to be slightly modified:

$$g^{(2)}(\vec{q}, \Delta t) = 1 + \beta |g^{(1)}(\vec{q}, \Delta t)|^2 \tag{2.44}$$

The factor β is called contrast (see Sect. 2.1.3) and also Siegert or coherence factor (Sutton 2008) and accounts for the fact that the used radiation is not perfectly coherent initially and also coherence is lost by optical elements of the setup. The coherence factor can be calculated for the optics of a given setup or experimentally obtained, measuring a sample with no dynamics. It can vary between 0 and 1 and decreases with increasing scattering angle (see Fig. 2.9).

2.3 Unravelling Atomic Dynamics

Now that we know how to obtain real-space correlations (namely $g^{(1)}(\vec{q}, \Delta t)$, the autocorrelation of the electrical field), we can find models which are able to describe

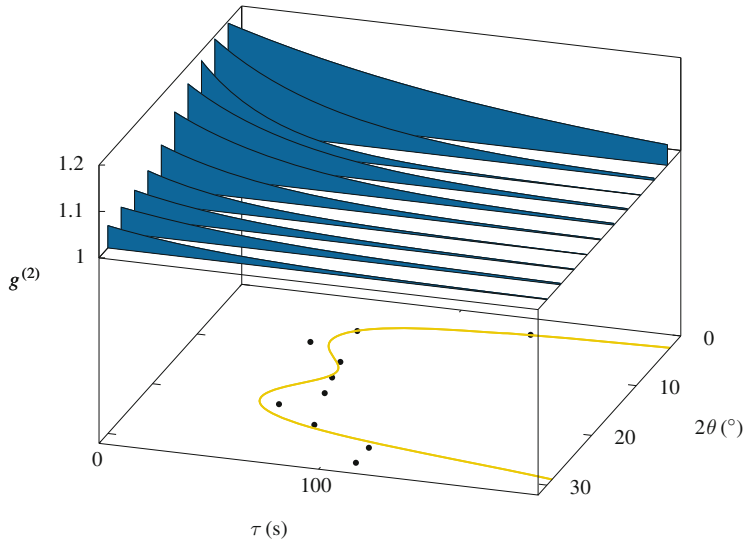

Fig. 2.9 Dependence of the intensity autocorrelation function on scattering angle and time lag. The coherence factor of each measurement is the axis intercept of the according autocorrelation curve. The plot on the *bottom* of the graph shows the corresponding correlation times and a fit to these decay times

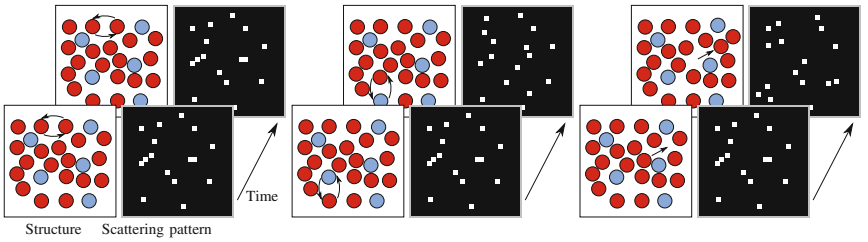

Fig. 2.10 Detectable dynamics with aXPCS. Each column shows a structural change and the according scattering pattern over time. *Left* Two atoms of the same atomic species exchange positions. No change in scattering pattern occurs, thus this exchange is not detectable. *Middle* Exchange of two atoms of different elements. The scattering pattern changes and the exchange is detectable. *Right* Translation of an atom. The scattering pattern changes thus the movement of the atom is detectable

these correlations and provide deeper insight into the actual atomic dynamics. As shown in Fig. 2.10, aXPCS is not sensitive to all atomic movements. In fact it can be seen as a remarkable property of this method that it can be used to specifically focus on the translatory movement of atoms. It should be further noted that in the context of this thesis, the term *dynamics* describes solely diffusion and excludes other dynamic phenomena like e.g. phonons, which are taking place on entirely different time scales (see Fig. 1.3).

2.3.1 Continuous Diffusion

Assuming a continuous medium, the consequences of diffusion for the concentration of an atomic species can be described by Fick's laws. As the self-correlation function G_s can be seen as a representation of the particle concentration, it has to obey Fick's second law:

$$\frac{\partial G_\mathrm{s}(\vec{r},t)}{\partial t} = D\nabla^2 G_\mathrm{s}(\vec{r},t) \tag{2.45}$$

Here, D is called the self-diffusion coefficient. With $G_\mathrm{s}(\vec{r},0) = \delta(\vec{r}\,)$ and assuming that the particle is followed over a longer range relative to the atomic distances, the solution of Eq. (2.45) is the Gaussian function:

$$G_\mathrm{s}(\vec{r},t) = \frac{1}{(4\pi Dt)^{3/2}} \mathrm{e}^{-\frac{r^2}{4Dt}} \tag{2.46}$$

The mean square displacement of a particle can be expressed in terms of the diffusion coefficient:

$$\left\langle \vec{r}^{\,2}(t) \right\rangle := \int r^2 G_\mathrm{s}(\vec{r},t)\mathrm{d}\vec{r} \tag{2.47}$$

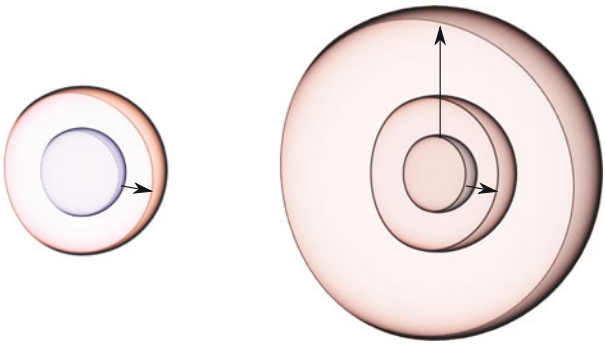

Fig. 2.11 Visualisation of the fixed jump lengths and isotropic jump directions of the Chudley–Elliott model. *Left* Single jump Chudley–Elliott model. *Right* Two-jump Chudley–Elliott model

Solving this equation for isotropic media (i.e. in spherical coordinates) leads to

$$\left\langle \vec{r}^{\,2}(t) \right\rangle = \frac{4\pi}{(4\pi Dt)^{3/2}} \int_0^\infty r^4 \mathrm{e}^{-\frac{r^2}{4Dt}} \mathrm{d}r = 6Dt. \tag{2.48}$$

Following atomic motion on smaller scales relative to the atomic distances, the Gaussian approximation is not valid anymore. A microscopic model has to take into account the discretised nature of the atomic motion (Figs. 2.11 and 2.12).

2.3.2 *Jump Diffusion: Chudley–Elliott Model*

A mechanism which can describe atomic-scale transport is the so-called jump diffusion. It is based on the assumption that atoms stay at a fixed position most of the time, only vibrating around this position. Transport happens by very fast translatory motions, which are uncorrelated in time and so much faster than the time the atom spends at a fixed position (the so-called mean residence time τ_0), that these motions can be described as (quasi-instantaneous) jumps. Another model assumption is that the atomic jumps are isotropic and have the same specific distance. This model was first studied in detail by Chudley and Elliott (1961) who derived the van Hove pair correlation function for a diffusion process under these assumptions. The derivation is based on the master equation for the probability of finding an atom at position $\vec{r}$,

$$\frac{\partial P(\vec{r},t)}{\partial t} = -\frac{1}{\tau_0} P(\vec{r},t) + \frac{1}{N\tau_0} \sum_j P(\vec{r}+\vec{r}_j,t), \tag{2.49}$$

where the index of summation j runs over all N potential positions $\vec{r}_j$ the atom could jump from.

Setting $G(\vec{r},0) = \delta(\vec{r})$, this equation is solved by the van Hove pair correlation function. Introducing the Fourier transform

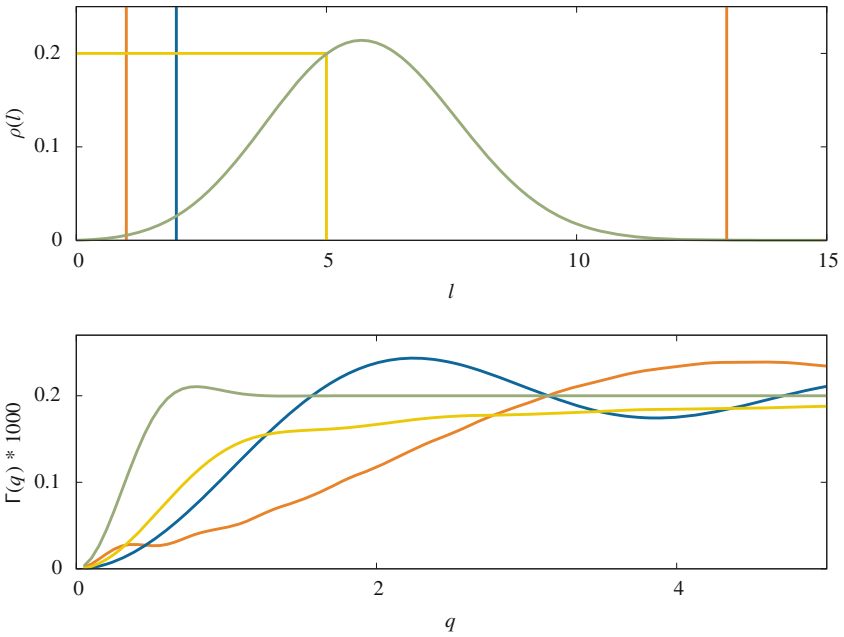

Fig. 2.12 Jump length distributions (*upper plot*) and inverse correlation times (*lower plot*) for the single jump Chudley–Elliott model (*blue line*, parameter value $l = 2$), the two-jump Chudley–Elliott model (*orange line*, parameter values $l_1 = 1, l_2 = 13, \omega_1 = 0.9$), the Jobic model (*green line*, $d_0 = 5, r_0 = 2$) and for uniformly distributed jumps (*yellow line*, $l_{\max} = 5$). All inverse correlation times were plotted using $\tau_0^{-1} = 2 \times 10^{-4}$

$$P(\vec{r}, t) = \int \tilde{P}(\vec{q}, t) \mathrm{e}^{-\mathrm{i}\vec{q}\vec{r}} \mathrm{d}\vec{q} \tag{2.50}$$

and rewriting the master equation accordingly leads to a differential equation:

$$\frac{\partial \left(\int \tilde{P}(\vec{q}, t) \mathrm{e}^{-\mathrm{i}\vec{q}\vec{r}} \mathrm{d}\vec{q} \right)}{\partial t} = -\frac{1}{\tau_0} \int \tilde{P}(\vec{q}, t) \mathrm{e}^{-\mathrm{i}\vec{q}\vec{r}} \mathrm{d}\vec{q} + \frac{1}{N\tau_0} \sum_j \int \tilde{P}(\vec{q}, t) \mathrm{e}^{-\mathrm{i}\vec{q}(\vec{r}+\vec{r}_j)} \mathrm{d}\vec{q} \tag{2.51}$$

This equation can be solved by an exponential decay function. Setting

$$\tilde{P}(\vec{q}, t) = \mathrm{e}^{-\Gamma(\vec{q})t}, \tag{2.52}$$

the equation reads

$$\frac{\partial \left(\int \mathrm{e}^{-\Gamma(\vec{q})t - \mathrm{i}\vec{q}\vec{r}} \mathrm{d}\vec{q} \right)}{\partial t} = -\frac{1}{\tau_0} \int \mathrm{e}^{-\Gamma(\vec{q})t - \mathrm{i}\vec{q}\vec{r}} \mathrm{d}\vec{q} + \frac{1}{N\tau_0} \sum_j \int \mathrm{e}^{-\Gamma(\vec{q})t - \mathrm{i}\vec{q}(\vec{r}+\vec{r}_j)} \mathrm{d}\vec{q}. \tag{2.53}$$

The decay parameter $\Gamma(\vec{q}\,)$ is also known as inverse correlation time τ^{-1} or line width. After differentiating, we get:

$$\begin{aligned}\int (-\Gamma(\vec{q}\,))\,\mathrm{e}^{-\Gamma(\vec{q}\,)t-\mathrm{i}\vec{q}\vec{r}}\mathrm{d}\vec{q} &= -\frac{1}{\tau_0}\int \mathrm{e}^{-\Gamma(\vec{q}\,)t-\mathrm{i}\vec{q}\vec{r}}\mathrm{d}\vec{q} + \frac{1}{N\tau_0}\sum_j \int \mathrm{e}^{-\Gamma(\vec{q}\,)t-\mathrm{i}\vec{q}\vec{r}}\cdot\mathrm{e}^{-\mathrm{i}\vec{q}\vec{r}_j}\mathrm{d}\vec{q} \\ &= -\frac{1}{\tau_0}\int \mathrm{e}^{-\Gamma(\vec{q}\,)t-\mathrm{i}\vec{q}\vec{r}}\mathrm{d}\vec{q} + \frac{1}{N\tau_0}\sum_j \int \mathrm{e}^{-\Gamma(\vec{q}\,)t-\mathrm{i}\vec{q}\vec{r}}\cdot\mathrm{e}^{-\mathrm{i}\vec{q}\vec{r}_j}\mathrm{d}\vec{q} \\ &= \int \left(-\frac{1}{\tau_0} + \frac{1}{N\tau_0}\sum_j \mathrm{e}^{-\mathrm{i}\vec{q}\vec{r}_j}\right)\mathrm{e}^{-\Gamma(\vec{q}\,)t-\mathrm{i}\vec{q}\vec{r}}\mathrm{d}\vec{q}\end{aligned} \tag{2.54}$$

Thus we obtain a solution for the functional dependence of the decay on the scattering vector:

$$\Gamma(\vec{q}\,) = \frac{1}{N\tau_0}\sum_j \left(1 - \mathrm{e}^{\mathrm{i}\vec{q}\vec{r}_j}\right) \tag{2.55}$$

Now we can link the autocorrelation functions to the scattering vector:

$$g^{(1)}(\vec{q},\,\Delta t) = \frac{S(\vec{q},\,\Delta t)}{S(\vec{q},\,0)} = \frac{\mathcal{F}(G(\vec{r},\,\Delta t))}{\mathcal{F}(G(\vec{r},\,0))} = \frac{\tilde{P}(\vec{q},\,\Delta t)}{\tilde{P}(\vec{q},\,0)} = \mathrm{e}^{-\Gamma(\vec{q}\,)\Delta t} \tag{2.56}$$

$$g^{(2)}(\vec{q},\,\Delta t) = 1 + \beta|g^{(1)}|^2 = 1 + \beta\mathrm{e}^{-2\Gamma(\vec{q}\,)\Delta t} \tag{2.57}$$

Taking into account the model assumption of a fixed jump length l and an isotropic jump distribution, we can rewrite $\Gamma(\vec{q}\,)$ in integral form:

$$\Gamma(q) = \frac{1}{\tau_0}\frac{\int_0^{2\pi}\int_0^{\pi}\left(1 - \mathrm{e}^{\mathrm{i}ql\cos\theta}\right)\sin\theta\,\mathrm{d}\theta\,\mathrm{d}\phi}{\int_0^{2\pi}\int_0^{\pi}\sin\theta\,\mathrm{d}\theta\,\mathrm{d}\phi} \tag{2.58}$$

Substituting $u = \cos\theta$ and using $\frac{\mathrm{e}^{\mathrm{i}ql} - \mathrm{e}^{\mathrm{i}ql}}{2\mathrm{i}} = \sin(ql)$, we obtain the single jump Chudley–Elliott form:

$$\begin{aligned}\Gamma(q) &= \frac{1}{\tau_0}\frac{2\pi\int_{-1}^{1}\left(1 - \mathrm{e}^{\mathrm{i}qlu}\right)\,\mathrm{d}u}{4\pi} \\ &= \frac{1}{2\tau_0}\left(2 - \frac{\mathrm{e}^{\mathrm{i}ql} - \mathrm{e}^{\mathrm{i}ql}}{\mathrm{i}ql}\right) \\ &= \frac{1}{\tau_0}\left(1 - \frac{\sin(ql)}{ql}\right)\end{aligned} \tag{2.59}$$

In the limit of very small angles (or more precisely $ql \ll 1$), the sine function can be expanded and the inverse correlation time $\Gamma(q)$ simplifies to

$$\lim_{(ql)\to 0} \Gamma(q) = \frac{1}{\tau_0}\left(1 - \frac{ql - \frac{(ql)^3}{3!} + \cdots}{ql}\right) \approx \frac{q^2 l^2}{6\tau_0}, \tag{2.60}$$

often described in the form $\Gamma(q) = Dq^2$, where D is called diffusion coefficient.

Keeping the criterion of isotropic jumps but relaxing the criterion of a single jump length, Eq. (2.59) can be generalised (Jobic 2000). Using a jump length distribution $\rho(l)$, Eq. (2.59) can be rewritten in the form

$$\Gamma(q) = \frac{1}{\tau_0} \frac{\int \left(1 - \frac{\sin(ql)}{ql}\right) \rho(l)\, \mathrm{d}l}{\int \rho(l)\, \mathrm{d}l}. \tag{2.61}$$

If $\rho(l)$ is normalised, this simplifies to

$$\Gamma(q) = \frac{1}{\tau_0}\left(1 - \int_0^\infty \frac{\sin(ql)}{ql} \rho(l)\, \mathrm{d}l\right). \tag{2.62}$$

2.3.3 *Extensions of the Chudley–Elliott Model*

We can use the results obtained by the generalisation shown in Eq. (2.62) to derive $\Gamma(q)$ for other jump geometries.

Uniformly Distributed Jumps

The Chudley–Elliott model is one extreme of jump distributions, assuming that only one jump distance is possible. Another extreme can be constructed assuming that all jump lengths up to a certain distance are equally probable:

$$\rho(l) = \begin{cases} \frac{1}{l_{\max}} & 0 < l < l_{\max} \\ 0 & \text{otherwise} \end{cases} \tag{2.63}$$

This leads to

$$\begin{aligned} \Gamma(q) &= \frac{1}{\tau_0}\left(1 - \frac{1}{l_{\max}} \int_0^{l_{\max}} \frac{\sin(ql)}{ql}\, \mathrm{d}l\right) \\ &= \frac{1}{\tau_0}\left(1 - \frac{1}{l_{\max}} \frac{\mathrm{Si}(ql_{\max})}{q}\right), \end{aligned} \tag{2.64}$$

where the sine integral $\mathrm{Si}(x)$ can be calculated numerically or approximated by a truncated series expansion.

Jobic Model

Jobic (2000) introduced a jump length distribution similar to a model proposed by Hall and Ross (1981). In this model, the jump lengths follow the distribution

$$\rho(l) = \frac{l}{d_0 r_0 \sqrt{2\pi}} \exp\left(-\frac{(l-d_0)^2}{2r_0^2}\right). \tag{2.65}$$

Here, d_0 represents the jump distance and r_0 the delocalisation of an atom from its site. The inverse correlation time is then given by

$$\begin{aligned}\Gamma(q) &= \frac{1}{\tau_0}\left(1 - \frac{1}{q d_0 r_0 \sqrt{2\pi}} \int_0^\infty \sin(ql) \exp\left(-\frac{(l-d_0)^2}{2r_0^2}\right) \mathrm{d}l\right) \\ &= \frac{1}{\tau_0}\left(1 - \frac{\sin(qd_0)}{qd_0} \exp\left(-\frac{q^2 r_0^2}{2}\right)\right).\end{aligned} \tag{2.66}$$

Two-Jump Chudley–Elliott Model

A straightforward way to allow for more than one jump distance imposed by the Chudley–Elliott model is to include a second independent jump. This can be achieved with the following jump distribution:

$$\rho(l) = \omega_1 \delta(l - l_1) + \omega_2 \delta(l - l_2) \tag{2.67}$$

with the relative weights ω_i of the jump lengths l_i, where $\omega_1 + \omega_2 = 1$. With this distribution, the inverse correlation time takes the form

$$\Gamma(q) = \frac{1}{\tau_0}\left(1 - \omega_1 \frac{\sin(ql_1)}{ql_1} - (1-\omega_1)\frac{\sin(ql_2)}{ql_2}\right). \tag{2.68}$$

2.4 Applying aXPCS to Diffusion in Glasses

Studying atomic diffusion in glasses compared to diffusion in crystals poses additional challenges as the structure is much less defined and the underlying mechanisms of diffusion are much less clear. We will have a look at some effects typically encountered when studying glasses and see how they influence the way the dynamics can be described.

2.4.1 Influence of Different Scattering Species

In contrast to crystalline materials, glasses do not show a distinct long-range order which would result in a Bragg peak. Instead, a broad distribution of scattering

intensity is observed. This poses additional challenge to interpreting aXPCS data, as the scattered intensity of the rather immobile matrix can not be easily separated from the scattering of the diffusing atoms under consideration. In principle, the measured intensity (also called structure factor) can be represented by the weighted sum of partial structure factors (Soper 2005)

$$S(q) = \sum_{\alpha,\beta \geq \alpha} (2 - \delta_{\alpha\beta}) c_\alpha c_\beta f_\alpha f_\beta S_{\alpha\beta}(q), \tag{2.69}$$

where c_α is the atomic fraction of species α and f_α is the scattering length.

In some cases, like in lead silicate glass (see Chap. 5), the huge difference in scattering strength of the lead atom compared to Si and O allows to interpret the measurements like a system of one element species. Thus we can follow mainly Pb atoms in their movement and neglect the other atoms in the sample. This is one of the reasons why lead silicate glass is an ideal candidate as a starting point for studying atomic diffusion in glasses.

2.4.2 Kohlrausch Exponent

A pure exponential decay as derived in Eq. (2.57) can often only be observed in aXPCS experiments when a single process is active. When multiple dynamic processes with similar decay rates are observed at the same time (e.g. when in some regions atoms move with different diffusion rates than in the other regions of the material, see Fig. 2.13), they cannot be easily separated. Instead, the stretching parameter

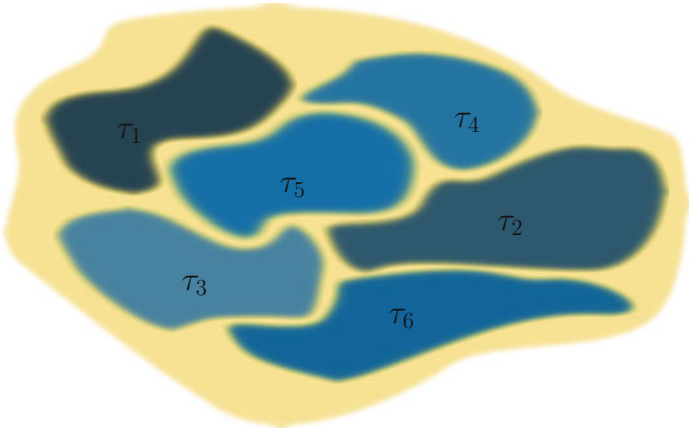

Fig. 2.13 Visualisation of a glass sample with different regions distinguished by the mean residence time which is predominant in each region. Due to macroscopic ageing, parts of the sample can be in different evolution levels of the dynamics. Thus the same type of process can be unchanged over the measurement time but have spatially different diffusion speeds

α, also called KWW parameter, can be used. This empirical parameter has been introduced in the 19th century by Kohlrausch and resurrected by Williams and Watts (1970) and can be seen as a straightforward approximation for the sum of multiple exponentials. With this approximation, the intensity autocorrelation function takes the form

$$g^{(2)}(\vec{q}, \Delta t) = 1 + \beta \mathrm{e}^{-2(\Gamma(\vec{q})\Delta t)^{\alpha}}, \tag{2.70}$$

with the inverse correlation time $\Gamma(\vec{q}) = \frac{1}{\tau(\vec{q})}$.

A value of $\alpha = 1$ just leads to the normal behaviour derived in Eq. (2.57). In Fig. 2.14, the effect of applying the KWW function is shown. The stretching parameter α can be less than one (in that case, the KWW function is also called stretched exponential function) for constrained or subdiffusive motion of particles (Pontoni et al. 2003; Guo et al. 2012) or for dynamics where several processes are active. A value of $\alpha > 1$ (where the KWW function is also called compressed exponential function) can indicate non-equilibrium dynamics (Madsen et al. 2010; Leitner et al. 2012; Ruta et al. 2012).

2.4.3 Short-Range Order Correction

As we have seen, the measured q dependence of the correlation time allows to test mathematical models of different diffusion processes. We have also seen that aXPCS

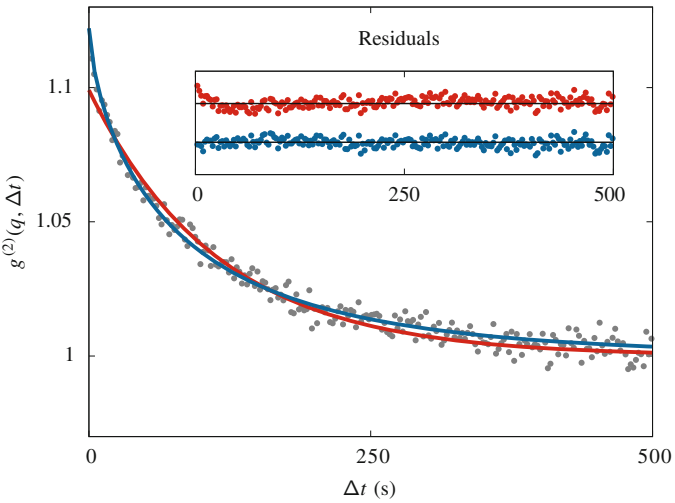

Fig. 2.14 Comparison of the autocorrelation function of experimental intensity values and residuals using the KWW function with different KWW parameters. In the main plot, the *red line* depicts the pure exponential decay with $\alpha = 1$, while the *blue line* is a fit of the KWW function with $\alpha < 1$ to the data. The *inset* shows the residuals which are the subtraction of the fitted curve from the data points. The stretched exponential decay function clearly fits the data better than the pure exponential decay

is a coherent method or in other words, it takes into account the diffusion of all atoms rather than following one single atom only.

In addition to the scattering described so far, there are further effects which influence the intensity due to the short-range order. This spatial correlation of the diffusing atoms to other atoms in their direct vicinity typically results in a broad intensity peak, the so-called structure peak. This effect is known as the de Gennes narrowing, first described qualitatively for coherent QENS (De Gennes 1959). It basically states that those species whose dynamics are slower than the dynamics of other diffusing species will form longer-living structures, which will in turn lead to a higher scattering intensity in the q range corresponding to the size of these structures. Thus the q dependence of the scattering intensity $S_{\mathrm{SRO}}(\vec{q}\,)$ gives additional information on the diffusion rate of atoms in the material.

The diffusion models described before are in fact valid for incoherent methods and have to be modified for a coherent method like aXPCS if the system studied is ordered. The diffuse scattering under short-range order has been investigated in a linear approximation by Sinha and Ross (1988) and is discussed in detail in Leitner and Vogl (2011). For a weak short-range ordering, the coherent inverse correlation time can be described in terms of the incoherent inverse correlation time:

$$\tau_{\mathrm{coh}}^{-1}(\vec{q}\,) = \frac{\tau_{\mathrm{inc}}^{-1}(\vec{q}\,)}{S_{\mathrm{SRO}}(\vec{q}\,)} \tag{2.71}$$

This correlation time τ_{coh} can now be compared with the results of coherent experiments, where $\tau_{\mathrm{inc}}(\vec{q}\,)$ is the correlation time which would be obtained with an incoherent scattering method.

References

Abernathy, D. L., Grübel, G., Brauer, S., McNulty, I., Stephenson, G. B., Mochrie, S. G. J., et al. (1998). Small-angle X-ray scattering using coherent undulator radiation at the ESRF. *Journal of Synchrotron Radiation*, *5 (Part 1)*, 37–47.

Chudley, C. T., & Elliott, R. J. (1961). Neutron scattering from a liquid on a jump diffusion model. *Proceedings of the Physical Society London*, *77*(2), 353–361.

De Gennes, P. G. (1959). Liquid dynamics and inelastic scattering of neutrons. *Physica*, *25*(7–12), 825–839.

Goodman, J. W. (2007). *Speckle phenomena in optics: theory and applications*. Englewood: Roberts & Company.

Guo, H., Bourret, G., Lennox, R. B., Sutton, M., Harden, J. L., & Leheny, R. L. (2012). Entanglement-controlled subdiffusion of nanoparticles within concentrated polymer solutions. *Physical Review Letters*, *109*(5), 055901.

Hall, P. L., & Ross, D. K. (1981). Incoherent neutron scattering functions for random jump diffusion in bounded and infinite media. *Molecular Physics*, *42*(3), 673–682.

Hansen, J.-P., & McDonald, I. R. (2006). *Theory of simple liquids*. London: Elsevier.

Isserlis, L. (1918). On a formula for the product-moment coefficient of any order of a normal frequency distribution in any number of variables. *Biometrika*, *12*(1–2), 134–139.

Jobic, H. (2000). Diffusion studies using quasi-elastic neutron scattering. In N. K. Kanellopoulos (Ed.), *Recent advances in gas separation by microporous ceramic membranes* (Vol. 6, pp. 109–137). Amsterdam: Elsevier.

Leitner, M., & Vogl, G. (2011). Quasi-elastic scattering under short-range order: the linear regime and beyond. *Journal of Physics: Condensed Matter*, *23*(25), 254206.

Leitner, M., Sepiol, B., Stadler, L.-M., & Pfau, B. (2012). Time-resolved study of the crystallization dynamics in a metallic glass. *Physical Review B*, *86*(6), 064202.

Madsen, A., Leheny, R. L., Guo, H., Sprung, M., & Czakkel, O. (2010). Beyond simple exponential correlation functions and equilibrium dynamics in x-ray photon correlation spectroscopy. *New Journal of Physics*, *12*(5), 055001.

Marchesini, S., He, H., Chapman, H. N., Hau-Riege, S. P., Noy, A., Howells, M. R., et al. (2003). X-ray image reconstruction from a diffraction pattern alone. *Physical Review B*, *68*(14), 140101.

Pontoni, D., Narayanan, T., Petit, J.-M., Grübel, G., & Beysens, D. (2003). Microstructure and dynamics near an attractive colloidal glass transition. *Physical Review Letters*, *90*(18), 188301.

Ruta, B., Chushkin, Y., Monaco, G., Cipelletti, L., Pineda, E., Bruna, P., et al. (2012). Atomic-scale relaxation dynamics and aging in a metallic glass probed by x-ray photon correlation spectroscopy. *Physical Review Letters*, *109*, 165701.

Sandy, A. R., Lurio, L. B., Mochrie, S. G. J., Malik, A., Stephenson, G. B., Pelletier, J. F., et al. (1999). Design and characterization of an undulator beamline optimized for small-angle coherent x-ray scattering at the advanced photon source. *Journal of Synchrotron Radiation*, *6*(6), 1174–1184.

Sinha, S. K., & Ross, D. K. (1988). Self-consistent density response function method for dynamics of light interstitials in crystals. *Physica B*, *149*(1–3), 51–56.

Sinha, S. K., Jiang, Z., & Lurio, L. B. (2014). X-ray photon correlation spectroscopy studies of surfaces and thin films. *Advanced Materials*, *26*(46), 7764–7785.

Soper, A. (2005). Partial structure factors from disordered materials diffraction data: An approach using empirical potential structure refinement. *Physical Review B*, *72*(10), 104204.

Sutton, M. (2006). X-ray intensity fluctuation spectroscopy. In F. Hippert, E. Geissler, J. L. Hodeau, E. Lelièvre-Berna, & J.-R. Regnard (Eds.), *Neutron and x-ray spectroscopy* (pp. 297–318). Dordrecht: Springer.

Sutton, M. (2008). A review of x-ray intensity fluctuation spectroscopy. *Comptes Rendus Physique*, *9*(5–6), 657–667.

Wick, G. (1950). The evaluation of the collision matrix. *Physical Review*, *80*(2), 268–272.

Williams, G., & Watts, D. C. (1970). Non-symmetrical dielectric relaxation behaviour arising from a simple empirical decay function. *Transactions of the Faraday Society*, *66*, 80.

Chapter 3
Experimental

An important step in the quest for gaining new insight into glassy dynamics is the experimental realisation. We will first learn about the challenges connected to the preparation of the samples. Then we will see how a stable sample environment can be created. Finally, we will have a closer look at the principles of synchrotrons and how the actual experiments are set up in this context.

3.1 Preparing Glass Samples for Coherent Experiments

A range of lead silicate glasses and alkali borate glasses have been prepared in the course of this thesis. The particular glasses and their compositions are described in Chaps. 5 and 6. Sample preparation poses certain challenges with respect to the material properties in the context of coherent measurements. We will take a look at the approach used to produce suitable glass samples and how these samples can be shaped in a way that allows for coherent scattering.

3.1.1 Glass Melting

The glass batches were formed from chemically pure materials in powder form. The batches were finely mixed and melted in alumina crucibles. For the creation of bulk glass from powder it turned out to be essential to mix the components not only before melting but also during the melting process. Thus a small furnace has been developed with the capability for direct access to the melt by an open top side (see Fig. 3.2). A homogeneous powder blend was reached by mixing all components in a mortar before melting and constantly stirring during the melting process.

A multitude of nomenclatures for describing glass compositions exist and there is no established standard among them (Shelby 2005). In this thesis, the stoichiometric style $(A)_x(B)_{1-x}$ will be used to describe the composition of a glass, where the

M. Ross, *Atomic Diffusion in Glasses Studied with Coherent X-Rays*,
Springer Theses, DOI 10.1007/978-3-319-28646-4_3

composition contains x mole% of A and $(1 - x)$ mole% of B. One should note that although it may look like the mixture consists of the basic building blocks A and B, the structure does not necessarily have to be arranged in that way.

The batches were melted at temperatures ranging between 1123 K for $(PbO)_{60}(SiO_2)_{40}$ and 1273 K for $(PbO)_{30}(SiO_2)_{70}$ and alkali borate glasses. The stirring during melting was especially important for the alkali borate glasses, as the alkali mixing components were blended in as carbonates, with CO_2 emission and bubble formation during the melting process. The melt was typically left for an hour while covering the furnace top with a ceramic lid. Occasional stirring removed bubbles from the melt.

Glass batches of 5–20 g were created. The melts were subsequently quenched to room temperature. In case of the rubidium borate glasses (see Sect. 6.2.2), for each composition two different cooling protocols were used and thus chemically identical samples with different cooling rates were created. For that, half of each fast-cooled batch was remelted in the tube furnace, see below.

The solid specimens were annealed in a tube furnace from about 50 K below glass transition temperature to room temperature with a temperature decrease of about 10 K per hour in order to remove stress. The sample compositions were analysed by Energy-Dispersive X-ray spectroscopy (EDX) showing good agreement with the nominal composition.

Tube Furnace

Slowly cooling from the melt to room temperature requires a programmed control over the temperature. To prepare slowly-cooled samples, an electrically heated tube furnace was used. Pre-melted batches were remelted and then cooled down with a temperature protocol similar to that shown in Fig. 3.1. As can be seen from the right plot, due to the heat capacity of the furnace, the real temperature decay is not as steep as set in the program. However, for all glasses considered in this thesis, the temperature decrease is fast enough to ensure vitrification.

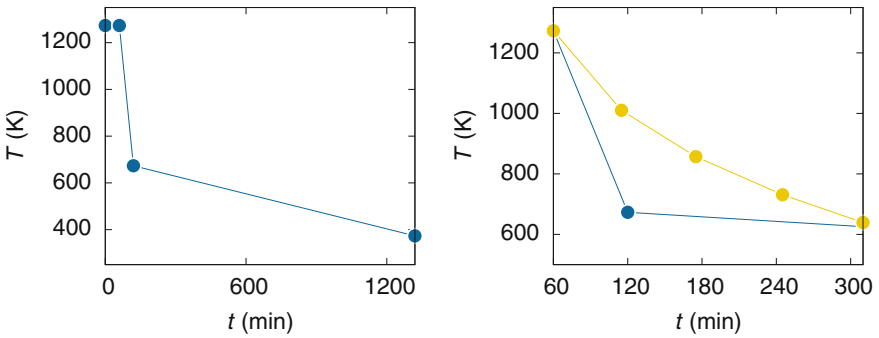

Fig. 3.1 Tube furnace temperature protocol for slowly cooling down the samples from the melt. The *blue curve* shows the set temperature. *Left* Entire cooling protocol. *Right* Zoom on the phase of fastest cooling down. The *yellow curve* shows the actual sample temperature which deviates from the furnace setpoints due to the heat capacity of the furnace

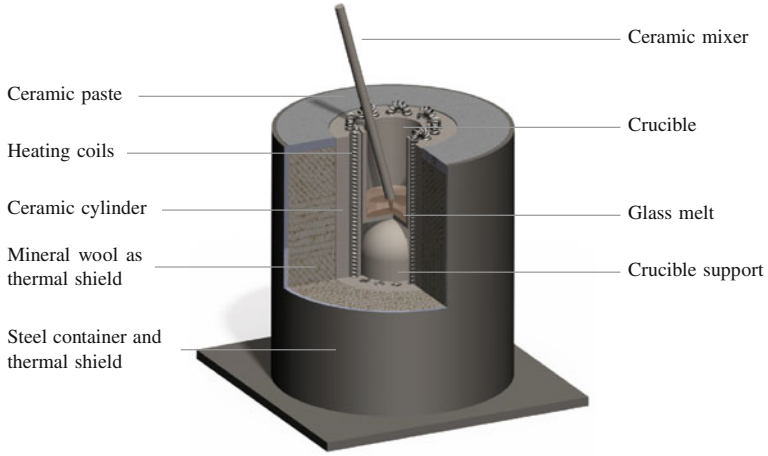

Fig. 3.2 Cross-section CAD view of the constructed stir furnace and its components

Stir Furnace

When creating glass batches from powder, the homogeneity of the melt is often only reached when stirring during melting. For that, a stir furnace was constructed. A sketch is shown in Fig. 3.2. The heating coils are made of 8 m *Kanthal A* steel wires (stable in air up to about 1600 K) with 1 mm diameter and have a total resistivity of about 15 Ω. The furnace design allows to accommodate an alumina oxide crucible with a diameter of 35 mm and a height of 50 mm, see Figs. 3.2 and A.5.

The mixed powder is melted in the ceramic crucible and stirred with a ceramic mixer. The crucible resides on the support such that the lower part of the crucible is in a region of homogeneous temperature. The heating coils are kept in place by a ceramic cylinder with slotted drill holes, allowing direct radiative heating of the crucible. In order to keep as much of the heat as possible inside of the furnace, a thick layer of mineral wool surrounds this cylinder. The mineral wool is covered by ceramic paste for protection and stability. The whole furnace is enclosed by a metallic container, also serving as thermal shield. Electric power supply and temperature can be regulated with a thyristor unit. For temperature measurement, a thermocouple can be inserted into the furnace from the top. After obtaining a homogeneous bubble-free melt, the crucible is removed from the furnace and the melt is poured onto a massive brass block.

3.1.2 Creating Thin But Stable Samples: Dimpling Grinder

Preparation of brittle samples poses a challenge for experiments in transmission geometry. The scattering intensity has a maximum at a certain sample thickness (the

optimal scattering length, see Sect. 2.1.2). The coherently illuminated volume should be minimal while still yielding a reasonable amount of scattering intensity. As a rule of thumb, the thickness of the sample should be below the optimal scattering length if that is achievable (see Sect. 2.1.3). As the glasses under study are very brittle at their optimal scattering thickness (mostly in the range of a few tens of μm) and the width of the beam is only a few μm, it is desirable to prepare the sample in such a way that only a small part of the sample actually is at this thickness, thus retaining the stability of thicker samples. A very convenient way to achieve this sample geometry is the usage of a dimpling grinder.

The dimpling grinder is based on simple mechanical abrasion. The sample is glued on a turning table, rotating in the horizontal plane. Perpendicular to this plane, the grinding wheel rotates and slowly takes off material from the sample. Both movements combined impose an inverse spherical profile on the sample. By that, the desired amount of material is removed in the rotational midpoint while outer parts stay untouched. The radius of the affected region R_d can be calculated as visualised in Fig. 3.3:

$$\begin{aligned} R_\mathrm{w}^2 &= (R_\mathrm{w} - h_\mathrm{d})^2 + R_\mathrm{d}^2 \\ h_\mathrm{d} &\approx \frac{R_\mathrm{d}^2}{2R_\mathrm{w}} \end{aligned} \tag{3.1}$$

Here, R_w is the grinding wheel radius and h_d the dimpling height. With $R_\mathrm{w} = 7.5\,\mathrm{mm}$ and a typical dimpling height of $h_\mathrm{d} = 0.2\,\mathrm{mm}$, an area with a maximum radius of $R_\mathrm{d} \approx 1.7\,\mathrm{mm}$ is affected on the surface.

To assess the deviation from a plane-parallel sample in the X-ray beam, the maximal difference between the sample thickness at the midpoint and at the outermost point of the sample in the beam can be calculated according to Eq. (3.1). Even for large beam sizes of $R_\mathrm{d} \approx 5\,\mu\mathrm{m}$ the height difference would be in the range of 2 nm, which is negligible compared to the sample thickness of typically more than 5 μm.

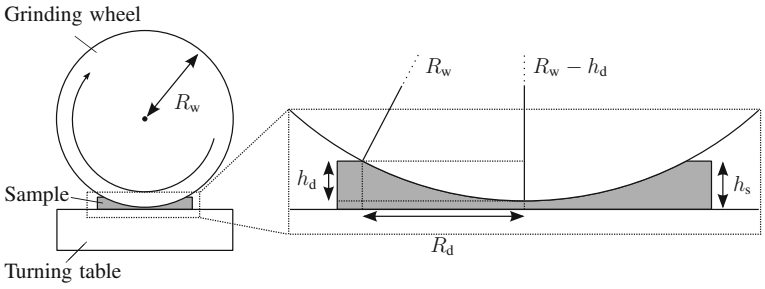

Fig. 3.3 Schematic of the principle of the dimpling grinder. The grinding wheel is shown together with a sample on the *left*, a zoom on the sample is shown on the *right*. For detailed photos see Fig. A.4

To enhance the abrasion speed, diamond paste is used in combination with a cutting fluid. Typical dimpling rates tend to be in the range of 0.5–3 µm per minute, leading to a total dimpling duration on the order of 1–10 h.

The dimpling grinder *Fischione Instruments Model 2000* was used to prepare the samples. After dimpling, the samples have to be removed from the turning table, which is normally done with acetone. In the case of water sensitive samples, instead of glue a wax is used which can be removed by slightly warming and using a water free solvent.

The samples were prepared with a thickness of 15–20 µm in the case of lead silicates glasses and 20–50 µm in the case of alkali borate glasses. The profile of the dimpled samples can be studied by measuring the transmitted intensity of an X-ray beam with a diameter of 0.5 mm normal to the base plane of the sample. According to the Beer-Lambert law, the transmitted intensity is proportional to the thickness d of the sample

$$I = I_0 \mathrm{e}^{-\mu d}, \tag{3.2}$$

with material dependent attenuation coefficient µ and incident intensity I_0. Reformulating to

$$d = -\frac{\ln I}{\mu} + \frac{\ln I_0}{\mu} \tag{3.3}$$

shows that the thickness is proportional to the negative logarithm of the measured intensity plus a constant value. The measurement of a lead silicate glass sample profile is shown in Fig. 3.4. The raster image has been obtained by measuring the intensity transmission of the sample with a *Bruker AXS Nanostar* Small-Angle X-ray Scattering (SAXS) device.

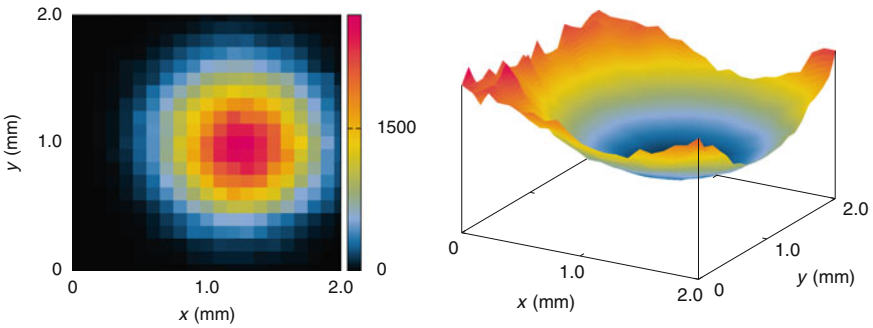

Fig. 3.4 Depth profile measurement of a lead glass sample prepared with the dimpling grinder. *Left* Colour map of X-ray transmission intensities in ADU, measured for a raster of sample positions. *Right* Three-dimensional representation with negative logarithm of intensity as third dimension and interpolated values

3.2 Creating a Stable Sample Environment for Atomic-Resolution Measurements

In order to carry out experiments at a synchrotron beamline, the sample should stay in a very stable position at the centre of the beam and at a well-defined constant temperature. By changing the temperature of the sample, the diffusion rate can be regulated. As aXPCS is currently limited to a certain range of diffusion speeds, the according temperature window has to be chosen to be able to measure the diffusion. A vacuum sample cell has been constructed for measurements in the range of 150–1300 K, while for measurements in the low temperature regime of about 20 K a helium cryostat is required.

3.2.1 Vacuum Sample Cell

The vacuum cell can be operated in two different modes. The main mode is the heating mode, where stable temperatures between 300–1300 K can be reached by a furnace built-in to the sample cell. The second mode is an extension to low temperatures down to about 150 K. In that setup, the furnace is switched off and the regular sample holder is replaced by a cold-finger sample holder. The temperature is then entirely controlled through the cold finger.

Heating Mode

In heating mode, the sample is mounted in a sample holder which is placed at the centre of a resistively heated furnace. The heating wires are made of about 2.5 m high-purity tantalum with 0.25 mm diameter. This metal offers the advantageous properties of a high melting point while having good ductility, which makes the wires more durable. The wires are wrapped around a ceramic cylinder which defines the spacing of the wires. This cylinder is placed inside a tantalum cage and connected to the power supply through a vacuum feedthrough at a dedicated flange. To minimise heat loss, the inner part of the furnace is covered by a metallic thermal shield and has only openings for the sample holder, the electric wiring and the beam. The entry holes for the beam can be kept small, while downstream of the sample, the openings widen up to allow for the scattered radiation to exit at angles of 0° to up to about 35°. As the direct beam can pass through the furnace, scanning of the sample is possible without having to remove parts of the sample cell. At regular measurements, a lead beam-stop is attached directly to the exit window to minimise scattered radiation of the direct beam downstream of the sample. The furnace is attached to the blind flange of the entry window. To minimise background intensity from X-ray scattering in air and to avoid furnace oxidation and heat losses, the sample cell is vacuumised by a turbomolecular pump.

The outer casing of the cell and the cell stage are symmetric with respect to the plane which is perpendicular to the beam direction and goes through the middle

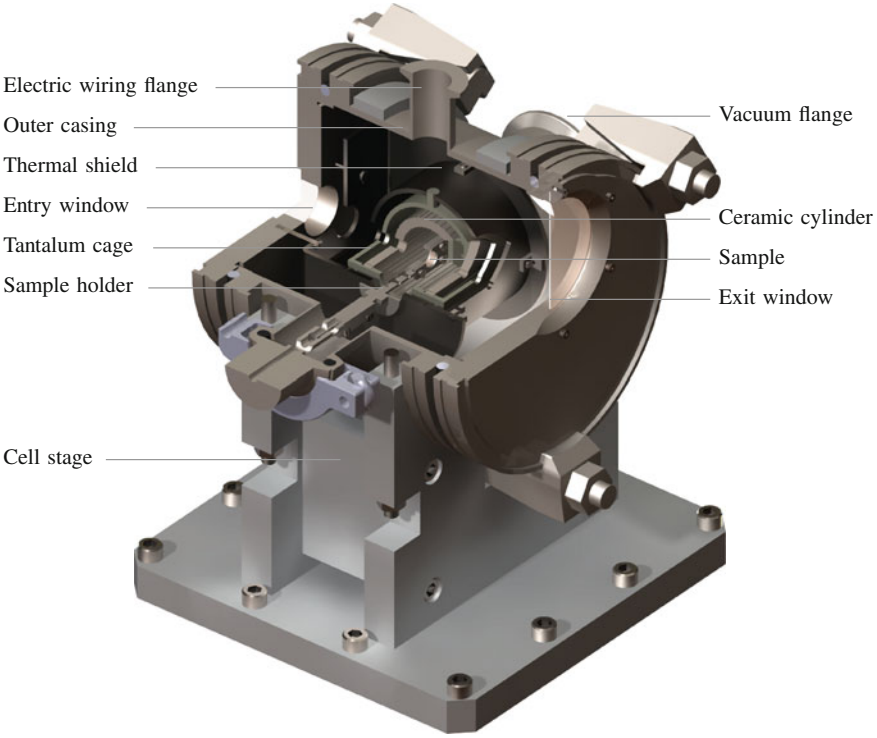

Fig. 3.5 Cross-section CAD view of the constructed experimental cell with furnace

of the casing. This allows for two different mounting options of the sample cell which are necessary due to different experimental setups at the synchrotrons used (see Sect. 3.3). The first option is standing in upright position (as shown in Fig. 3.5), which is the mode used at the ESRF. In the second arrangement, the detector is still movable in the angular region above the beam, thus the openings of the cell need to be arranged identically to the first setup. However, the cell now has to be mounted in a hanging setup as provided by the PETRA III. This can be achieved by assembling all components in the exact way as before but with the outer casing (and cell stage with clamps) rotated by 180° around the sample-holder axis (see Fig. 3.6). The only other change necessary to account for the different setups is the usage of electrical wiring of slightly different length.

The beam enters and exits the sample cell through Kapton windows. This polymeric material is mechanically very stable, temperature-resistant and has a high transmittance for X-rays. Kapton is also relatively resistant to radiation damage. However, in the experiments carried out for this thesis, it has been found that after several hours of measurement, degradation sets in due to beam exposure. As degradation leads to a decreased contrast, the furnace position relative to the direct beam should be changed by few microns from time to time to omit this degradation process.

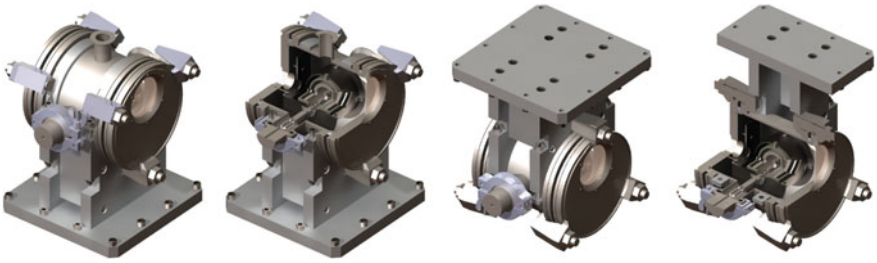

Fig. 3.6 Comparison of upright standing (used at the ESRF) and overhead hanging (used at the PETRA III) configuration, each in full and cross-section CAD view

The sample is fixed by the sample clip (see Fig. 3.7). The sample holder is constructed such that the middle of the opening of the sample clip (and thus the centre of the sample) is exactly in the middle of the beam. An adjustable clamp allows for small corrections of the position of the clip normal to the beam in the horizontal plane. An *Inconel*-sheathed thermocouple is attached close to the sample to measure the temperature inside the furnace, which should be equivalent to the sample temperature in thermal equilibrium. A thermal shield helps reducing radiation losses through the sample-holder opening of the furnace. The thermocouple is connected to the external temperature controller *Eurotherm 2416*, which in turn regulates the power supply of the heating wires to achieve a stable temperature.

The difference of the actual sample temperature to the measured nominal temperature can have a systematic bias. However, it should be less than 10 K, as has been verified by a second thermocouple in place of the sample and by an infrared thermometer. More important is the stability of the sample temperature which is not influenced by a systematic bias. The thermal latency of the sample cell leads to a delayed change in temperature after changing the set value. Changing the set temperature by a few tens of degrees leads to about 2 min for the sample cell to reach the new value. After about 10 min the sample cell reaches the stabilised temperature.

The sample holder is not directly attached to the furnace but is inserted sideways into the vacuum cell, which has two main advantages. Firstly, the sample holder is not influenced by movements of the furnace due to thermal expansion. This is critical

Fig. 3.7 Full and cross-section CAD view of the sample holder for high-temperature measurements

because the stability of the sample position is of crucial importance when trying to resolve atomic movements. Secondly, the sample can be easily removed and a new sample can be put into position without having to remove the sample cell or the furnace, which significantly speeds up the process of measuring multiple samples. Also, the setup of the sample cell can be switched from heating mode to cooling mode by just exchanging the sample holders.

Cooling Mode

In order to expand the temperature range below room temperature, a cold finger has been designed, replacing the conventional sample holder. Its inner metal parts are made of oxygen-free high thermal conductivity copper. The base part can be cooled by water running through a bored cooling pipe. Additionally, a Peltier element ($P_{max} \approx 20\,W$, $\Delta T_{max} \approx 75\,K$) is placed between the base part and the upper part of sample holder, allowing to further decrease the sample temperatures. In order to avoid heat flow through other parts than the Peltier element, both copper parts are separated by the Peltier element and pressed together by plastics with low thermal conductivity. Slot holes allow for small corrections of the position of the upper part normal to the beam in the horizontal plane. The sample clip is mounted on the upper part of the sample holder and keeps the sample at a fixed position. A thermocouple measures the temperature of the upper part of the sample holder, which should be equal to the sample temperature in thermal equilibrium. The wiring for the Peltier element and the thermocouple are connected to external control units through a vacuum-tight feedthrough. For attaching the sample holder to the outer casing of the cell, a gasket is clamped between the sample-holder flange and the clamping flange such that the copper body and the gasket form a vacuum-tight unit.

With this setup, cooling to some fifty degrees below room temperature is possible. Another operating mode is possible by using cold nitrogen instead of water for cooling the main part and using the Peltier element for stabilising the temperature by heating. In that mode, temperatures of 150 K have been reached (Fig. 3.8).

Fig. 3.8 Full and cross-section CAD view of the cold finger for low-temperature measurements

3.2.2 Helium Cryostat

In order to slow down diffusion even further, which is especially important for studying fast ionic conductors, much lower temperatures are required. For this, a cryostat was utilised (see Fig. A.6). It enables temperatures in the range of about 15–150 K. Helium from a cryogenic tank was used to cool the cryostat. Pumping was applied to increase the helium flow from the tank. The lowest stable temperature which could be reached with this setup within reasonable cooling time was at 20 K. The temperature was controlled by a *Lake Shore Model 325* unit.

3.3 Obtaining Scattering Data for Atomic-Diffusion Studies

In order to study atomic diffusion with aXPCS, intensity patterns of coherently scattered X-rays need to be obtained. We will first examine how this kind of radiation is created and then look at the actual synchrotron experiments performed. Finally we will see how supplementary details can be obtained with conventional X-ray scattering.

3.3.1 Generating Coherent X-Rays

The basic principle of a synchrotron is that a charged particle is accelerated in a closed loop. This acceleration is achieved by time-varying electric and magnetic fields synchronised to the accelerated particles, therefore the name.

The basic part of a synchrotron is a (close to) circular vacuumised tube equipped with bending and focusing magnets and accelerating cavities. Particles gain momentum inside the accelerating parts of the vacuum tube such that they reach velocities close to the speed of light.

While moving along this tube, the charged particles emit so-called synchrotron radiation in a narrow cone with an emission angle $\theta \propto 1/\gamma$ (with Lorentz factor γ) along the velocity direction (Bilderback et al. 2005). As they move at relativistic speed, the direction of the emitted radiation in the laboratory system is almost entirely tangential to the path of the particle. The particles lose energy to this radiation but regain it from the accelerating field.

The rate of energy loss of a charged particle due to synchrotron radiation is proportional to the square of the Lorentz factor γ, which means that a heavy particle like a proton needs a much higher energy (γmc^2) than a light particle like an electron to produce comparable synchrotron radiation. Due to this fundamental difference, two main types of synchrotrons exist. In the first type, heavy particles are accelerated and used for heavy-particle collision, where only a negligible amount of energy is lost as synchrotron radiation, while in the second type, light particles are accelerated

to produce a significant amount of synchrotron radiation. This second type is also called *synchrotron light source*. Referring to synchrotrons implies the second type in this thesis.

In principle, either electrons or positrons can be used as accelerated particle in synchrotron light sources (with only minor changes like opposite direction of motion or magnetic field). While using positrons has certain advantages like avoiding the effects of positive ion-clouds which can occur even in the ultra-high vacuum using an electron beam (Wiedemann 2003), it is much easier to create electron beams, thus electrons are predominantly used in synchrotron facilities. We will only consider electrons as accelerated particles in this thesis, but all principles apply to positrons as well.

Acceleration of electrons is achieved by electric fields. Usage of static electric fields is problematic due to technical reasons (the necessary field strengths would lead to sparkovers, breakdowns and arcs). A solution to this problem is using an alternating electric field instead of a static one. Technically, this is realised by using Radio Frequency (RF) cavities, typically powered by klystrons.

The electrons in the synchrotron ring are not homogeneously distributed but have a bunched structure. This effect is due to the time structure of the accelerating RF field. It can be easily understood in a simplified way by looking at an electron travelling at a speed of $v \approx c$ along a synchrotron with circumference U. The electron loses kinetic energy as it emits synchrotron radiation. This energy is replenished by the RF cavities, which provide acceleration by an oscillating field. Let us look at one specific electron and one specific RF cavity providing oscillations exactly in phase to the electron cycling frequency ν, so each time the electron travels one circumference of the synchrotron, it gets accelerated once in the cavity. If the frequency of the RF field f is increased, it needs to be an integer multiple of the cycling frequency of the electron, because otherwise the electron would get quickly out of phase and be lost to the system (Willmott 2011). If the RF field would have the same frequency as the cycling electron, only one bunch of electrons (with a length smaller than the cavity length) would be possible. Increasing the frequency of the RF cavities N-fold thus leads to N potential bunches. These potential bunches are typically called buckets if they contain no electrons. So the number of buckets can be calculated by

$$N = \frac{f}{\nu} = \frac{fU}{c}. \tag{3.4}$$

For a synchrotron like the PETRA III with a cavity frequency of $f \approx 500\,\text{MHz}$ and a circumference of $U \approx 2304\,\text{m}$ this leads to a bucket number of $N = 3840$. In actual synchrotron operation, not all buckets need to be filled and different operating modes exist, e.g. to enable a certain time resolution. The time between two bunches, called bunch separation, is thus the inverse of f if all buckets are filled and a multiple of the inverse of f if only a fraction of the buckets are filled. For the operating modes of 960 and 40 bunches at the PETRA III, this leads to bunch separations of 8 ns and 192 ns (the ESRF operates with bunch separations in the range of 2.82–2816 ns). While for certain experiments this time structure can be crucial, in the aXPCS experiments

conducted in the context of this thesis, processes took place on time scales on the order of seconds, thus the radiation can be a seen as quasi-continuous.

The synchrotron radiation considered so far is purely produced by forcing electrons at relativistic speeds on a circular path. Additionally in modern synchrotrons, so-called insertion devices which further enhance the emitted radiation are utilised. An important quantity which can be used to characterise the X-ray beam created in a synchrotron and particularly by insertion devices is the brilliance, which is closely connected to the brightness. Typically, the brightness of a source is defined as number of photons emitted by the source into a unit solid angle per unit source area. Using a pinhole in the dimensions of the transversal coherence lengths to create an entirely transversally coherent beam, the brightness could be used as a measure to assess how many transversally coherent photons can be provided by the source. However, for methods like aXPCS, the coherence volume and thus also the longitudinal coherence length is important (see Sect. 2.1.3). As the synchrotron radiation is typically monochromatised by a crystal monochromator with $\Delta E/E \approx 10^{-4}$, an often more useful quantity is the brilliance, also called spectral brightness and defined analogously to the brightness, but per energy bandwidth of 10^{-3}:

$$b = \frac{\text{photons/s}}{(\text{mm}^2 \text{ source area}) \cdot \text{mrad}^2 \cdot 0.1\,\% \text{ bandwidth}} \tag{3.5}$$

The brightness of a synchrotron can be drastically increased by using the aforementioned insertion devices. These components of third generation synchrotrons force electrons on a sinusoidal path transversal to their average cyclic path. This approach is used as it has been found that the transverse acceleration leads to much higher radiation power than longitudinal acceleration (García-Gutiérrez and Rueda 2009). The transverse acceleration is caused by a series of dipole magnets with alternating field direction.

There are two types of insertion devices which in principle only differ by the amplitude which they impose upon the electron motion but as a result emit radiation with very different properties. The first type are the so-called wigglers. They can be thought of as a series of bending magnets and have similar characteristics to the radiation created by the storage ring itself. In a good approximation, their intensity is $2N$-fold that of the storage ring, where N is the number of alternating magnetic periods of the wiggler. The second type are the so-called undulators. They are constructed similar to wigglers, but with a smaller periodicity of dipole magnets and weaker magnetic fields. The amplitude of the sinusoidal path imposed on passing electrons is much smaller than in a wiggler and the radiation cones emitted by the accelerated electrons now overlap. For certain wavelengths, this overlap leads to constructive interference and the radiation has a much narrower energy spectrum. This results in radiation of a significantly higher brilliance compared to wigglers for certain wavelengths (García-Gutiérrez and Rueda 2009). The wavelength of the radiation produced in an undulator can be adjusted by changing the magnet separation and thus the magnetic field strength. For certain applications, higher harmonics are

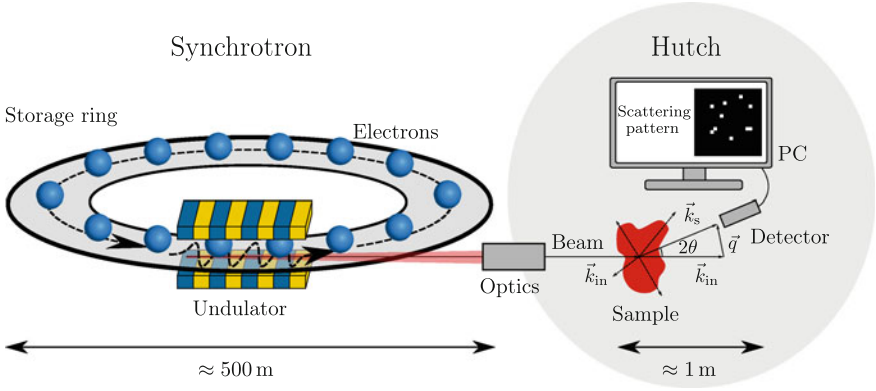

Fig. 3.9 Experimental setup at a synchrotron: Charged particles (*typically electrons*) are accelerated around a closed loop and in insertion devices (*typically undulators*) and emit synchrotron radiation tangential to the loop. This radiation is further enhanced by the beamline optics and usable for measurements in the experimental hutch, where sample and detector are set up

used for which also constructive interference occurs, although with a much lower photon count.

Further downstream of each of the insertion devices, experimental halls called beamline are installed. A beamline typically consists of a front end, an optics hutch and an experimental hutch (Willmott 2011). The front end monitors the position of the photon beam, filters and blocks the radiation if necessary and isolates the beamline vacuum from the storage-ring vacuum. The optics hutch provides monochromatisation and refocusing of the beam. For that, a monochromator and X-ray mirrors are utilised. The experimental hutch provides the facilities for the end users to utilise the radiation for their experiments. As the optics and the setups of each beamline can differ, each of the beamlines has specific scientific target applications.

The scattered radiation is collected by a CCD detector. The preferred size of the scattering speckle patterns should be on the same order as or slightly smaller than the size of the detector pixels. Typically, a distance between 0.5–1 m has been chosen to achieve this speckle size to pixel size ratio (see Fig. A.8) (Figs. 3.9 and 3.10).

3.3.2 Conducting Synchrotron Experiments

The experimental data for the diffusion studies of this thesis have been obtained at six beamtimes, each lasting for six days. The aXPCS measurements were performed at the synchrotrons ESRF and PETRA III (see Table 3.1). Both are third generation synchrotrons and belong to the most advanced sources for coherent X-rays in the world.

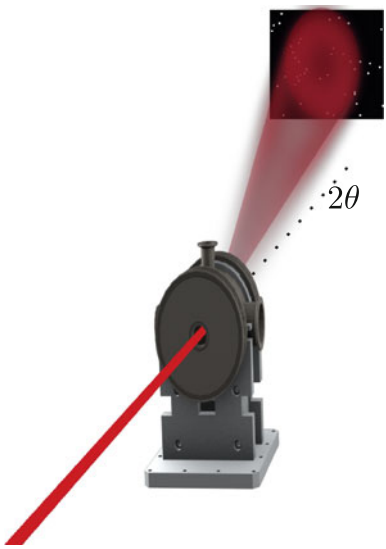

Fig. 3.10 Visualisation of the scattering of synchrotron radiation in the sample cell (see Sect. 3.2.1) and detection of the scattering pattern at angle 2θ with a CCD detector in the experimental hutch

The aXPCS experiments for lead silicate glass (see Chap. 5) were performed at the beamline P10 of the synchrotron PETRA III using a coherent setup with 7.05 keV photons for the $(PbO)_{30}(SiO_2)_{70}$ and 8 keV photons for the $(PbO)_{60}(SiO_2)_{40}$ sample using the heating mode of the vacuum sample cell.

Measurements on alkali borate glasses were done at synchrotron PETRA III using a cryostat as well as at beamline ID10 of the ESRF using the cooling mode of the vacuum sample cell.

All measurements were performed with the sample environment at a pressure of about 10^{-6} mbar. The temperature in the measurements of elevated temperatures was stabilised by a Proportional-Integral-Derivative (PID) controller within a range of 0.1 K. The intensity patterns were recorded for several scattering vectors and the intensity autocorrelation functions were calculated (see Fig. 4.6).

Table 3.1 List of experiments conducted at coherence beamlines of synchrotron facilities in the context of this thesis and samples measured (for details on the samples see Chaps. 5 and 6)

Year	Synchrotron	Energy (keV)	Detector	Sample
2011	PETRA III	7.00 and 8.00	Pixis	Trials with lead silicate glasses
2011	ESRF	8.00	Andor	Trials with lead silicate glasses
2012	PETRA III	7.05	Pixis	$(PbO)_{30}(SiO_2)_{70}$
2013	PETRA III	8.00	Pixis	$(PbO)_{60}(SiO_2)_{40}$
2013	ESRF	8.10	Andor	Alkali borate glasses
2014	PETRA III	8.00	Pixis	Alkali borate glasses

The stability of the sample as well as the mechanical stability of the setup was checked by calculating the two-time autocorrelation function for each measurement (see Fig. 4.7). For systems which are in equilibrium, the two-time autocorrelation function depends solely on $\Delta t = t_2 - t_1$. For the few measurements where instabilities of the setup occurred, these have been excluded.

Measurements for one detector position were repeated multiple times and only if the resulting correlation function was stable the measurement was considered as being in quasi-equilibrium. The sample relaxation took usually several hours at one temperature. As the equilibration procedure must be repeated at each new temperature, measurements of the activation energy have not been conducted due to the limited beamtime on synchrotrons.

ESRF

Experiments were performed at beamline ID10 at the ESRF. A photon energy of 8 keV was used and the X-ray beam was focused with a Be compound refractive lens system and monochromatised by a Si(111) crystal channel cut monochromator (energy resolution $\Delta E/E \approx 10^{-4}$). As can be seen from Eq. (2.16), this leads to a longitudinal coherence length on the order of the sample thickness. The beam was typically cut to dimensions on the order of $10 \times 10\,\mu\text{m}^2$ with movable tungsten slits located upstream the sample. The flight tube was placed directly after the sample cell, leaving only a small path of few centimetres in air for the scattered rays to pass downstream the furnace before entering the flight tube. The samples were measured in transmission geometry, with an angular 2θ range of about 2°–35°.

The standard setup at the ESRF is shown in the upper part of Fig. 3.11. As the z-stage is set in a middle position for a flight tube and detector tilt angle of $\gamma_1 = 0$, the potential of the stage is not fully utilised when going to high γ_1 angles. In this setup, the accessible γ_1 value is limited to about 15°. In order to achieve higher angles, an adaptor plate has been purpose-built. Using the adaptor and additional distance plates, the z-stage could be raised by about 60 mm and thus also γ_1 angles of more than 20° were possible. Due to the isotropic nature of glasses, the scattering only depends on 2θ and is independent of the azimuthal angle. Any combination of the angles δ and γ, as depicted in Figs. 3.11 and 3.12, which results in the same angle 2θ leads to equivalent scattering patterns. Thus the base goniometer angle δ can be utilised to further increase the 2θ limit. Utilising just the δ angle alone to reach the desired 2θ angles was not possible due to constructive limits of the sample cell. Using the adaptor plate setup, 2θ angles of more than 35° have been reached.

The scattered radiation was detected by a direct-illumination CCD camera (*Andor Ikon*, 1024 × 1024 pixels, $13 \times 13\,\mu\text{m}^2$ pixel size). The camera was put about 0.5m from the sample to have an acceptable contrast (see Sect. 2.1.3).

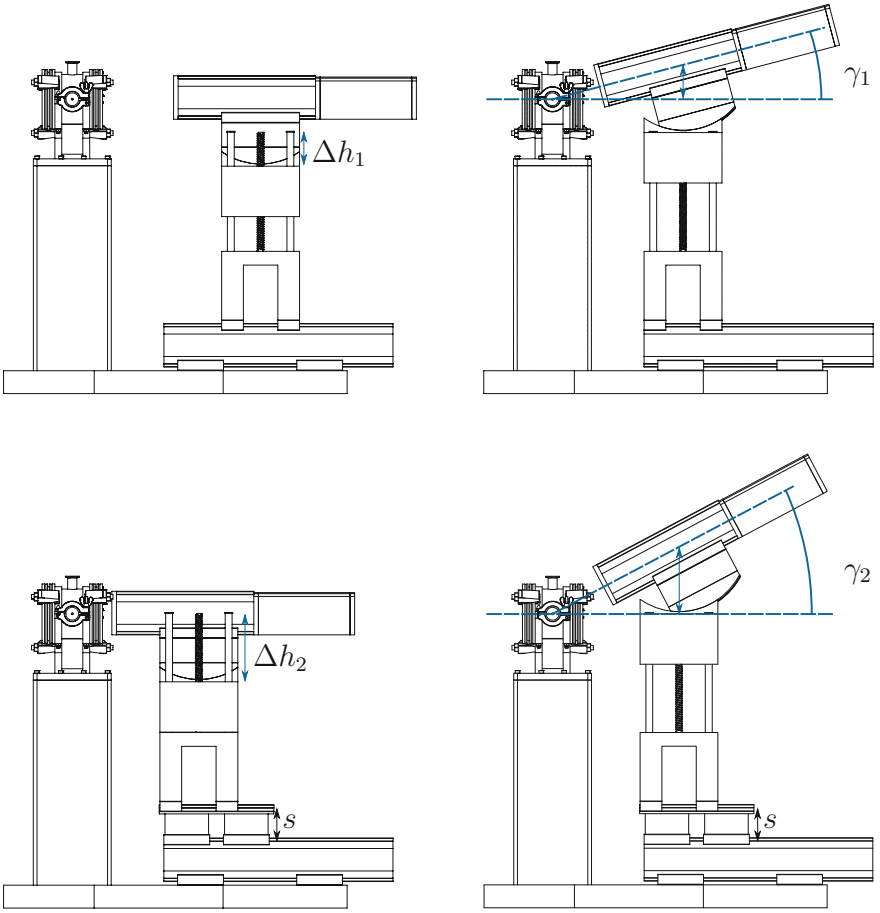

Fig. 3.11 Additional flight tube and detector angle reachable by adding adaptor and distance plates. *Upper part* Standard setup with straight (*left*) and maximum tilted detector angle γ_1 (*right*). *Lower part* Modified setup with straight (*left*) and maximum tilted detector angle γ_2 (*right*). The additional separation s leads to a higher elevation $\Delta h_2 = \Delta h_1 + s$ and thus to a larger angle γ_2. For more details on the setup see Fig. 3.12

PETRA III

PETRA III is a new high-brilliance third generation synchrotron located at the facility DESY in Hamburg, Germany. Beamline P10 is one of 14 undulator beamlines installed at the PETRA III and offers a setup specially designed for coherent applications. Micro-focusing is achieved by compound refractive lenses, which leads to beam sizes at the sample of about $10 \times 10\,\mu m^2$. The beam is monochromatised by a high heat-load Si(111) crystal channelcut monochromator. A pair of horizontally

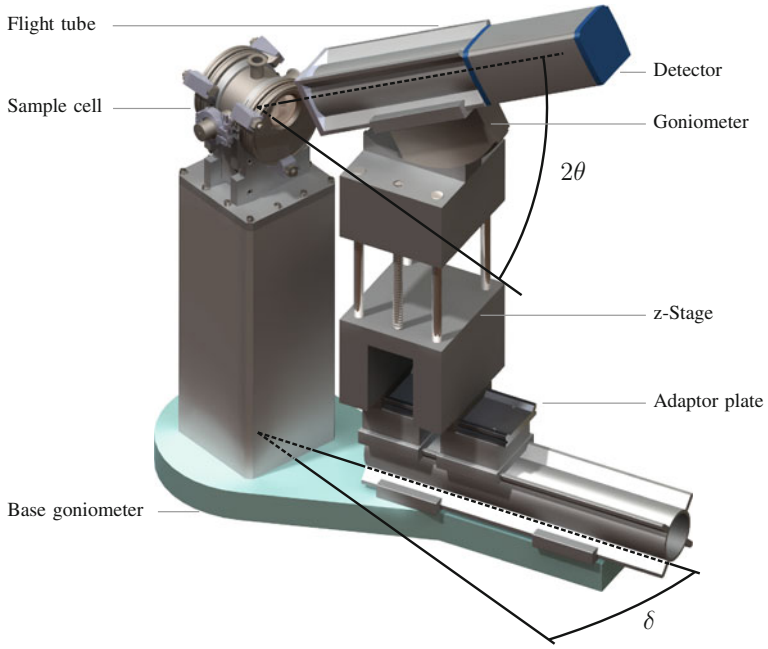

Fig. 3.12 Scattering angle 2θ and base goniometer angle δ of the ESRF setup with adaptor plate, visualised in CAD view

reflecting flat ($R > 100$ km) mirrors suppress the higher harmonics. Typical radiation energies are in the medium-hard X-ray regime of 5–25 keV.

The beamline setup at the PETRA III is different in that the sample cell has to be mounted overhead hanging from a stage goniometer. This is due to the detector and the flight tube being mounted on a movable arm, installed on a goniometer directly below the sample cell. This allows for a wide range of 2θ angles (see Fig. A.8), with the detector being moved along a spherical shell.

The scattered radiation was detected by a direct-illumination CCD camera (*Princeton Instruments Pixis*, 1340 × 1300 pixels, $20 \times 20\,\mu m^2$ pixel size). The camera was put about 0.7 m from the sample to gain sufficient intensity while having an acceptable contrast (see Sect. 2.1.3).

3.3.3 Gaining Complementary X-Ray Scattering Information

The short-range order intensity can play an important role when interpreting aXPCS data (see Sect. 2.4.3). In a first approximation, the azimuthally integrated scattered radiation intensity of glasses can be identified with this short-range order intensity. A detailed view on the scattered intensity can be obtained using a conventional X-ray

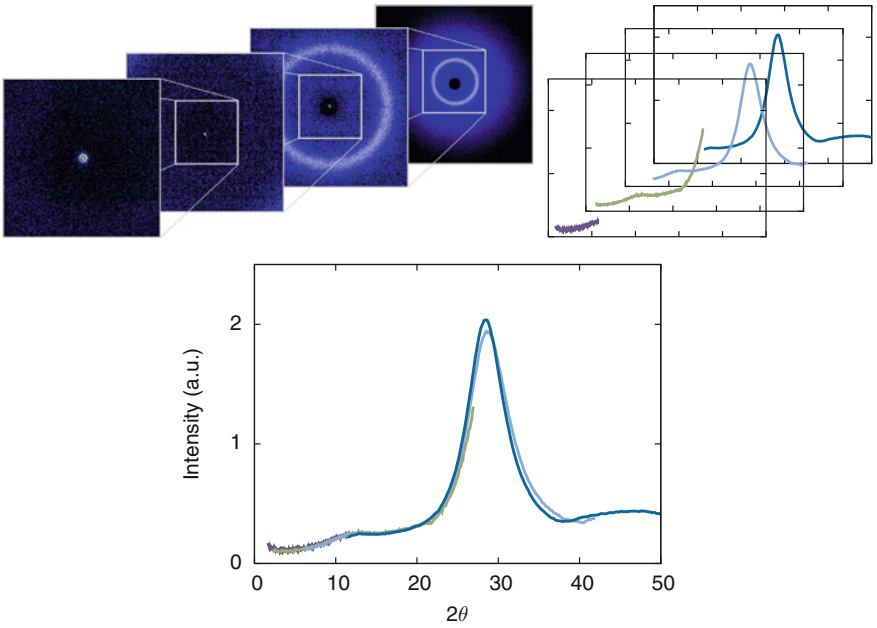

Fig. 3.13 Intensity curves over a wide angular range can be obtained by stitching together measurement values obtained for different sample-to-detector-distances. *Upper left* Intensity patterns at different distances, containing different levels of detail and angular spread. *Upper right* Integrated intensities over azimuthal angle for each intensity pattern. *Lower part* Intensities superimposed to form a single curve

source at different sample to detector distances, stitching together the obtained 2θ ranges (see Fig. 3.13). For these measurements, a *Bruker AXS Nanostar* was used.

References

Bilderback, D. H., Elleaume, P., & Weckert, E. (2005). Review of third and next generation synchrotron light sources. *J. Phys. B: At. Mol. Opt. Phys.*, *38*(9), 773–797.

García-Gutiérrez, M. C., & Rueda, D. R. (2009). Bases of synchrotron radiation and light sources. In T. A. Ezquerra, M. C. García-Gutiérrez, A. Nogales, & M. A. Gómez (Eds.), *Applications of synchrotron light to scattering and diffraction in materials and life sciences* (pp. 1–22). Berlin: Springer.

Shelby, J. E. (2005). *Introduction to glass science and technology*. Cambridge: Royal Society of Chemistry.

Wiedemann, H. (2003). *Synchrotron radiation*. Berlin: Springer.

Willmott, P. (2011). *Applications of synchrotron light to scattering and diffraction in materials and life sciences*. New York: Wiley.

Chapter 4
Data Analysis

To gain actual information on atomic dynamics, we need to process the raw scattering information obtained in the experiment. We will first look at how the scattering information can be converted. Then we will learn that considering single-photon events helps to overcome the challenge of particularly low intensities and allows for efficient data processing. Finally we will see how the obtained data can be connected to theoretical models and that data processing can be optimised to provide a direct feedback during the experiment, thus helping to efficiently use the synchrotron beamtimes.

4.1 Converting Scattered X-Rays to Intensity Data

To convert scattered X-rays to computationally usable data, the scattered X-ray photons have to be detected and counted. Techniques such as photographic and image plates suffer from the long post-processing time. In XPCS, as time series of intensity patterns are correlated, it is crucial to be able to measure intensity versus time with comparatively small time lags. Point detectors like photomultiplier tubes, scintillation counters and avalanche photo diodes (Johnson et al. 2008) and area detectors like CCD sensors are able to achieve this task.

While point detectors are very fast, the statistics of XPCS measurements for slower processes can be drastically increased by using 2D single-photon multi-pixel CCD cameras, as the signal to noise ratio is proportional to the square root of the number of measured speckles (Sutton 2008). This is particularly important for aXPCS experiments with low intensities. In synchrotron experiments, most of the 2D detectors used are based on CCD sensors. Newer developments comprise array chip detectors like Maxipix (Ponchut et al. 2011) and Pilatus (Broennimann et al. 2006). While these are promising in their properties of faster readout, they have not been utilised in this thesis due to the larger pixel sizes, which lead to infeasible flight tube sizes for the angles used when aiming for a comparable number of pixels with the same speckle size to pixel size ratio.

M. Ross, *Atomic Diffusion in Glasses Studied with Coherent X-Rays*,
Springer Theses, DOI 10.1007/978-3-319-28646-4_4

Let us look at the principles of a CCD detector and the data cleaning techniques applied to efficiently utilise this device.

4.1.1 Detecting Single Photons

The scattered radiation is detected with a CCD detector. A CCD sensor can be seen as an array of photosensitive capacitors coupled together as a shift register. Each capacitor represents one pixel in the array. A photon hitting the active area of the detector creates a cloud of electric charges. During illumination, each capacitor accumulates these electric charges proportional to the light intensity present at its position. In order to convert this two-dimensional intensity information, the charge levels of the capacitors have to be read out. This is done by a sequential shifting of each charge packet to the next capacitor, dumping and amplifying the charges at the last capacitor in the row after each sequence and storing the voltage as digital information. Until all capacitors are read out in that way, no further illumination of the CCD is advisable (and normally prevented by using a shutter), as the additional intensity would influence the charges of those capacitors which have not been read out yet. This splits the operation of a CCD detector into two steps, which are the exposure phase and the readout phase. In the experiments carried out for this thesis, typical exposure and readout times for one intensity image, also called *frame* (Fig. 4.1), are on the order of 1–10 s and 0.5–2.5 s respectively.

The dimensions of a direct-illumination CCD pixel are on the order of $10 \times 10\,\mu m^2$ to $20 \times 20\,\mu m^2$ and the typical distance between the CCD camera and the sample is about 0.5–1.0 m. In this case the angular spread of the detector is small enough that all pixels of the camera can be used for averaging in order to increase the statistical significance of the weak diffuse signal, representing a single q value. As in the real measurements, the radiation of the X-ray source is only partially coherent and the sample volumes are larger than the longitudinal coherence length, contrast is lost. The contrast is also influenced by the speckle size relative to the pixel size of the detector.

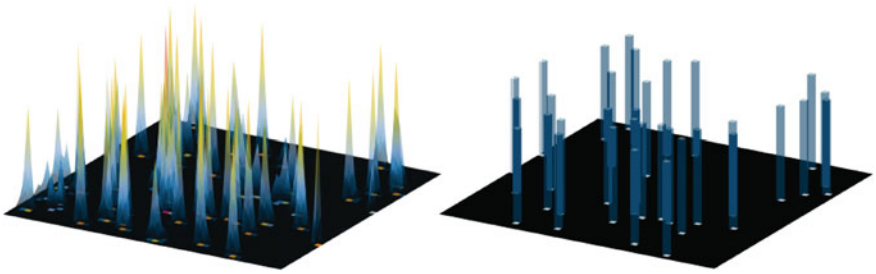

Fig. 4.1 *Left* X-ray intensity pattern zoom on a 50×50 pixels area obtained with a CCD detector. The z-axis represents the intensity in each pixel. *Right* After subtracting the dark current, single photon positions and energies can be identified with a droplet algorithm

The size of a speckle on the detector is determined by the size of the scattering region. Similar to the effect of diffraction at a slit, the speckle size is proportional to the reciprocal value of the illuminated volume and to the distance between the detector and the sample. The preferred size of the speckles is slightly smaller than the size of the detector pixels (Leitner 2012).

4.1.2 Disposing of the Dark Current

Any CCD detector produces an output voltage when active, even without being illuminated. This thermally activated effect is a leakage current (Strauss et al. 1988) due to random creation of electron-hole pairs in the photosensitive region (Willmott 2011). The resulting current is called dark current, which is a normal effect due to the function principle of this detector type. The dark current is time independent, as long as there is no change in the CCD environment (e.g. temperature). In order to analyse the measured data, the apparent dark current intensity has to be subtracted from each frame. There are several possibilities to determine the dark current. The most direct but also more time-consuming option is to measure some frames without illumination and to average over these frames. Another option is to calculate the dark current from the obtained measurement frames. As only few photon events occur per frame, most of the detector is just recording the dark current. Thus one can obtain the dark current by averaging over all frames after removing the photon events. For calculating the mean, the size of the data files can impose restrictions as for

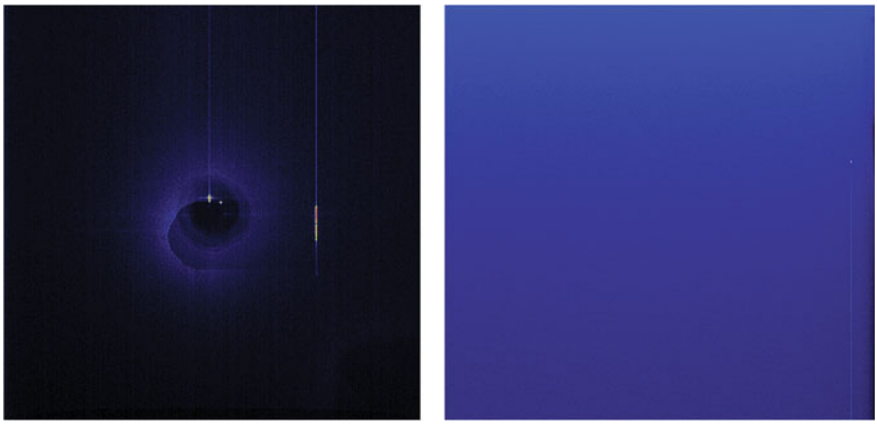

Fig. 4.2 *Left* Dark current image taken with an *Andor Ikon* camera as used at the ESRF. As can be seen, some traces of previous experiments (presumably small-angle scattering with high scattering intensity) remain in the detector in the form of a variation of the dark current. *Right* Dark current image taken with an almost brand new *Princeton Instruments Pixis* camera, as used at the PETRA III. The dark current is very homogeneous

measurements with several hundreds of frames, not all frames can be simultaneously loaded into memory. In that case, the procedure is repeated such that only part of the pixels are read from all files and the mean is calculated for these pixels until the mean for all pixels has been calculated (Fig. 4.2).

The obtained dark current intensity values are subtracted from the obtained scattering intensity images before further processing.

4.2 Obtaining Correlation Times from Intensity Data

After subtracting the dark current, the actual intensity information can be processed further. We have seen in Sect. 2.1.3 that the intensity is Gamma-distributed for continuous speckle patterns. However, for the wide angle measurements performed in aXPCS, the coherent intensities are comparatively low. Thus the intensities can be expressed by photon events. The photon count can be described by Poisson-Gamma statistics (Goodman 2007) with number of speckles M and gamma function $\Gamma(M)$:

$$P(k) = \frac{\Gamma(k+M)}{\Gamma(M)\Gamma(k+1)} \left(1 + \frac{M}{\langle k \rangle}\right)^{-k} \left(1 + \frac{\langle k \rangle}{M}\right)^{-M} \tag{4.1}$$

Here, k is the number of photons measured in a pixel and $\langle k \rangle$ is the mean number of photons per pixel. For low intensities I, the signal-to-noise ratio can be approximated by

$$\mathrm{SNR} \approx \beta \langle I \rangle \sqrt{N_\mathrm{p} N_\mathrm{f}}, \tag{4.2}$$

with contrast factor β, the number of pixels N_p and the number of frames N_f taken during the measurement (Lumma et al. 2000; Chushkin et al. 2012). Due to the low count rates, the Poisson-Gamma statistics are hard to distinguish from Poisson noise. Thus, care has to be taken to ensure that the photons are accurately counted and assigned to the correct pixels. This is done with the so-called droplet algorithm. The obtained photon events can then be correlated for further analysis (Fig. 4.3).

4.2.1 Histogram

In order to obtain the single photon events, it is necessary to identify the actual elastic photon energy in detector units. The sensitivity of a CCD detector can be tuned by changing the gain. The digital signal output of the detector is given in ADUs, which are dependent on the gain. A straightforward approach to identify the actual energy connected to an ADU (which does not necessarily work if strong fluorescence is involved, as we will see later on) is identifying the highest peak in the intensity histogram. As aXPCS is based on elastic scattering, the energy spread of the

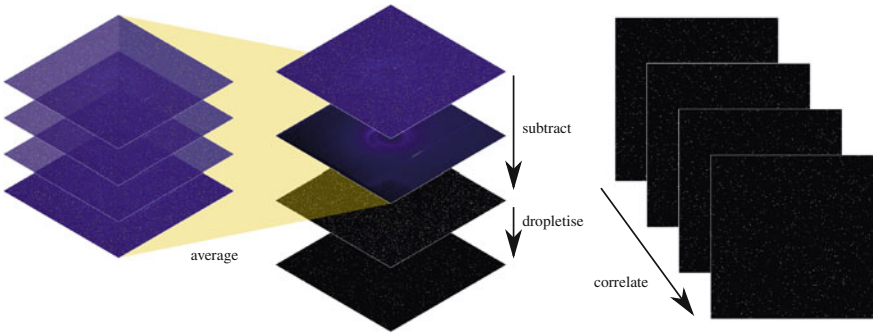

Fig. 4.3 Data processing steps. *Left* The dark current is calculated from the average of the gathered frames after removing the photon events. *Middle* The dark current is subtracted and the droplet algorithm is applied for each frame. *Right* The autocorrelation of the photon events of all frames is calculated

detected photons should be very narrow. Typically, photons within an energy range of ± 100 ADU were also considered to be caused by elastic scattering, where a typical photon energy of 8 keV corresponded to about 2000 ADU in the measurements for this thesis. After equating the ADU value of the main peak in the histogram with the elastic photon energy, other peaks in the histogram can be assigned to effects of electron escape and in some cases, fluorescence (see Sect. 6.2.1). Escape peaks result from Si fluorescence in the silicon layer, which can occur for energies above the silicon K-edge energy (1.839 keV). This interaction can lead to a photon being emitted and escaping the detector or being absorbed at another position in the detector as either a 1.74 keV or as a 1.836 keV photon event (McCarthy et al. 1997). In that case the energy of the original elastic photon is detected as two separate energies, one of about the K-edge energy and one of about the elastic energy minus the K-edge energy of silicon (see Fig. 4.4).

4.2.2 Droplet Algorithm

When a photon interacts with the photosensitive layer of the CCD, a charge cloud forms. This photoelectric charge cloud expands in size when travelling to the electrodes. Thus, most photon events cause multiple pixels of the detector to register an intensity as if the photon was spread over multiple pixels (Miyata et al. 2003; Ponchut 2008). If multiple photon events occur at the same position, it can be difficult or even impossible to separate the position and energy of the incident photons. For low intensities, as it is the case in aXPCS, typically only on the order of 10^4 photons are registered per frame out of the total of about 10^6 pixels on the detector. Thus, only very few photon events occur at the exact same detector position within

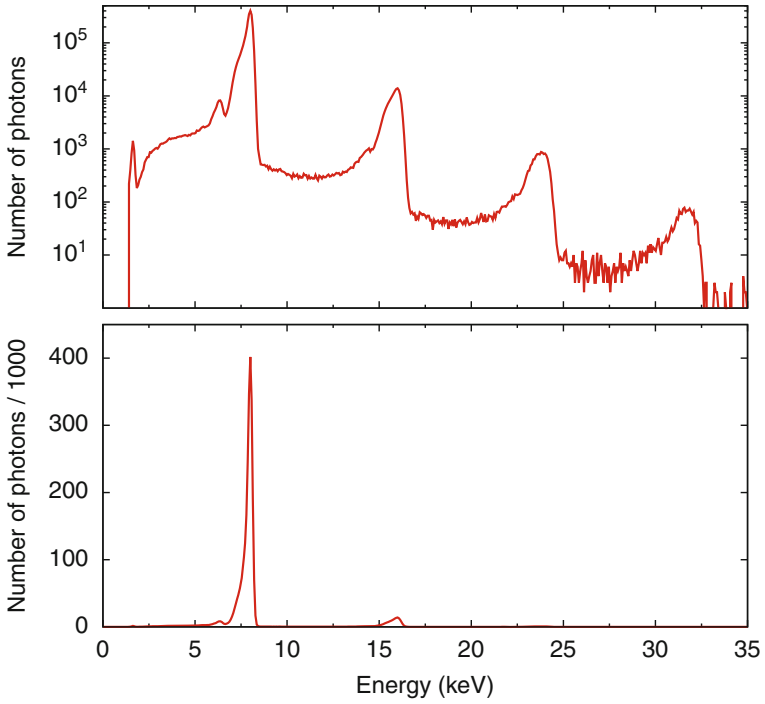

Fig. 4.4 Histogram of a $(Rb_2O)_2(B_2O_3)_{98}$ sample in logarithmic (*upper plot*) and linear scale (*lower plot*). Besides the elastic photon at 8 keV, small peaks of Si fluorescence at about 1.7 keV and Si escape of the elastic photons at about 6.3 keV are visible. At higher energies, multi-photon events are detected

one frame. All other events can be clearly separated and attributed to the according pixels with the droplet algorithm (Fig. 4.5).

The droplet algorithm identifies the position and energy of the incident photons (Livet et al. 2000; Chushkin et al. 2012; Leitner 2012). For that, a lower-intensity threshold is defined (typically about 30 ADU). Adjacent pixels which detect energies above this threshold are taken to belong to the same droplet. Additionally, a lower threshold for the value of the highest-intensity pixel in the droplet is defined (typically about 500 ADU) to avoid droplets which are spread so far that no correct position detection could be expected. The intensities of all pixels belonging to one droplet are added and give the energy of the according photon. The position of the photon is calculated by weighting each pixel position with its intensity value and averaging over all droplet pixels. The photons with energies which do not agree with the elastic energy (within a certain range) are discarded. For fast subsequent processing, only single-photon events are included and saved as binary information (where a binary *1* corresponds to the detection of a photon with an energy in the aforementioned elastic energy range).

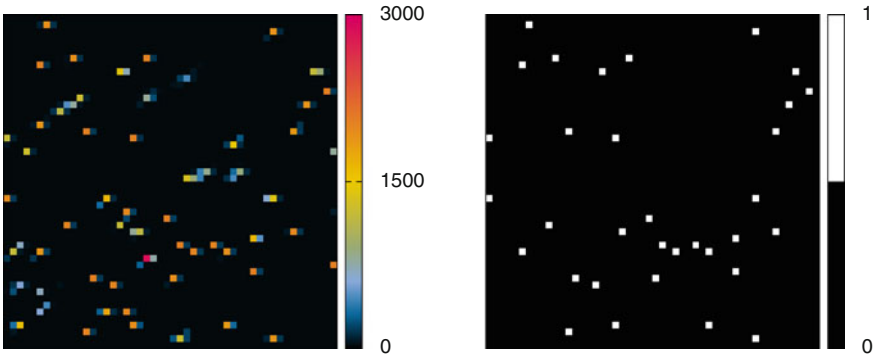

Fig. 4.5 Principle of operation of the droplet algorithm, shown for a 50 × 50 pixels section of the detector. The most probable pixel for the detected photon on the discretised detector area is obtained. *Left* Intensities before applying the droplet algorithm. The *colour* represents the intensity in ADU. *Right* Photon positions obtained from intensity droplets. The intensity is now binary information. Only droplets in the correct intensity range are taken into account

4.2.3 Autocorrelation

In order to gain real-space information, the intensity autocorrelation has to be obtained, as shown in Sect. 2.2.3. Experimentally, this can be realised by taking a set of frames over time and calculating the autocorrelation function Eq. (2.40) in the form

$$g^{(2)}(\vec{q}, \Delta t) = \frac{\left\langle \left\langle I_p(\vec{q}, t) I_p(\vec{q}, t + \Delta t) \right\rangle_t \right\rangle_p}{\left\langle \left\langle I_p(\vec{q}, t) \right\rangle_t^2 \right\rangle_p}, \tag{4.3}$$

with intensity $I_p(\vec{q}, t)$ at pixel p, averaging over all pixels and time-averaging over all frames. A typical measurement run consists of several hundred frames.

Due to the low, discrete values of intensity and due to the large number of zero events in the data that do not contribute to $g^{(2)}(\vec{q}, \Delta t)$, the computation of Eq. (4.3) can be significantly simplified by processing the intensities as binary data and neglecting multi-photon events (Leitner 2012) or utilising an event correlation scheme including multi-photon events (Chushkin et al. 2012).

As shown in Sect. 2.4.2, the experimentally obtained intensity correlation values can be linked to the dynamics:

$$g^{(2)}(\vec{q}, \Delta t) = 1 + \beta \, \mathrm{e}^{-2(\Delta t / \tau(\vec{q}))^{\alpha}} \tag{4.4}$$

The fit yields values for τ and α at each q value (see Fig. 4.6). While α is typically constant for all q values, the correlation time has a characteristic q dependence $\tau(q)$.

The averaging over q assumes that the detector is far away from the scattering centre and that the spread of q values of the elastic photons impinging on the detector is negligible, implying that also the corresponding correlation times show

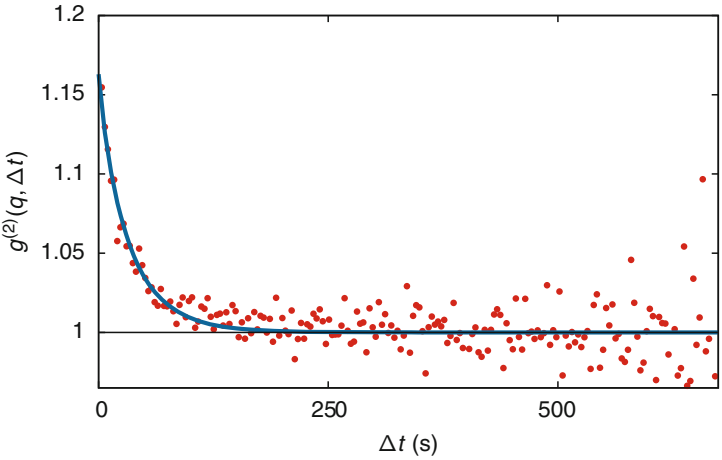

Fig. 4.6 Autocorrelation function $g^{(2)}(q, \Delta t)$ in a slowly cooled $(Rb_2O)_2(B_2O_3)_{98}$ sample fitted using Eq. (4.4) with the parameter $\alpha = 0.9$ (see Sect. 6.2.2). The experimental values were obtained at $q \approx 0.4\,\text{Å}^{-1}$ and $T = 20\,\text{K}$. The baseline at $g^{(2)} = 1$ is shown for comparison. Error bars are not shown for visibility and clarity of the fitting curve

only small deviation. While this is normally true, for significant changes in intensity within the q range covered by the detector, averaging causes a systematic error. Typically, this error is smaller than the statistical error for aXPCS measurements. In $(PbO)_{60}(SiO_2)_{40}$, due to the long runtime of the experiment and due to the changes in scattering intensity with increasing q, the systematic errors were significantly larger than the statistical ones (see Sect. 5.2.3). This was accounted for by virtually splitting the detector area into stripes of equal angular span where the correlation time should not change significantly. In that case, the errors have been derived from the difference of the average to the extremum.

4.2.4 Two-Time Correlation

Additional information on the stability of the setup and the dynamics can be obtained by calculating the two-time correlation from the collected intensity data. It is defined as the correlation of the intensities at two different times t_1 and t_2 at scattering vector $\vec{q}$, averaged over all detector pixels p:

$$C(\vec{q}, t_1, t_2) = \frac{\left\langle I_p(\vec{q}, t_1) I_p(\vec{q}, t_2) \right\rangle_p}{\left\langle I_p(\vec{q}, t_1) \right\rangle_p \left\langle I_p(\vec{q}, t_2) \right\rangle_p} \tag{4.5}$$

The two-time correlation function is widely used to study changes in dynamics during experiments, e.g. to study ageing phenomena (Malik et al. 1998; Madsen

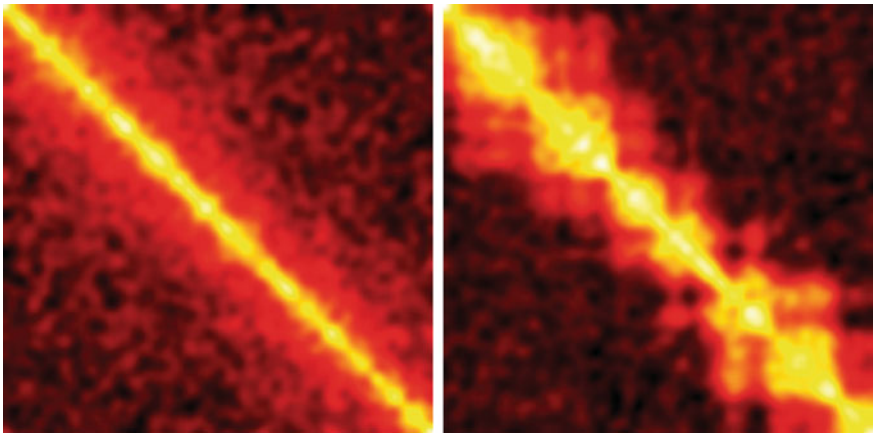

Fig. 4.7 Two-time correlation plotted as a colour map with t_1 and t_2 as axes. *Left* Typical image for stable sample. *Right* Due to instabilities, the speckle patterns decorrelate inhomogeneously

et al. 2010; Czakkel and Madsen 2011). A graphical representation of the two-time correlation is typically plotted as a colour map with t_1 and t_2 as axes. The colour map is convoluted with a Gaussian kernel to optically reduce noise. The ensemble averages are performed over the detector pixels, all having practically the same q value. The two-time correlation function can be characterised by the time distance $|t_1 - t_2|$ from the diagonal in perpendicular direction. In equilibrium systems, the two-time correlation functions are only dependent on the time difference. This can be seen in the colour map as parallel contour lines (Sutton et al. 2003; Fluerasu et al. 2007). If there are instabilities in the experimental setup or dynamic heterogeneities in the sample, deviations from this parallel contour lines occur (see Fig. 4.7). Thus, the two-time correlation function can be used to check the stability of the setup.

4.3 Extracting Dynamics from Correlation Times

From the correlation time $\tau(\vec{q}\,)$ obtained by the intensity autocorrelation, information on the atomic dynamics can be deduced. This is done by fitting different theoretical models (see Sect. 2.3) to the correlation time and analysing the resulting parameters.

Depending on the model, one or multiple jump lengths l and the mean residence times τ_0 of atoms at their positions can be obtained. Via the Einstein relation (Einstein 1905)

$$D = \frac{\langle l^2 \rangle}{6\tau_0}, \tag{4.6}$$

the diffusivity can be obtained.

4.4 Evaluating in Real-Time During Experiments

Due to the data acquisition and readout time of the detector, the most appropriate correlation times for aXPCS experiments are on the order of 10^2 s. Correlation times which are significantly faster are often not detectable. Significantly longer correlation times increase the measurement time accordingly, which should be avoided due to the limited beamtime and potential instabilities in the synchrotron radiation source over time. As the correlation time depends on the diffusion rate which in turn depends on the temperature, varying the sample temperature can be used to influence the correlation time. The most appropriate temperature can often be roughly estimated from literature diffusion data. However, the optimal temperature is most reliably found experimentally. For that, it is necessary to be able to quickly analyse the measured data and use the obtained correlation times as feedback for the temperature finding process. This is achieved by using the fast droplet algorithm described above and with several data handling scripts, allowing direct access to and automated processing of the obtained data.

References

Broennimann, C., Eikenberry, E. F., Henrich, B., Horisberger, R., Huelsen, G., Pohl, E., et al. (2006). The PILATUS 1M detector. *Journal of Synchrotron Radiation*, *13*(2), 120–130.

Chushkin, Y., Caronna, C., & Madsen, A. (2012). A novel event correlation scheme for X-ray photon correlation spectroscopy. *Journal of Applied Crystallography*, *45*(4), 807–813.

Czakkel, O., & Madsen, A. (2011). Evolution of dynamics and structure during formation of a cross-linked polymer gel. *Europhysics Letters*, *95*(2), 28001.

Einstein, A. (1905). Über die von der molekularkinetischen Theorie der Wärme geforderte Bewegung von in ruhenden Flüssigkeiten suspendierten Teilchen. *Annalen der Physik*, *322*(8), 549–560.

Fluerasu, A., Moussaïd, A., Madsen, A., & Schofield, A. (2007). Slow dynamics and aging in colloidal gels studied by X-ray photon correlation spectroscopy. *Physical Review E*, *76*(1), 010401.

Goodman, J. W. (2007). *Speckle phenomena in optics: Theory and applications*. Englewood: Roberts & Company.

Johnson, I., Sadygov, Z., Bunk, O., Menzel, A., Pfeiffer, F., & Renker, D. (2008). A Geiger-mode avalanche photodiode array for X-ray photon correlation spectroscopy. *Journal of Synchrotron Radiation*, *16*(1), 105–109.

Leitner, M. (2012). *Studying atomic dynamics with coherent X-rays*. Berlin: Springer.

Livet, F., Bley, F., Mainville, J., Caudron, R., Mochrie, S. G. J., Geissler, E., et al. (2000). Using direct illumination CCDs as high-resolution area detectors for X-ray scattering. *Nuclear Instruments and Methods in Physics Research Section A*, *451*(3), 596–609.

Lumma, D., Lurio, L. B., Mochrie, S. G. J., & Sutton, M. (2000). Area detector based photon correlation in the regime of short data batches: Data reduction for dynamic X-ray scattering. *Review of Scientific Instruments*, *71*(9), 3274.

Madsen, A., Leheny, R. L., Guo, H., Sprung, M., & Czakkel, O. (2010). Beyond simple exponential correlation functions and equilibrium dynamics in X-ray photon correlation spectroscopy. *New Journal of Physics*, *12*(5), 055001.

Malik, A., Sandy, A., Lurio, L., Stephenson, G., Mochrie, S., McNulty, I., et al. (1998). Coherent X-ray study of fluctuations during domain coarsening. *Physical Review Letters*, *81*(26), 5832–5835.

McCarthy, K. J., Owens, A., & Keay, A. (1997). Escape peak ratios in silicon X-ray charge coupled devices (CCDs). *Nuclear Instruments and Methods in Physics Research Section A*, *384*(2–3), 403–409.

Miyata, E., Miki, M., Hiraga, J., Kamiyama, D., Kouno, H., Tsunemi, H., et al. (2003). Mesh experiment for back-illuminated CCDs in improvement of position resolution. *Nuclear Instruments and Methods in Physics Research Section A*, *513*(1–2), 322–326.

Ponchut, C. (2008). Correction of the charge sharing in photon-counting pixel detector data. *Nuclear Instruments and Methods in Physics Research Section A*, *591*(1), 311–313.

Ponchut, C., Rigal, J. M., Clément, J., Papillon, E., Homs, A., & Petitdemange, S. (2011). MAXIPIX, a fast readout photon-counting X-ray area detector for synchrotron applications. *Journal of Instrumentation*, *6*(01), C01069–C01069.

Strauss, M. G., Naday, I., Sherman, I. S., Kraimer, M. R., Westbrook, E. M., & Zaluzec, N. J. (1988). CCD sensors in synchrotron X-ray detectors. *Nuclear Instruments and Methods in Physics Research Section A*, *266*(1–3), 563–577.

Sutton, M. (2008). A review of X-ray intensity fluctuation spectroscopy. *Comptes Rendus Physique*, *9*(5–6), 657–667.

Sutton, M., Laaziri, K., Livet, F., & Bley, F. (2003). Using coherence to measure two-time correlation functions. *Optics Express*, *11*(19), 2268.

Willmott, P. (2011). *Applications of synchrotron light to scattering and diffraction in materials and life sciences*. New York: Wiley.

Chapter 5
Proof of Concept: Direct Observation of Atomic Diffusion in Glasses

The main question this thesis addresses is if aXPCS can follow atomic jumps in glasses. As a showcase material, the binary network former lead silicate glass was chosen. An important question arising for this material is how the dynamics are connected to the network forming properties of its components. To show that this question can indeed be addressed with aXPCS, the following route was taken: First, glass samples in both network forming regions of lead silicate glass were produced. Then, both samples were studied with coherent X-rays. Finally, appropriate models for the dynamics were found and tested, yielding insight into the change in dynamics with the change in structure of the studied material. The results presented here were published recently (Ross et al. 2014).

A multitude of measurements was performed on lead silicate glasses. We will first review previous findings and then look into the new insight obtained with aXPCS in the framework of this thesis.

5.1 Previous Studies of Lead Silicate Glasses

Silicate glasses are among the most widely used glasses. A very important subgroup are the lead silicate glasses. These glasses are utilised especially for optical elements like holey fibres (Petropoulos et al. 2003), electronic devices and radiation shielding because of their high refractive index, high resistance against devitrification and high X-ray absorption. The ability to form these glasses over a wide range of compositions suggests the special role of lead in this material in structural and dynamic terms.

5.1.1 Structure

First X-ray studies on lead silicate glasses were carried out in the 1930s (Bair 1936), suggesting structural similarities between lead silicate and the soda silicate glasses

M. Ross, *Atomic Diffusion in Glasses Studied with Coherent X-Rays*,
Springer Theses, DOI 10.1007/978-3-319-28646-4_5

studied by Warren (1934). Later, more detailed information on the coordination numbers of the elements of lead silicate glasses could be obtained. It was proposed that PbO polyhedra are building blocks of the lead silicate glasses (Rybicki et al. 2001; Takaishi et al. 2005; Kohara et al. 2010). These polyhedra were described as either edge-shared PbO_3 trigonal pyramids (Takaishi et al. 2005) or as a broad distribution of PbO_x polyhedra with $x = 3 - 5$ (Kohara et al. 2010). It was shown that lead oxide can act both as a glass former and a network modifier. The molar fraction for which lead oxide changes its role to being the network former was reported to be above 40–60 mole% PbO (Takaishi et al. 2005; De Sousa Meneses et al. 2006; Feller et al. 2010). This network-forming and network-modifying capability of lead silicate glasses explains the wide compositional range of lead silicate glasses and sets them apart from most alkali silicate and borate glasses.

The structure of lead silicate glasses was studied in detail by X-ray diffraction (Takaishi et al. 2005; Kohara et al. 2010) and neutron scattering (Yamada et al. 1986; Takaishi et al. 2005). The X-ray diffraction studies have revealed two distinct peaks in the radial distribution function, which gives insight into the average radial distance of the scatterers. The first peak, representing the nearest-neighbour distance of lead atoms, was found around 3.8 Å. This peak is independent of composition, indicating a definite structure of the lead groups with covalent Pb–Pb bonding (Rabinovich 1976; Takaishi et al. 2005). The lead-lead interaction was also interpreted as a consequence of the polarisability of lead ions (Rabinovich 1976). The second peak, representing the second-nearest-neighbour distance of lead atoms, appears at about 6.5–7.5 Å (Rabinovich 1976; Imaoka et al. 1986; Takaishi et al. 2005). A model of PbO_3 chains, connected by silica chains has been proposed. For disparate structural models, similar radial distribution functions were obtained, thus a definite structural model was difficult to establish (Imaoka et al. 1986). X-ray and neutron diffraction patterns were combined to show how the lone electron pairs of ionised Pb^{2+} atoms are arranged, leading also to the conclusion of pyramidal PbO_x polyhedra with $x = 3 - 4$ (Alderman et al. 2013).

Studies in binary lead silicate glasses were carried out with NMR (Yoko et al. 1992; Takaishi et al. 2005; Feller et al. 2010). It was concluded that lead forms covalent PbO_4 and PbO_3 pyramids (see Fig. 5.1) over a large compositional range (Fayon et al. 1998).

Reverse Monte Carlo (RMC) simulations were done to gain a three-dimensional structural model of lead silicate glass. The structure was determined as ordered distribution of Pb in the glass, with irregular PbO_4 pyramids as building blocks (Suzuya et al. 1999). While Monte Carlo (MC) simulations can yield structural insight (see Fig. 5.2 for a structure achievable with MC), they are typically not able to grasp the dynamics of the simulated material. This is normally attempted with Molecular Dynamics (MD). However, MD simulations have focused on structural rather than dynamic insight on a broad range of glass formation (Rybicki et al. 2001; Witkowska et al. 2005). MD data and EXAFS results combined show that for any concentration of PbO, the PbO_4 groups are the dominant structural units and that PbO_3 and PbO_4 structures can coexist at lower PbO concentrations (Rybicki et al. 2001).

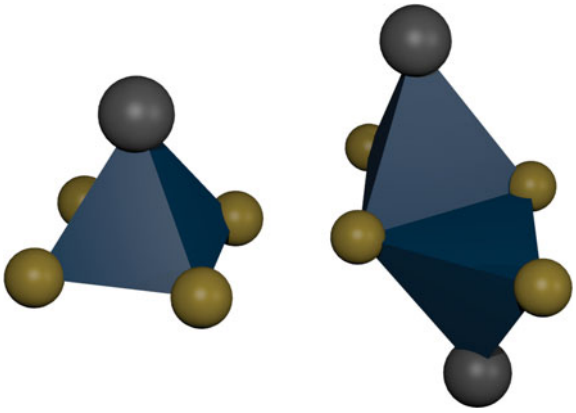

Fig. 5.1 Visualisation of proposed structures of lead oxide building blocks. The *grey* spheres represent lead atoms, the smaller *yellow* spheres represent oxygen atoms. *Left* PbO_4 pyramid. *Right* Edge-sharing tetrahedrons of PbO_3

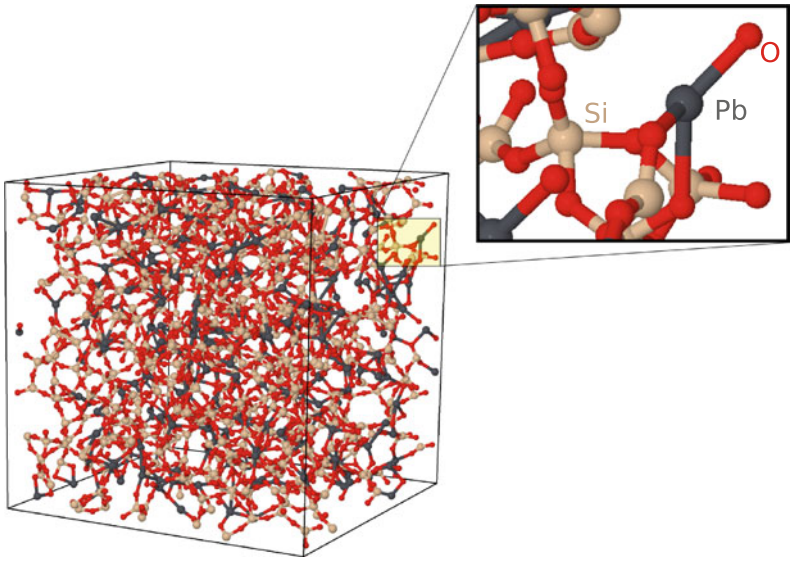

Fig. 5.2 Ball-and-stick visualisation of a lead glass structure, based on data of an MC simulation

There has been some speculation about the existence of micro-inhomogeneities as a consequence of frozen-in fluctuations in lead silicate glasses. SAXS measurements were interpreted as showing the occurrence of micro-inhomogeneities with a size of 5–7 Å in lead glasses in the region above 40 mole% PbO (Golubkov et al. 1999).

The short-range order was also studied by Raman spectroscopy (Furukawa et al. 1978; Feller et al. 2010) and IR spectroscopy (De Sousa Meneses et al. 2006; Feller et al. 2010), yielding indications for a separate lead oxide glass network in high lead concentration regions.

Although many studies were carried out since the first X-ray studies on lead silicate glasses, their structure has not been fully explained yet. To sum up the most important findings with respect to this thesis: The structure of lead silicate glasses $(PbO)_x(SiO_2)_{1-x}$ depends on the fraction of PbO (Rabinovich 1976). A significant structural change takes place in the compositional region of 40–60 mole% PbO (Takaishi et al. 2005; De Sousa Meneses et al. 2006; Feller et al. 2010). The structure of lead silicate glass can be described in terms of the silicate and the lead network. In low lead content glass, Pb atoms are randomly distributed in the voids of the three-dimensional silicon-oxygen network. There, each lead atom is linked by two oxygen atoms, acting as a modifier of the silicon-oxygen network, with charge state Pb^{2+}. With increasing lead content, lead starts to form the network. Then, the lead structure can be explained as chain-like, where the interatomic interaction is nonpolar (Golubkov et al. 1999). At this compositional region, the three-dimensional silicon-oxygen network is no longer present. Instead, isolated silicon-oxygen groups are linked together by lead ions (Rabinovich 1976; Kohara et al. 2010).

5.1.2 Dynamics

The dynamic behaviour of silica glass and other glassy materials is even less understood than the structure. Lead silicate glass is of specific interest also in dynamic terms, as Pb^{2+} can cause ionic conduction through the glass. Also the components lead oxide and silica oxide both can act as network formers, thereby influencing the dynamics. Gaining insight into the dynamics then raises the question of how these play along with the network-forming role of each component and the changes with composition. One of the main reasons for the lack of information in this field has been the fact that no method was able to study glassy dynamics spatially resolved on the appropriate length and time scales.

Glasses are commonly defined as metastable liquids. It was shown in experiments on metallic glasses (Leitner et al. 2012; Ruta et al. 2012) that ageing in the glassy state is widely present. This ageing is not the focus of this thesis. Rather, the atomic equilibrium dynamics in a glass shall be studied. Network glasses like lead silicate glasses are in that respect an ideal material as the ageing below the glass transition temperature in these materials is many orders of magnitude slower than the measurement times of aXPCS.

Experimental studies of lead diffusion in lead silicate glasses (Lindner et al. 1960) are rare. The diffusion behaviour of Pb^{2+} ions in lead silicate glasses in the context of leaching was measured, indicating that the PbO network percolates for high lead concentrations to form diffusion paths for the lead ions (Mizuno et al. 2005).

5.2 New Insight into Lead Silicate Glasses

For the lead glass diffusion measurements, two different sample compositions were prepared (see Sect. 3.1.1), with composition formula $(PbO)_x(SiO_2)_{1-x}$. The lead silicate oxide glass sample with mixing ratio $x = 30$ mole% will be referred to as low lead content glass and the sample with $x = 60$ mole% will be referred to as high lead content glass. This selection is due to the substantial difference in the structure of lead silicate glasses for concentrations below and above 40–60 mole% PbO. PbO-SiO_2 can be classified as a binary network-former glass (Kohara et al. 2010), where in a low lead content glass SiO_2 forms the network. In a high lead content glass, PbO acts as the former of the network structure. It is of great interest how this change in structure reflects on the dynamics in both regions.

5.2.1 Scattering Intensities

As we have seen in Sect. 2.4.3, the scattering intensities are relevant for taking into account the influence of short-range order on the dynamics. Scattering curves of the measured glasses were obtained by conventional X-ray scattering (see Sect. 3.3.3) to correct for this influence and to ensure that there are no signs of crystallisation in the samples. No sharp peaks or other signs of crystallisation were observed, see Fig. 5.3. A broad peak was found for low lead content glass at a wave vector of about 0.6 $Å^{-1}$ and with lower intensity for high lead content glass at about 0.8 $Å^{-1}$. This confirms

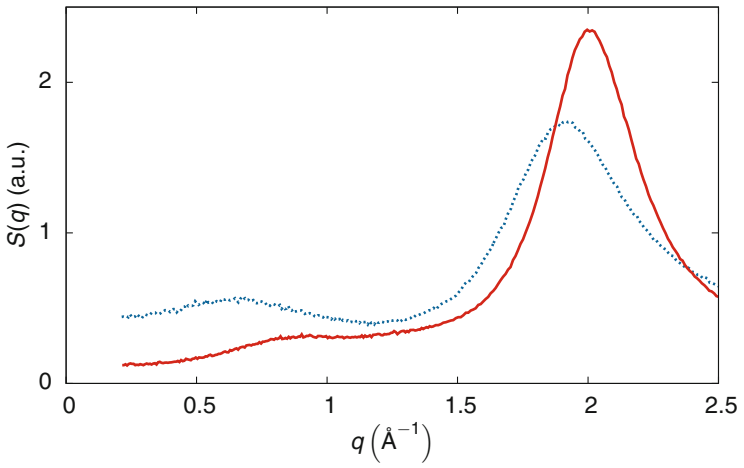

Fig. 5.3 Scattering intensities obtained after the experiment for low (*blue dashed line*) and high lead content glass (*red solid line*). Data published in Ross et al. (2014)

observations of Kohara et al. (2010), where with increasing lead content a prepeak at low q values with decreasing intensity was found and interpreted as signature of an inhomogeneous distribution of PbO_x polyhedra. The main peak, also called glass peak, is found at about $2\,\text{Å}^{-1}$.

5.2.2 Glass Temperatures

Glass temperatures for $(PbO)_{60}(SiO_2)_{40}$ were reported to be in the range of 640–650 K (Zahra et al. 1993; Feller et al. 2010). In order to ensure that the aXPCS measurements are in the vitreous state, Differential Scanning Calorimetry (DSC) measurements were done on a *Netzsch DSC 204 Phoenix* to check the actual glass transition temperatures for the samples prepared for this thesis (Fig. 5.4). Values of $T_g > 663\,\text{K}$ were obtained. The aXPCS measurements on this composition were performed at 643 K, thus staying clearly below the glass transition temperature. Analogously, the glass temperatures for $(PbO)_{30}(SiO_2)_{70}$ were measured with DSC. The obtained value of $T_g > 753\text{K}$ is also above the literature data of around 730–740 K (Zahra et al. 1993; Feller et al. 2010). The aXPCS measurements on this composition were performed at 713 K, again staying below T_g.

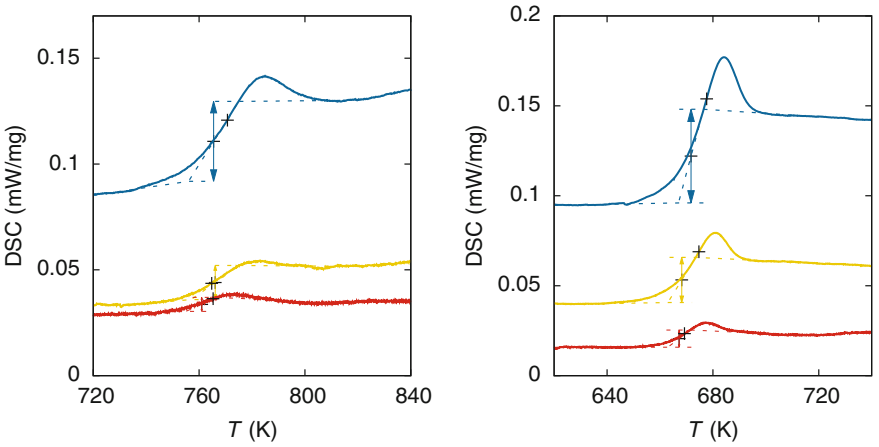

Fig. 5.4 Differential scanning calorimetry measurement after the experiment for low (*left*) and high lead content glass (*right*). The *blue* upper curve was obtained with a cooling rate of 20 K/min, the *yellow* middle curve with 10 K/min and the lower *red* curve with 5 K/min

5.2.3 Atomic Dynamics

The two-time correlation is checked for all measurements to ensure that no ageing takes place during the experiment. No significant broadening of the contour lines is observed, indicating that no macroscopic ageing phenomena or instabilities on the measurement time scale are present (see Sect. 4.2.4). Compared to metallic glasses, ageing in oxide glasses is much less pronounced. A similar observation of the absence of ageing during the measurement on the atomic scale was recently reported by Ruta et al. (2014).

The intensity of X-ray scattering is as a first approximation proportional to the square of the electron density, thus the Pb atoms contribute by far most to the scattered intensity. This allows to interpret the scattering data exclusively in terms of lead diffusion and to specifically follow the motion of lead atoms.

As a strong initial diminishment in contrast can be an indication for processes on faster time scales than resolvable, the measured contrasts are compared to expected values. The dependence of the coherence values on the scattering vector is shown in Fig. 5.5. The obtained coherence factors are similar to the values measured on a standard metallic scatterer (Cu-Au, with no dynamics in the sample) and to values typically measured at this beamline setup.

The correlation times were obtained from the autocorrelation of the intensity patterns at different q vectors with a free coherence factor β and a KWW parameter $\alpha = 1$ for low lead content and $\alpha = 0.75$ for high lead content glass. The plot of the intensity autocorrelation and the fit for the correlation time are shown in Fig. 5.6.

By covering a q range up to values of about 2.5 Å^{-1}, insight into the dynamics on the atomic scale is obtained.

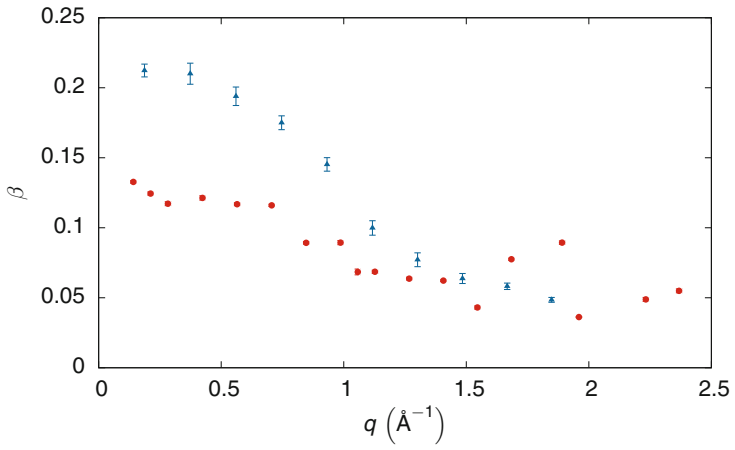

Fig. 5.5 Contrast factor dependence on scattering vector for low (*blue triangles*) and high lead content silicate glass (*red circles*)

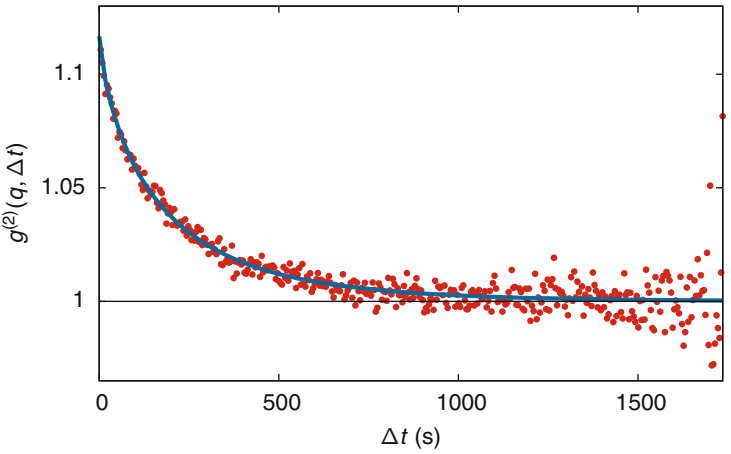

Fig. 5.6 Autocorrelation function $g^{(2)}(q, \Delta t)$ in the high lead content glass sample fitted using Eq. (4.4) with the parameter $\alpha = 0.75$. The experimental values were obtained at $q \approx 0.7\,\text{Å}^{-1}$ and $T = 643\,\text{K}$. The baseline is shown for comparison. Data published in Ross et al. (2014)

Low Lead Content Glass

The experimentally obtained data points are fitted with appropriate jump models to give insight into the dynamics. These models are the single jump Chudley–Elliott model, the two-jump Chudley–Elliott model, the Jobic model with a mean jump distance and an additional delocalisation parameter of an atom from its site, and the model of uniformly distributed jumps (see Sects. 2.3.2 and 2.3.3). Different models were compared to the most straightforward single jump Chudley–Elliott model (see Fig. 5.7). Two of the models applied result in the same fit in the fitting range and are thus not shown in the figure. The fact that the two-jump Chudley–Elliott model with additional fitting parameters leads to the same fit shows that no additional details can be resolved with the assumption of multiple jump processes of PbO in low lead content glass. A third model yields a fit deviating more from the measured data than the single jump Chudley–Elliott model. Thus from the models discussed, the single jump Chudley–Elliott represents the data most appropriately while being most straightforward. Here it is assumed that an atom remains at a fixed position most of the time and only moves by quasi-instantaneous jumps over a fixed distance.

Fitting the data with the single jump Chudley–Elliott model yields a jump distance of $l \approx 8(1)$ Å with a mean residence time of $\tau_0 \approx 370\,\text{s}$. Comparing this jump length to available structural information shows that these atomic jumps are by far larger than the expected neighbouring distances of about 3.8 Å (see Sect. 5.1.1). This implies jump diffusion in a structure with regions of different lead contents. Micro-inhomogeneities were found in some glass types (Bus'ko et al. 2003), with sizes on the order of 10 Å. Also by MD and X-ray studies, aggregation of lead was found for similar compositions as the low lead content glass measured here (Kohara et al.

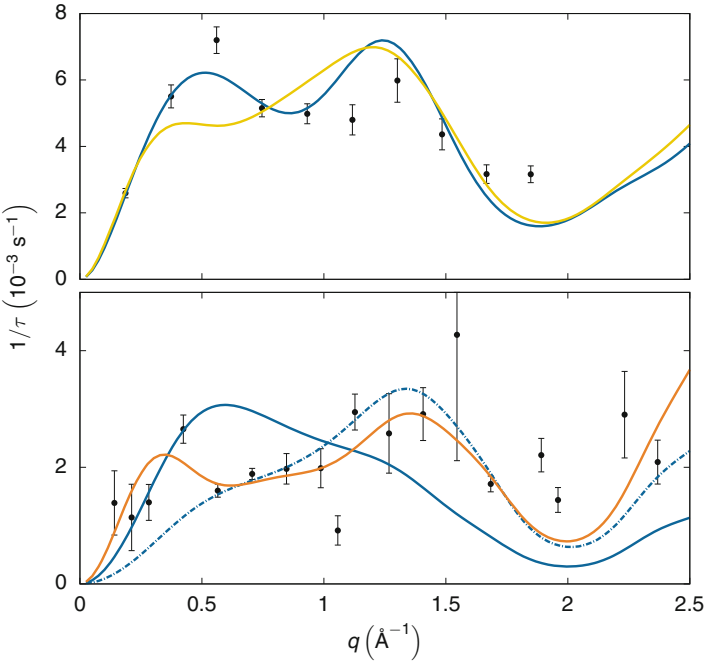

Fig. 5.7 Inverse correlation time dependence on scattering vector for low lead content glass at 713 K (*upper plot*) and high lead content glass at 643 K (*lower plot*). The curves show the fit of the single jump Chudley–Elliott model (*blue line*), the model of uniformly distributed jumps (*yellow line*) and two-jump Chudley–Elliott model (*orange line*) to the data. For the high lead content glass, the single jump Chudley–Elliott model was fitted for low (*solid blue line*) and high q values (*dot-dashed blue line*). Data published in Ross et al. (2014)

2010). Following the interpretation of large amounts of free volume, diffusive jumps are facilitated by absence of blocking PbO structures.

The KWW parameter of $\alpha = 1$ of the fit to the measured data indicates that the jump process has no memory of previous jumps. This further supports the picture of a single process in the form of jumps through a void structure. This diffusion must then be fast compared to the mean residence time as the void structures would otherwise not stay at a lower lead concentration compared to the lead-rich regions. The length of the diffusion jump of a lead atom and the void size should then be on the same order, which is in good agreement with the obtained results.

From the Einstein relation (see Sect. 4.3) the diffusivity can be calculated, leading to a value on the order of $10^{-22}\,m^2\,s^{-1}$. Diffusion coefficients measured in literature vary to a large extend for different measurements (Rabinovich 1976) and only rough estimations can be done. Tracer diffusion measurements in PbO–SiO_2 melts (Langanke and Schmalzried 1979) give diffusion coefficients at $T = 1123\,K$ on the order of $10^{-10}\,m^2\,s^{-1}$ for high lead content. With an activation energy of 118 kJ/mole

and assuming Arrhenius-like behaviour, diffusion coefficients are on the order of 10^{-14}–$10^{-15}\,m^2\,s^{-1}$ at the temperature of the measurements performed. This is by far faster than the diffusion coefficients obtained here, as this calculation is based on the assumption that the lead silicate melt stays in liquid state while cooling down and diffusion just decelerates according to the Arrhenius-law, neglecting the dramatic slowing down of the dynamics during glass formation. It is possible to estimate diffusivities via the Nernst-Einstein relation from literature data (Cohen et al. 1973; Topping et al. 1974), yielding values of $10^{-18}-10^{-17}m^2\,s^{-1}$. However, the comparison of the present measurements with these measurements is difficult due to the long annealing times in the sample preparation, leading to a better equilibrated system with much slower dynamics.

The low lead content diffusion can thus be envisioned as a process of a long residence at a rather fixed position aside a lead aggregate, a very fast diffusive motion through the unfavourable void regions and again a very long residence, temporarily fixed to yet another lead aggregate. The autocorrelation functions always decayed to the baseline for long measurement times, thus no indication for a localised motion besides the ubiquitous vibrational motions around these residence positions is found.

High Lead Content Glass

The dynamics of lead in high lead content glass was measured and modelled analogous to the low lead content glass (see Fig. 5.7). A fit of the single jump Chudley–Elliott model to the measured data indicates significant changes in the dynamics compared to the low lead content silicate glass. The Jobic model and that of uniformly distributed jump lengths yield the same fit in the fitting range as the single jump Chudley–Elliott model for short jump distances (up to $0.5\,Å^{-1}$). Both models are thus not shown in Fig. 5.7. However, the single jump Chudley–Elliott model is not able to reproduce the inverse correlation times for lower and higher q values at the same time. Extending the Chudley–Elliott model by a second jump process leads to a much more convincing model fit. With this model, the details of the data across the whole q range can be captured. This shows that the two-jump Chudley–Elliott model is the most appropriate jump model for high lead content glass as it is the most direct approach which captures all details of the experimental data.

This agrees well with the structural information of predominant network forming by lead oxide at this composition. As the percolation of lead-rich regions to a network leads to an intrinsic structural inhomogeneity on the short range, different jump processes along different jump directions are possible.

The fit of the two-jump Chudley–Elliott model (see Eq. (2.68)) yields $l_1 \approx 1.2(7)$Å, $l_2 \approx 13(3)$Å, $\omega_1 \approx 0.9$ and $\tau_0 \approx 435$s, where $\tau_0^{-1} = \tau_1^{-1} + \tau_2^{-1}$ and $\omega_i = \tau_i^{-1}/\tau_0^{-1}$. As the factor ω_i is the probability for a jump to have a distance l_i with a mean residence time τ_i, about 90 % of the atomic jump processes take place on a very short range. With a significantly lower probability of about 10 %, additional jumps take place on a longer range, comparable to the process in the low lead content glass. The KWW parameter $\alpha = 0.75$ of the fit supports the observation that a change in the diffusion mechanism occurs. This can be interpreted as result of the dynamic heterogeneity in glasses (see Sect. 1.1.2), where the dynamics of a lead atom depends

on its position in the structure. If it is at the edge of a void, it has a tendency for a jump through the void, whereas inside the structure, it moves along the network paths.

The overall diffusivity can be calculated from the Einstein relation, yielding a value on the order of $10^{-22}\,m^2\,s^{-1}$. When comparing to the low lead content results, one should note the lower temperature of the high lead content measurement. From tracer diffusion measurements (Langanke and Schmalzried 1979), diffusion coefficients can be extrapolated to be on the order of $10^{-12}m^2\,s^{-1}$ for low lead content. The same challenges as in the low lead content glass exist when comparing the obtained diffusion coefficients to literature data due to the more equilibrated sample with slower dynamics.

Comparison of Low and High Lead Content Glass

Comparing the aXPCS results for low and high lead content glass shows that a drastic change in dynamics occurs with composition. Previous studies have revealed that the structure of lead silicate glass is subject to large changes in the same compositional region (see Sect. 5.1.1). This indicates that the observed change in dynamics goes hand in hand with that in structure. Comparing the long-range jumps in low and high lead content glass shows that the maximum jump distance increases with increasing lead content. This seems counter-intuitive as the increasing concentration of lead should on average result in decreasing distances of lead atoms. This behaviour can be understood in terms of the structural and dynamic heterogeneity of lead atoms in high lead content glass. While at low concentrations diffusion takes place by jumps between the closest lead-rich regions, in high lead content glass the lead-rich regions are connected by network paths. Thus most jumps take place along those paths and jumps through the remaining voids are longer than between the gaps which exist between the lead-rich regions in low lead content glass (see Fig. 5.8). This is in good agreement with the results of Kohara et al. (2010), observing extraordinarily large amounts of free volume. Additional experimental support to this view is given by Kaur et al. (2013), finding that no abrupt increase in volume at the glass transition temperature occurs, which indicates that the structure of the system is not densely packed.

The nature of charge carriers in PbO–SiO_2 glasses is still uncertain (Abe et al. 1990). Pb^{2+} cations were proposed as current carriers, as well as impurity alkali metal ions, protons and electrons (Rabinovich 1976). Based on the aXPCS results obtained here, it can be concluded that lead atoms indeed move through the network structure at relatively low temperatures, supporting the idea of charge transport by lead cations.

In summary, a split of dynamics is found. In low lead content glass, longer-range jumps on the order of 8 Å take place. In high lead content glass, two jump processes occur on the order of 1 and 13 Å. This split in dynamics can be understood as a consequence of dynamic changes in analogy with structural changes, where direct jumps of lead between lead aggregates drive the dynamics for low lead content glass and short jumps along network structure and longer jumps through voids occur for

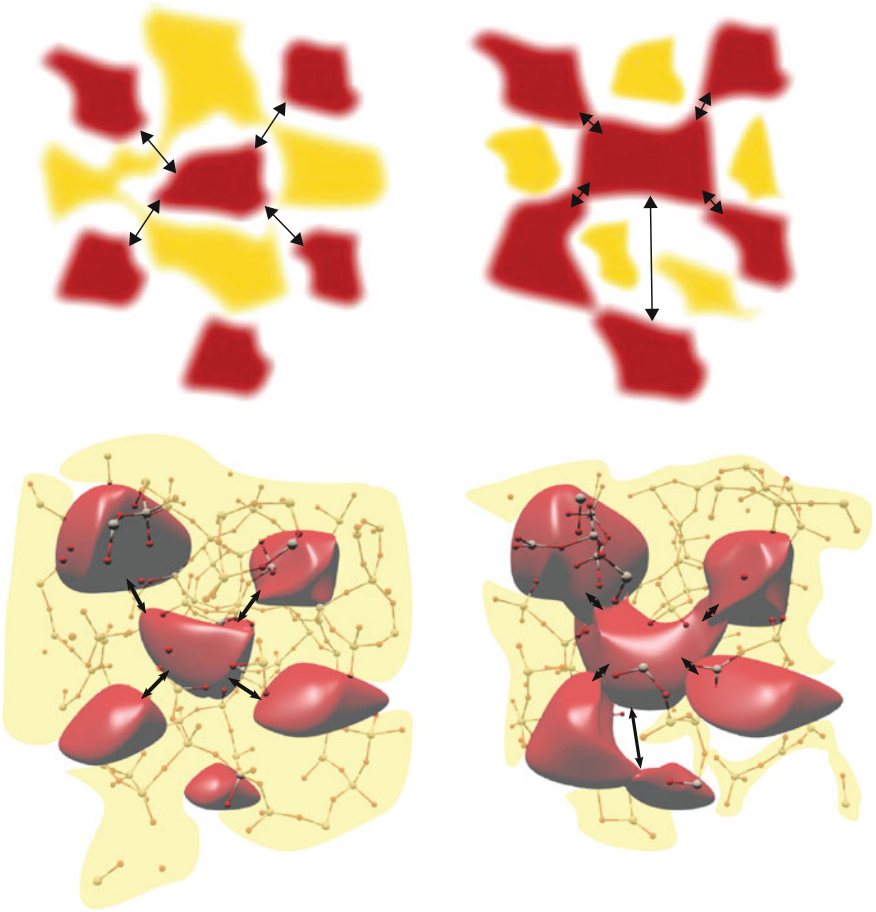

Fig. 5.8 Visualisation of jump processes of lead oxide in lead silicate glass in two (*upper figure*) and three dimensions (*lower figure*). Regions in *red* colour depict clusters of lead oxide and regions in *yellow* colour are silica oxide structures. *Left* In low lead content glass, the diffusive motion is a result of jumps between lead oxide clusters. *Right* In high lead content glass, there are two distinct types of jump processes. As the lead components are now connected along network paths, a short-range diffusion along these paths is possible. Additionally, the diffusion is driven by jump processes through the voids over longer distances. Published in Ross et al. (2014)

high lead content glass. In turn, the existence of jump processes on distinctly different length scales imply a partial aggregation of lead in high lead content glass and the existence of voids between these aggregations (see Fig. 5.8).

As has been shown, the technique of aXPCS yields detailed insight into atomic transport of lead in lead silicate glasses, revealing characteristic jump distances and the link between the structural heterogeneity and the change in the diffusion processes depending on composition. This opens up the door for studies on many other amor-

phous systems. We will take a look at a very intriguing and technically important material class and see how aXPCS can enhance the understanding of the materials of this kind in the next chapter.

References

Abe, Y., Hosono, H., Hikichi, Y., & Hench, L. L. (1990). Protonic conduction in PbO-SiO_2 glasses: A quantitative estimation. *Journal of Materials Science Letters*, *9*(12), 1443–1444.

Alderman, O. L. G., Hannon, A. C., Holland, D., Feller, S., Lehr, G., Vitale, A. J., et al. (2013). Lone-pair distribution and plumbite network formation in high lead silicate glass, $80PbO{\cdot}20SiO_2$. *Physical Chemistry Chemical Physics*, *15*(22), 8506.

Bair, G. J. (1936). The constitution of lead oxide-silica glasses: I, atomic arrangement. *Journal of the American Ceramic Society*, *19*(1–12), 339–347.

Bus'ko, I. Z., Golubkov, V. V., & Stolyarova, V. L. (2003). On the structure of low-alkali rubidium and cesium borate glasses and melts. *Glass Physics and Chemistry*, *29*(3), 267–275.

Cohen, B. M., Uhlmann, D. R., & Shaw, R. R. (1973). Optical and electrical properties of lead silicate glasses. *Journal of Non-Crystalline Solids*, *12*(2), 177–188.

De Sousa Meneses, D., Malki, M., & Echegut, P. (2006). Structure and lattice dynamics of binary lead silicate glasses investigated by infrared spectroscopy. *Journal of Non-Crystalline Solids*, *352*(8), 769–776.

Fayon, F., Bessada, C., Massiot, D., Farnan, I., & Coutures, J. P. (1998). ^{29}Si and ^{207}Pb NMR study of local order in lead silicate glasses. *Journal of Non-Crystalline Solids*, *232–234*, 403–408.

Feller, S., Lodden, G., Riley, A., Edwards, T., Croskrey, J., Schue, A., et al. (2010). A multispectroscopic structural study of lead silicate glasses over an extended range of compositions. *Journal of Non-Crystalline Solids*, *356*(6–8), 304–313.

Furukawa, T., Brawer, S. A., & White, W. B. (1978). The structure of lead silicate glasses determined by vibrational spectroscopy. *Journal of Materials Science*, *13*(2), 268–282.

Golubkov, V. V., Bogdanov, V. N., Pakhnin, A. Y., Solovyev, V. A., Zhivaeva, E. V., Kabanov, V. O., et al. (1999). Microinhomogeneities of glasses of the system PbO-SiO_2. *Journal of Chemical Physics*, *110*(10), 4897.

Imaoka, M., Hasegawa, H., & Yasui, I. (1986). X-ray diffraction analysis on the structure of the glasses in the system PbO-SiO_2. *Journal of Non-Crystalline Solids*, *85*(3), 393–412.

Kaur, A., Khanna, A., Singla, S., Dixit, A., Kothiyal, G. P., Krishnan, K., et al. (2013). Structure-property correlations in lead silicate glasses and crystalline phases. *Phase Transitions*, *86*(8), 759–777.

Kohara, S., Ohno, H., Takata, M., Usuki, T., Morita, H., Suzuya, K., et al. (2010). Lead silicate glasses: Binary network-former glasses with large amounts of free volume. *Physical Review B*, *82*(13), 134209.

Langanke, B., & Schmalzried, H. (1979). Ionic transport in PbO-SiO_2-Melts (I). Tracerdiffusion and chemical interdiffusion. *Berichte der Bunsengesellschaft für physikalische Chemie*, *83*(1), 59–64.

Leitner, M., Sepiol, B., Stadler, L.-M., & Pfau, B. (2012). Time-resolved study of the crystallization dynamics in a metallic glass. *Physical Review B*, *86*(6), 064202.

Lindner, R., Hassenteufel, W., Kotera, Y., & Matzke, H. (1960). Diffusion radioaktiven Bleies in Bleimetasilikatglas. *Zeitschrift für Physikalische Chemie*, *23*(5–6), 408–414.

Mizuno, M., Takahashi, M., Takaishi, T., & Yoko, T. (2005). Leaching of lead and connectivity of plumbate networks in lead silicate glasses. *Journal of the American Ceramic Society*, *88*(10), 2908–2912.

Petropoulos, P., Ebendorff-Heidepriem, H., Finazzi, V., Moore, R., Frampton, K., Richardson, D., et al. (2003). Highly nonlinear and anomalously dispersive lead silicate glass holey fibers. *Optics Express*, *11*(26), 3568.

Rabinovich, E. M. (1976). Lead in glasses. *Journal of Materials Science*, *11*(5), 925–948.

Ross, M., Stana, M., Leitner, M., & Sepiol, B. (2014). Direct observation of atomic network migration in glass. *New Journal of Physics*, *16*(9), 093042.

Ruta, B., Chushkin, Y., Monaco, G., Cipelletti, L., Pineda, E., Bruna, P., et al. (2012). Atomic-scale relaxation dynamics and aging in a metallic glass probed by X-ray photon correlation spectroscopy. *Physical Review Letters*, *109*, 165701.

Ruta, B., Baldi, G., Chushkin, Y., Rufflé, B., Cristofolini, L., Fontana, A., et al. (2014). Revealing the fast atomic motion of network glasses. *Nature Communications*, *5*.

Rybicki, J., Rybicka, A., Witkowska, A., Bergmański, G., Di Cicco, A., Minicucci, M., et al. (2001). The structure of lead-silicate glasses: Molecular dynamics and EXAFS studies. *Journal of Physics: Condensed Matter*, *13*(43), 9781–9797.

Suzuya, K., Kohara, S., & Ohno, H. (1999). A reverse monte carlo study of lead metasilicate glass. *Japan Society of Applied Physics*, *38*(S1), 144.

Takaishi, T., Takahashi, M., Jin, J., Uchino, T., Yoko, T., & Takahashi, M. (2005). Structural study on $PbO\text{-}SiO_2$ glasses by X-ray and neutron diffraction and ^{29}Si MAS NMR measurements. *Journal of the American Ceramic Society*, *88*(6), 1591–1596.

Topping, J. A., Harrower, I. T., & Murthy, M. K. (1974). Properties and structure of glasses in the system $PbO\text{-}GeO_2$. *Journal of the American Ceramic Society*, *57*(5), 209–212.

Warren, B. (1934). The diffraction of X-rays in glass. *Physical Review*, *45*(10), 657–661.

Witkowska, A., Rybicki, J., & Di Cicco, A. (2005). Structure of partially reduced $x\text{PbO}(1\text{-}x)\text{SiO}_2$ glasses: Combined EXAFS and MD study. *Journal of Non-Crystalline Solids*, *351*(5), 380–393.

Yamada, K., Matsumoto, A., Niimura, N., Fukunaga, T., Hayashi, N., & Watanabe, N. (1986). Short range structural analysis of lead silicate glasses by pulsed neutron total scattering. *Journal of the Physical Society of Japan*, *55*(3), 831–837.

Yoko, T., Tadanaga, K., Miyaji, F., & Sakka, S. (1992). A ^{207}Pb MAS-NMR study of Pb-containing glasses. *Journal of Non-Crystalline Solids*, *150*(1–3), 192–196.

Zahra, A.-M., Zahra, C. Y., & Piriou, B. (1993). DSC and Raman studies of lead borate and lead silicate glasses. *Journal of Non-Crystalline Solids*, *155*(1), 45–55.

Chapter 6
Practical Application: Tailoring Fast Ionic Diffusion

We have seen that aXPCS can yield insight into glassy dynamics on the atomic scale. The next goal is to utilise aXPCS to further the understanding of a material class of great practical relevance.

Fast ionic conductors are a class of systems with a relatively high conductivity even close to room temperature and below. They have great potential for tackling the current and future challenges in power supply and demand. On the supply side, an important problem of renewable energy technologies is the variability in terms of their power output on time scales of seconds to hours. On the demand side, mobile applications such as electric cars and smart devices require high-capacity and at the same time light storage devices. One promising path to overcome these challenges is the widespread usage of high-capacity batteries to bridge supply and demand peaks. This could be driven by a high adoption of electrical cars combined with a connection of their accumulators to the power grid. Specific requirements in terms of physical properties vary largely by battery technology, yet there is one peculiarity that most ionic electricity storage solutions have in common, namely that improvement of one specific property is in most cases connected to an impairment of other important qualities. This symptom is partially due to the still incomplete knowledge of the fundamental processes leading to conductivity in these materials.

Pure borate glass is generally insulating in nature. Alkali borate glasses show electrical conductivity due to the charge transport capability of the mobile alkali ions. We will look into this glass type as a model system for studying aXPCS in amorphous fast ionic conductors, as the ions in this material class move rather freely through the largely fixed glass matrix. First we will learn which insight previous studies have generated, then we will see how aXPCS can reveal information on the ionic dynamics in these materials.

M. Ross, *Atomic Diffusion in Glasses Studied with Coherent X-Rays*,
Springer Theses, DOI 10.1007/978-3-319-28646-4_6

6.1 Previous Studies on Amorphous Fast Ionic Conductors

As practical example for fast ionic conductors, alkali borate glasses were studied in this thesis. We will first look into available structural information on this material glass. Then we will learn about previous studies on atomic diffusion in fast ionic conductors.

6.1.1 Structure of Alkali Borate Glasses

We will start by looking into pure borate glass and then see which changes are induced by adding alkali elements to borates.

Borate Glasses

Boron oxide belongs to the longest-known glass-forming materials. It was this glass which was originally described in Zachariasen's glass forming rules (Zachariasen 1932). Since then, it has been subject to numerous studies in various fields.

A very successful model for explaining experimental data on borate glasses was proposed by Krogh-Moe (1969). In this approach, the structure is explained as a random three-dimensional network of planar BO_3 triangles and additional six-membered boroxol rings (B_3O_6). Experimental evidence for this model was found with X-ray and neutron scattering (Mozzi and Warren 1970; Johnson et al. 1982; Hannon et al. 1994). Further experimental sign for the existence of boroxol rings in borate glass is the sharp line at 808 $Å^{-1}$ in the Raman spectrum, interpreted as breathing mode of this six-membered structure (Goubeau and Keller 1953). Likewise, NMR studies support the idea of a local arrangement of boroxol rings and triangular structures (Jellison et al. 1977). Statistical modelling also found a high fraction of boroxol rings in the borate structure (Micoulaut et al. 1995).

While many experimental indications agree well with Krogh-Moe's model, the uniqueness of this solution was challenged by Button et al. (1982). Additionally, some MD simulations claim that no boroxol rings are found in the borate structure (Soules and Varshneya 1981; Xu et al. 1988). In contrast, other MD studies indicate the formation of a large share of boroxol rings in borates (Inoue et al. 1987; Takada et al. 1995; Ferlat et al. 2008).

Alkali Borate Glasses

When adding alkali metals to borate glasses, distinct structural changes occur. The basic building blocks of alkali borate glasses are triangular BO_3 units and tetrahedral BO_4 units, connected by bridging oxygen atoms. The coordination of the building blocks is influenced by the alkali concentration, acting as network modifier (Berkemeier et al. 2005). The formation of BO_4 units can be understood as result of a charge transfer from the alkali atom to the borate building block, leading to a negatively charged borate unit and a positive alkali ion (see Fig. 6.1).

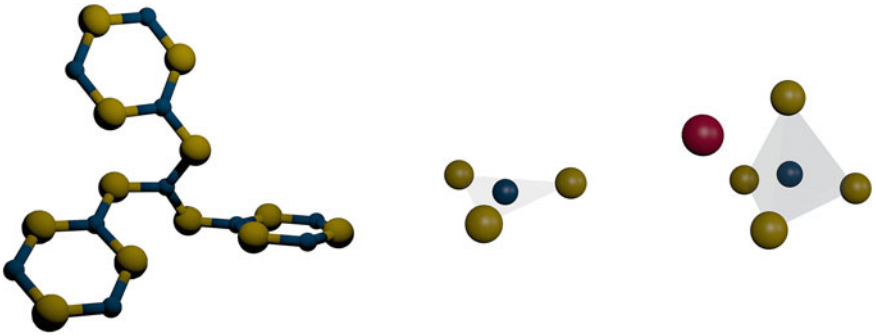

Fig. 6.1 Visualisation of alkali borate structures. The *small blue spheres* represent boron atoms, the *medium yellow spheres* depict oxide atoms and the *red large sphere* represents an alkali atom. *Left* Boroxol rings arranged in three dimensions, connected by a BO_3 triangle. *Middle* BO_3 triangle. *Right* BO_4 tetrahedron, influenced by an alkali ion

The change in coordination is continuous with alkali content until a fraction of $x \approx 30$ mole% (low alkali region) for alkali element A is reached, with $(A_2O)_x(B_2O_3)_{1-x}$. The concentration of boroxol rings decreases simultaneously with the increase in BO_4 units, with absence of boroxol rings when reaching $x \approx 30$ mole%. At a concentration of about 25 mole% alkali oxide content the formation of non-bridging oxygen atoms starts to play an important role in the alkali borate structure (Shelby 2005).

6.1.2 Atomic Dynamics

Several models have been developed to explain the nature of ionic conduction in network glasses. Although ionic conduction in glasses has been studied for many years, there is still no theory which explains all dynamic phenomena. Proposed models range from collective conduction mechanisms to diffusion via vacancies or interstitials (Dyre 2003).

Based specifically on the structural change of the building units of the alkali borate glass network, a model for dynamics of preferred sites was developed. The existence of a site memory effect was proposed (Maass et al. 1992), leading to the formation of conducting pathways. This view was extended in a general model for ionic diffusion in glasses by Bunde et al. (1994), called *dynamic structure model*. The model suggests that ion transport is a hopping process and the moving ions are involved in the glass structure forming, which leads to a changing glass structure even far below T_g. The structural change from BO_3 to BO_4, initially caused by a close-by alkali ion, is retained even when the alkali jumps to another position. This BO_4 unit without any attached alkali ion now poses a preferred site for another alkali ion to jump to. This is due to the fact that no additional energy for a coordination change is required, as opposed to jumping to a BO_3 site and changing it to a BO_4

tetrahedral site. The combination of ion hopping and local structural rearrangement is seen in this model as site memory effect, where the jump process strongly depends on the history of previous jumps and according available empty sites.

With a picture of ionic conduction via vacancies and interstitial sites whose positions freeze at the glass transition, a band gap for ionic-conducting glasses was proposed (Dyre 2003). In this model, two types of sites exist. Many of the sites are filled by modifying ions while others stay empty at the glass transition. Accordingly, it is energetically favourable to stay in or move into a low-energy site. Also based on the existence of distinct sites, an atomic hopping mechanism has been proposed by Elliott et al. (1994). In this model, there are as many ions as sites in the alkali borate glasses, where a site can be unoccupied or occupied by one or two alkali ions. This is in accordance with spectroscopic far infrared studies, which indicate that alkali ions are loosely bound in two distinct network environments (Kamitsos et al. 1990; Kamitsos 1998).

Numerous studies of ionic Alternating Current (AC) and Direct Current (DC) conductivity in fast ionic conductors like alkali silicate and borate glasses have been conducted (Funke 1993; Sidebottom et al. 1995; Roling et al. 1997; Funke et al. 2010). These measurements can be directly related to the ionic dynamics in fast ionic conductors, as these materials are not electronically conducting. Baranovskii and Cordes (1999) analysed extended random barrier and random energy models with a percolative approach, concluding that mobile ions contribute to conductivity by performing hops between localised states in the glass matrix with a rigid potential energy landscape. A strong increase in the DC conductivity with increasing alkali content was observed in alkali borate glasses, indicating that the diffusion changed from individual ion hops to a collective process (Imre et al. 2008). Comparing diffusivities of tracer and conductivity measurements yields the Haven ration. This quantity is a measure for the agreement of both diffusivities and allows to draw conclusions on the correlation and the collective nature of the diffusion process. In many cases, a Haven ratio smaller than 1 is seen as indication for a collective process (Dyre et al. 2009). The combination of both tracer and conductivity measurements was used to gain insight into the diffusion of borate glasses with multiple differing alkali elements and the so-called mixed alkali effect (Voss et al. 2004; Mehrer 2007). It has been found that ionic diffusion is uncorrelated at low alkali content and correlated motion occurs at higher alkali concentrations (Kelly III et al. 1980). Many tracer studies of ionic-conducting glasses have been restricted to the highly mobile ions like sodium, as they depend on the availability of a suitable radioisotope (Shelby 2005).

MC simulations of amorphous ionic conductors with partially immobile ions have shown good agreement with conductivity measurements (Knödler and Dieterich 1992). By a combination of inelastic neutron scattering and MD simulations, a channel formation with alkali-rich preferential ion-conducting pathways has been found (Meyer et al. 2004). Some MD simulations showed that the ionic transport can be described by a noninteracting single-particle process, with ions moving between vacancies (Lammert and Heuer 2010). Also, formation of a network of pockets and channels has been observed with MD, where the atomic motion is not cooperative

but consists of thermally activated hops between the pockets (Jund et al. 2001). Other MD simulations indicate a cooperative motion of diffusing ions and oxygen in glasses, termed as *sliding door mechanism* (Kunow and Heuer 2005).

The influence of Coulomb interaction on the diffusion of ionic conduction has been strongly emphasised by Ngai (1993, 1996). An approach directed at explaining the fast ionic conduction as correlated back-and-forth atomic hopping processes is the so-called *jump relaxation model*. In this model, the glass structure is widely fixed and the dynamics are influenced by relaxations in the ion distributions via Coulomb interaction and caging (Funke 1993). Ion-ion interaction plays an increasing role with increasing density of the alkali ions (Habasaki and Ngai 2006). It has been found that the amount of correlation of the ionic motion can depend on the alkali species (Verhoef and den Hartog 1995). For large ion concentrations transport is thus influenced both by interparticle interaction and the network structure (Kanert et al. 1996).

6.2 Tailoring Atomic Diffusion in Glasses

Many studies have been conducted on the structure of alkali borate glasses and in a broader context on the dynamics of ionic conduction in amorphous materials. Nevertheless, the mechanisms for diffusion on the fundamental level are unclear due to the lack of a suitable method for studying glassy dynamics spatially resolved on the atomic scale. We will now look into the dynamics of ionic jump processes on this very scale both in space and time with the new method of aXPCS and see how dynamics can be understood as an interplay of structural changes and dynamic properties.

In the course of this thesis, aXPCS measurements were carried out on a range of alkali borate glasses. In particular, the caesium borate glasses $(Cs_2O)_2(B_2O_3)_{98}$ and $(Cs_2O)_{15}(B_2O_3)_{85}$, the rubidium borate glasses $(Rb_2O)_2(B_2O_3)_{98}$ and $(Rb_2O)_{15}(B_2O_3)_{85}$, the potassium borate glasses $(K_2O)_5(B_2O_3)_{95}$ and $(K_2O)_{20}(B_2O_3)_{80}$ as well as a sodium borate glass with composition $(Na_2O)_5(B_2O_3)_{95}$ were studied. For a note on the nomenclature, see Sect. 3.1.1. As alkali borates are hygroscopic, they have been kept in vacuum during the measurement and stored in a dry atmosphere at all other times.

6.2.1 Fluorescence: Caesium Borate Glasses

As a first test for investigating into alkali borate glasses, two caesium borate glass compositions $(Cs_2O)_2(B_2O_3)_{98}$ and $(Cs_2O)_{15}(B_2O_3)_{85}$ were studied. Caesium has a much higher X-ray scattering cross section compared to the other elements in the glass matrix, boron and oxygen. Due to L-edges in a range close to (and below) the elastic photon energy utilised, the caesium borate glasses yielded fluorescent inten-

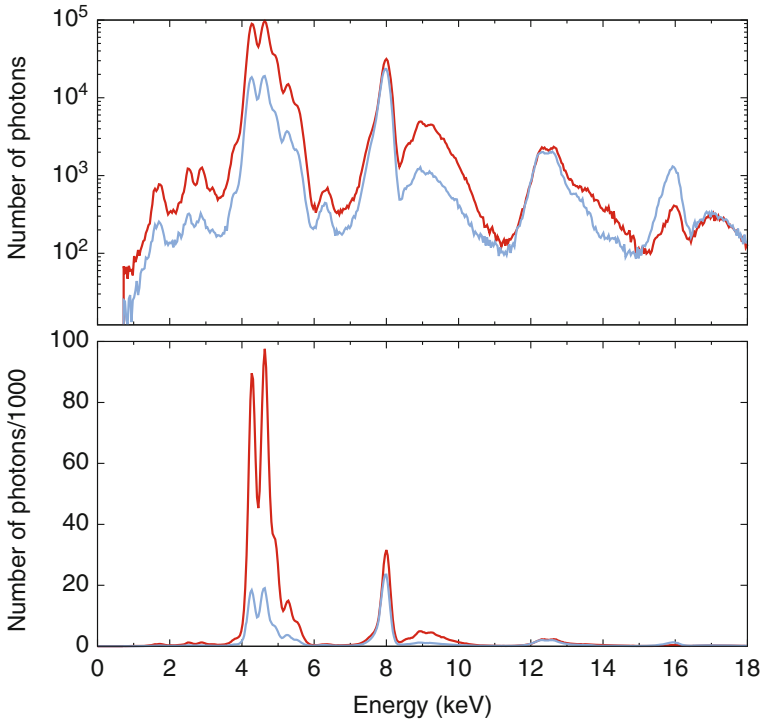

Fig. 6.2 Number of detected photons per energy interval in logarithmic (*upper plot*) and linear scale (*lower plot*). The histogram of the $(Cs_2O)_{15}(B_2O_3)_{85}$ sample is depicted by the *red curve*, the *blue curve* shows the histogram of the $(Cs_2O)_2(B_2O_3)_{98}$ sample. Strong fluorescence peaks are present in both samples

sities. In the histogram of the obtained droplet counts (see Fig. 6.2), the peaks can be assigned to their sources. The elastic peak is located at the elastic photon energy of the synchrotron radiation ($E = 8$ keV). Three fluorescence peaks of Cs can be clearly assigned ($L_{\alpha_{1/2}}$ at 4.3 keV, L_{β_1} at 4.6 keV and L_{γ_1} at 5.3 keV), as well as a shoulder (L_{β_2} at 4.9 keV). Additional peaks are due to the Si fluorescence of about 1.7 keV and Si escape of the elastic photons at $(8 - 1.7 = 6.3)$ keV as well as the Si escape of the Cs fluorescence photons at $(4.3 - 1.7 = 2.6)$ keV and $(4.6 - 1.7 = 2.9)$ keV. The peaks above 8 keV are the instances where multiple photons are detected simultaneously, with fluorescent two-photon peaks around 9 keV, combination of elastic and fluorescent peaks around 12.5 keV and the elastic two-photon peak at 16 keV.

The intensity of the caesium fluorescence was much higher than expected. Although the fluorescence lines of caesium are clearly separable from the elastic signal, their intensity caused too high illumination of the detector to achieve reasonable aXPCS measurements. Attempts to shield the fluorescence photons from reaching the detector using a thin foil did not succeed. In principle, using photons of higher energy and thicker samples, it would be possible to increase the ratio of elasticall

scattered intensity to fluorescent intensity. However, this would in turn decrease the coherence of the scattered radiation due to the higher path length difference. Due to time restrictions at the synchrotron beamtime, the trials with the caesium borates were terminated. Instead, attention was directed to the study of a series of rubidium borates, prepared with differing thermal history.

6.2.2 *Influence of Thermal History: Rubidium Borate Glasses*

To find out if a change in ionic dynamics occurs in glasses having differing thermal histories and if this change depends on the alkali concentration, a series of rubidium borate glasses has been studied.

Samples of two compositions, each with two drastically differing cooling rates from the melt to the vitrified state were prepared for study with aXPCS (see Sect. 3.1.1). The sample compositions were $(Rb_2O)_2(B_2O_3)_{98}$, which will be referred to as low rubidium content glass and $(Rb_2O)_{15}(B_2O_3)_{85}$, which will be referred to as high rubidium content glass. For each composition, one sample was prepared by directly quenching the melt to room temperature, yielding a cooling rate on the order of 10^4 K/min, while the other sample was prepared by cooling from 1273 K to room temperature with decreasing cooling rates on the order of 1 K/min at the glass transition temperature. Altogether, four different rubidium borate glass samples were created and studied.

In trials at different temperatures, the diffusion was found to be very fast even far below room temperature. With the cryostat provided at the PETRA III, temperatures as low as 20 K could be achieved. At this temperatures, dynamics are still surprisingly fast (see Figs. 4.6 and 6.3). It is remarkable that even at these low temperatures significant ionic motion is present.

The intensity autocorrelation function was obtained for several scattering vectors and stretching parameter values were obtained by fitting Eq. (4.4) with a free KWW parameter. The fit yielded KWW values around $\alpha = 0.9$ for all samples. The correlation times were determined by fitting Eq. (4.4) with a free coherence factor β and a KWW parameter $\alpha = 0.9$.

As mentioned in Sect. 2.4.3, the incoherent diffusion models are typically corrected with the short-range order intensity before applying them for data interpretation to the measured coherent inverse correlation times. In the case of lead silicate glasses, this correction was straightforward due to the dominant X-ray scattering cross section of lead compared to the other elements in this glass type. For alkali borates, the situation is much less clear. The contrast between the X-ray scattering cross sections of the elements in these glasses is too low to relate the scattering intensity to a single element. Instead, the partial scattering functions of the studied element would be required for correcting. The immense experimental effort necessary to obtain these partial scattering functions would have gone way beyond the

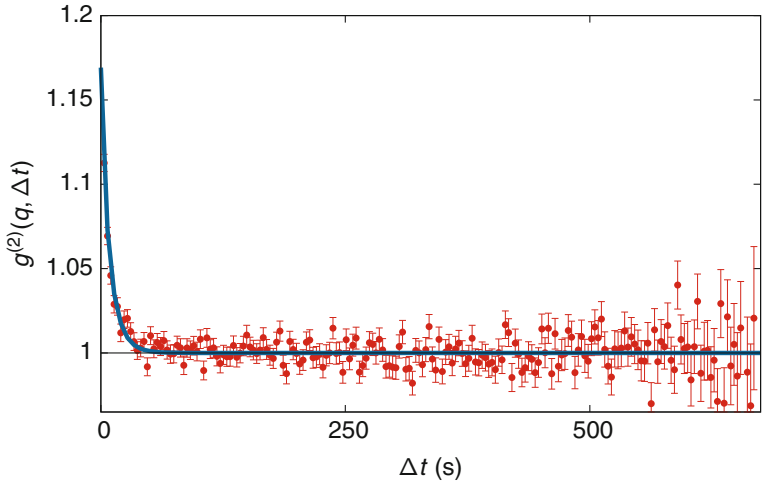

Fig. 6.3 Autocorrelation function $g^{(2)}(q, \Delta t)$ in a fast quenched high rubidium content sample fitted using Eq. (4.4) with the parameter $\alpha = 0.9$. The experimental values were obtained at $q \approx 0.2\,\text{Å}^{-1}$ and $T = 20\,\text{K}$. The baseline at $g^{(2)} = 1$ is shown for comparison

scope of this thesis. Only for few amorphous systems, detailed experimental partial scattering functions have been reported (Meyer et al. 2004; Soper 2005). Note that for the interpretation of the alkali ion mobility in a rigid borate network a partial scattering function S_{AA} is needed, where A is an alkali ion. Preliminary MC simulations done in our group indicate a rather flat partial scattering function for the alkali species under study. This agrees with the X-ray intensity curves obtained for the samples, not showing any indication for a medium range ordering. The remaining partial scattering functions are highly structured (Meyer et al. 2004). With this in mind and taking into account that the fast ionic motion should be significantly faster than the motion of the rigid borate glass matrix, the measured data can be interpreted without correction directly with the incoherent models.

For the lowest q values, the systematic experimental errors are much larger than suggested by the error bars in the graph. To avoid the strong influence of these values on the fit, the lowest q value was not taken into account for each of the fits. The Jobic model shows a very similar plot as the model of uniformly distributed jumps while yielding worse χ^2 values and is thus not considered further.

Low Rubidium Content Glass

For the low rubidium content glass, the single jump Chudley–Elliott model, the two-jump Chudley–Elliott model and the uniformly distributed jump model have been fitted to the data (see Fig. 6.4). The fit of the single jump Chudley–Elliott model yields $l \approx 6(1)\,\text{Å}$ for fast quenching and $l \approx 7(1)\,\text{Å}$ for slowly cooling. As can be seen from the figure, this model only roughly fits the data, with $\chi^2 \approx 5.2$ for fast cooling and $\chi^2 \approx 4.8$ for slowly cooling. The fit of the two-jump Chudley–Elliott model gives $l_1 \approx 3(1)\,\text{Å}$ and $l_2 \approx 8(1)\,\text{Å}$ ($\chi^2 \approx 1.5$) for fast quenching

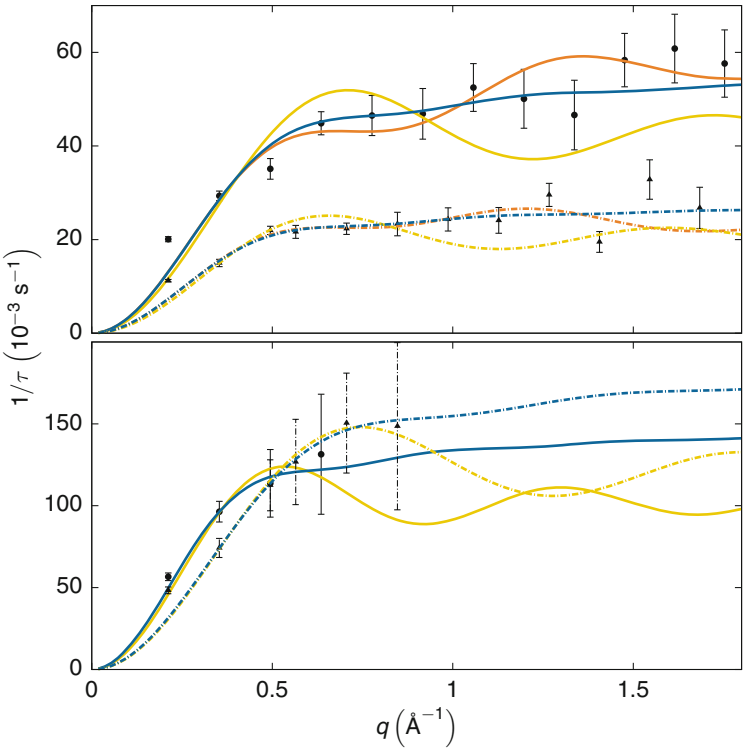

Fig. 6.4 Dependence of the inverse correlation time on the scattering vector q for low rubidium content glass (*upper plot*) and high rubidium content glass (*lower plot*) at 20 K, with fast (*circles*) and slow (*triangles*) quenching. The *curves* show the fit of the single jump Chudley–Elliott model (*yellow*), the two-jump Chudley–Elliott model (*orange*) and the uniformly distributed jump model (*blue*) to the data. For the fast quenched samples, the fits are plotted with *solid lines* and for the slowly cooled samples, they are plotted as *dot-dashed lines*

and $l_1 \approx 4(1)$ Å and $l_2 \approx 9(1)$ Å ($\chi^2 \approx 2.4$) for slowly cooling, each with a jump probability of $\omega_1 \approx 0.5$. This would indicate that both jump lengths occur with the same probability. It is interesting to note that the fit values obtained with the two-jump Chudley–Elliott model are quite close to the structural distances found in a combined RMC and neutron diffraction study of a rubidium borate glass by Cormier et al. (2007), with a distinct cation ordering with Rb–Rb correlations at 4.7 and 7 Å. However, the uniformly distributed jump model yields the best fit, with $l_{\max} \approx 10(1)$ Å ($\chi^2 \approx 1.1$) for fast quenching and $l_{\max} \approx 11(1)$ Å ($\chi^2 \approx 1.7$) for slowly cooling. This indicates that jumps up to about the order of 10 Å occur with equal probability. This agrees well with the image of a flat partial scattering function, hinting at a gas like distribution of the lowly concentrated rubidium in the borate glass matrix.

Comparing the data for fast quenched with slowly cooled low rubidium content glass shows that a remarkable difference in the mean residence times exists. The

mean residence times of the fast quenched sample are all on the same order, with a value of $\tau_0 \approx 17(1)$ s for the uniformly distributed jump model. In the slowly cooled sample the mean residence times are about double as large, with a value of $\tau_0 \approx 35(2)$ s for the uniformly distributed jump model. This is reflected in diffusivities of $D \approx 3.3 \times 10^{-21}\,\mathrm{m^2\,s^{-1}}$ for fast quenched and $D \approx 1.9 \times 10^{-21}\,\mathrm{m^2\,s^{-1}}$ for slowly cooled low rubidium borate glass and indicates that the ionic dynamics in the low rubidium content glass are much faster in the fast quenched sample.

High Rubidium Content Glass

For high rubidium content glass, the number of data points is too low to be fitted reasonably well with the two-jump Chudley–Elliott model. Fitting the single jump Chudley–Elliott model to the data yields $l \approx 8(1)$ Å for fast quenching and $l \approx 6(1)$ Å for slowly cooling. With the uniformly distributed jump model, values of $l_{\mathrm{max}} \approx 13(1)$ Å for fast quenching and $l_{\mathrm{max}} \approx 9(1)$ Å for slowly cooling are obtained. Thus both fits hint at a decrease in the jump lengths when changing from a fast quenched to a slowly cooled sample. However, one should note that the indications of the high rubidium content glass data are much less definite, which is also reflected in χ^2 values far below 1. The mean residence times are in the range of $\tau_0 \approx 5-10$ s.

When comparing the inverse correlation times for slowly cooled and fast quenched high rubidium borate glass, no distinct difference is detectable. Due to the very fast diffusion speeds, measurements at higher q values became increasingly challenging due to the very fast decay of the autocorrelation function (see Fig. 6.3) and the diminishment of contrast (see Fig. 6.5), leading to large measurement errors. Based on the large uncertainties in the obtained data, it seems appropriate to conclude that

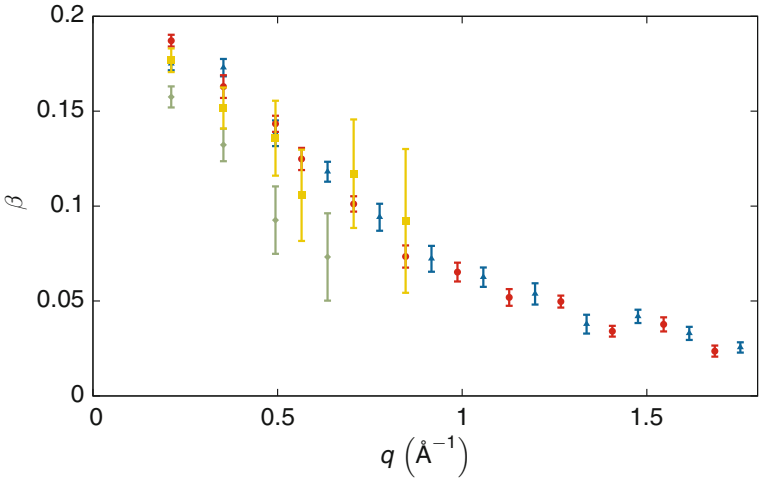

Fig. 6.5 Contrast factor dependence on scattering vector for fast quenched (*blue triangles*) and slowly cooled (*red circles*) low rubidium content borate glass as well as for fast quenched (*yellow squares*) and slowly cooled (*green diamonds*) high rubidium content borate glass

the differences between differing cooling rates are smaller than the experimental errors in the measured high rubidium content samples and that no pronounced change of the diffusion rate between fast cooling and slow quenching at this composition exists.

Comparison of Low and High Rubidium Content Glass

Comparing the low and high rubidium borate glasses reveals a significant difference in the cooling rate dependence. The low rubidium glasses show a much higher diffusion rate for fast quenching than for slowly cooling down. In contrast, the high rubidium content glasses show no indication of a change in the diffusion rate for different thermal histories. A possible way of explaining this behaviour lies in a percolative approach (Baranovskii and Cordes 1999) with hops between localised states in the rigid glass matrix combined with the *site memory effect* proposed by Maass et al. (1992) which is based on the diffusion of ions via preferred sites. If ionic diffusion is in fact dependent on the availability of those sites which are created as an interplay of alkali atoms and the borate structure, one can imagine a freezing-in of ionic arrangements which form a path of closer connected sites than the average ion distance when quenching a melt. In contrast, slowly cooling down allows for the sites to distribute equidistantly in the vitrifying sample. At higher concentrations, the average distance of ions in the melt is already so low that no significantly closer arrangements are possible (see Fig. 6.6). Thus a freezing-in of such structures is not possible anymore and the thermal history has no influence on the diffusion speed.

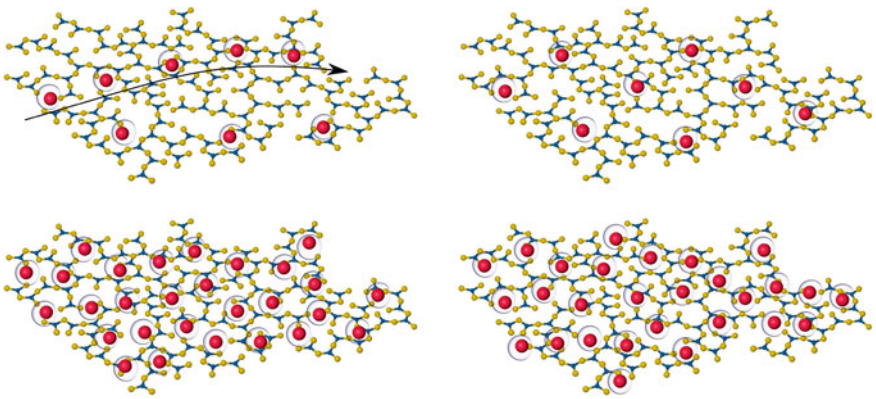

Fig. 6.6 Visualisation of ionic diffusion influenced by the structural arrangement of preferred sites in rubidium borate glass. The preferred sites are marked with transparent *blue spheres*, the *solid red spheres* represent the rubidium ions. For low rubidium content glass which was fast quenched (*upper left*), the preferred sites are stuck at the positions they occupied in the liquid phase. Throughout the glass, random arrangements of these sites exist such that shorter and faster jumps are possible with a lower energy barrier, as depicted by the *arrow*. For the slowly cooled low rubidium content glass (*upper right*), the sites were able to distribute homogeneously across the matrix due to the relaxation during the slow cooling down. For high rubidium content glass (*lower left* and *right*), the concentration of preferred sites has reached a value where larger fluctuations of preferred sites are not possible, independent of the cooling rate

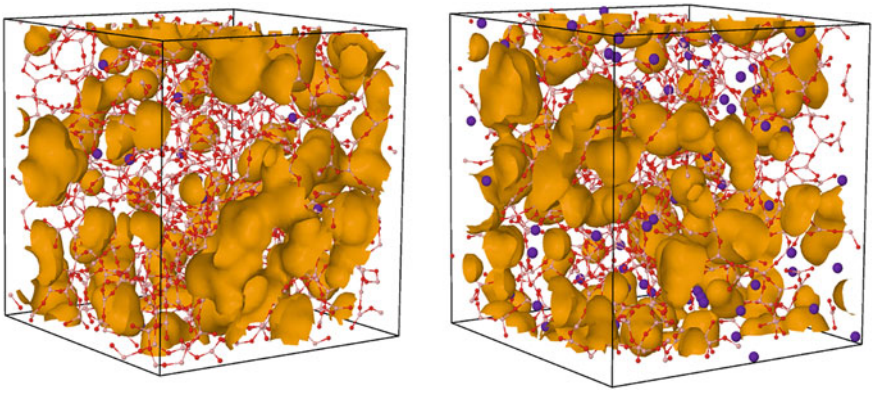

Fig. 6.7 Visualisation of low (*left*) and high (*right*) rubidium content glass structures, based on data of an MC simulation, with rubidium sites (*violet spheres*) in a three-dimensional borate matrix (*red* and *white ball*-and-*stick structure*). Free volume (exaggerated and indicated by *yellow pockets*) can be taken up by alkali ions to form diffusion pathways

Further support for the idea of percolation of ion pathways is given by an extension of the dynamic structure model by Ingram (1999), proposing that the mobile ions capture part of the existing free volume upon vitrification and build this volume into the diffusion pathways. A visualisation of such free volume in low and high rubidium content glass structures simulated with MC in our group is depicted in Fig. 6.7.

Comparing the mean residence times shows that the diffusion in high rubidium content glasses is significantly faster than in the low rubidium content glasses. The KWW parameter of $\alpha = 0.9$ could indicate a correlation of the diffusion, supporting the idea of motion which depends on the availability of vacancy-like sites. However, one should note that the obtained KWW value is subject to the same uncertainties as the inverse correlation times due to the very fast decay of the autocorrelation function even at this low temperature.

The results on rubidium borate glasses presented here show that aXPCS can be utilised to reveal information on atomic-scale motion of fast diffusing ions in glasses even far below the glass temperature and that thermal history can play an important role in the ionic diffusion speed, indicating that the conductivity of some fast ionic conductors can be tuned by the production process. Measurements at even lower temperatures could yield additional insight into the ionic diffusion process.

6.2.3 Path to Light Alkali: Potassium Borate Glasses

Having shown that rubidium diffusion in borate glasses can be studied with aXPCS, the next logical step is to investigate into a similar system with lighter and smaller alkali atoms, which is even more challenging due to the lower difference in electron density of the diffusing alkali species compared to the other elements in the material.

The atomic diffusion in two potassium borate glasses was studied, with compositions $(K_2O)_5(B_2O_3)_{95}$, called low potassium content glass and $(K_2O)_{20}(B_2O_3)_{80}$, called high potassium content glass. As the diffusion was found to be very fast even far below room temperature in the previous rubidium borate glass experiments, measurements on the potassium borate glasses were performed at the same temperature of 20 K, which was the lowest stable temperature achievable with the available cryostat setup.

Similar to the rubidium borate glasses, the intensity autocorrelation functions were acquired for several scattering vectors and stretching parameter values were obtained analogously. The correlation times were determined by fitting Eq. (4.4) with a free coherence factor β and a KWW parameter $\alpha = 0.9$. Fitting with the Jobic model shows a similar plot as the model of uniformly distributed jumps without adding insight for both potassium compositions and is thus not considered further. The τ value obtained in a single measurement for $q = 0.42\,\text{Å}$ was treated as outlier and was not taken into account in the fitting procedure (see Fig. 6.8).

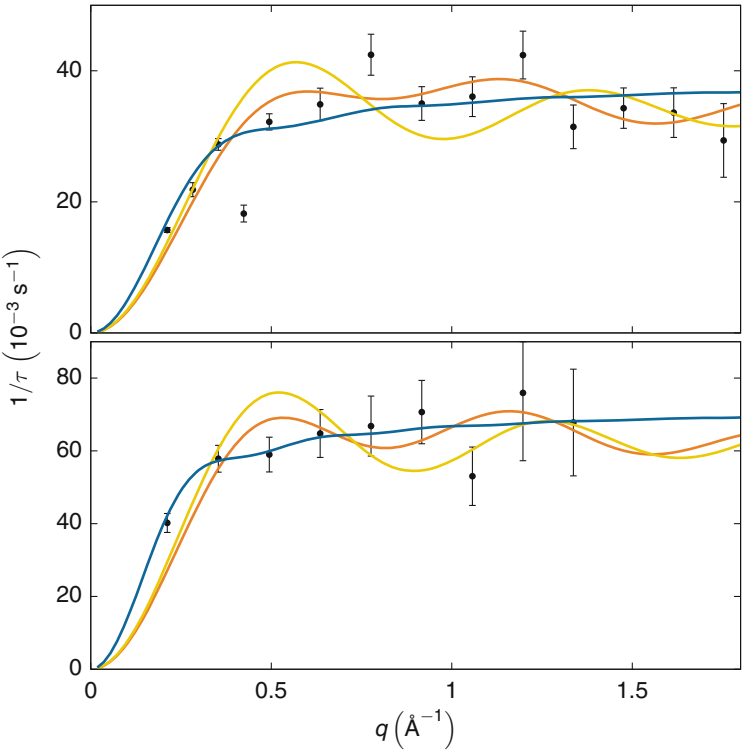

Fig. 6.8 Dependence of the inverse correlation time on the scattering vector q for low (*upper plot*) and high (*lower plot*) potassium content glass at 20 K. The *curves* show the fit of the single jump Chudley–Elliott model (*yellow*), the two-jump Chudley–Elliott model (*orange*) and the uniformly distributed jump model (*blue*) to the data

For the low potassium content glass, the single jump Chudley–Elliott model yields $l \approx 8(1)$ Å. The fit of the two-jump Chudley–Elliott model gives $l_1 \approx 5(1)$ Å with a probability ω_1 of slightly below 50 % and $l_2 \approx 9(1)$ Å. Fitting with the uniformly distributed jump model yields a value of $l_{\max} \approx 16(2)$ Å. The mean residence times are in the range of $\tau_0 \approx 25-30$ s and the diffusivities obtained with the model fits range from about $D \approx 3 \times 10^{-21}\,\mathrm{m^2\,s^{-1}}$ to $D \approx 5 \times 10^{-21}\,\mathrm{m^2\,s^{-1}}$.

In the high potassium content glass, the fit of the single jump Chudley–Elliott gives a value of $l \approx 9(1)$ Å. The fit of the two-jump Chudley–Elliott model yields $l_1 \approx 5(1)$ Å with a probability ω_1 of slightly below 30 % and $l_2 \approx 9(1)$ Å. For the uniformly distributed jump model, the fit yields a value of $l_{\max} \approx 20(3)$ Å. The mean residence times are in the range of $\tau_0 \approx 13-16$ s and the diffusivities range from about $D \approx 7 \times 10^{-21}\,\mathrm{m^2\,s^{-1}}$ to $D \approx 2 \times 10^{-20}\,\mathrm{m^2\,s^{-1}}$.

Based on the data obtained, it is not possible to clearly differentiate between the detailed atomic diffusion mechanisms. However, the single jump process seems least plausible. Also, there is slight indication towards uniformly distributed jumps. Comparing the inverse correlation times of both compositions shows that the diffusion in the high potassium content glass is clearly faster than in the low potassium content glass.

6.2.4 *First Measurement of Light-Alkali Diffusion: Sodium Borate Glasses*

Extending the method to the second-lightest alkali element, a sodium borate glass with composition $(Na_2O)_5(B_2O_3)_{95}$ was studied (Fig. 6.9).

As in the previous alkali borate glass measurements, the intensity autocorrelation functions and stretching parameter values were obtained at a temperature of 20 K. The correlation times were determined by fitting Eq. (4.4) with a free coherence factor β and a KWW parameter $\alpha = 0.9$. Fitting the single jump Chudley–Elliott gives a value of $l \approx 6(1)$ Å and a mean residence time of $\tau_0 \approx 28(2)$ s. In the fit of the two-jump Chudley–Elliott model, the probability of the second jump is practically 0 and the fit shows nearly the same plot as the single jump Chudley–Elliott model. It is thus not shown in the graph. The fit of the uniformly distributed jump model yields a value of $l_{\max} \approx 10(1)$ Å. As can be seen from the fits, the single jump Chudley–Elliott model yields a much more reasonable fit than the equally distributed jump model. This indicates a distinct single jump process. A diffusivity of $D \approx 2 \times 10^{-21}\,\mathrm{m^2\,s^{-1}}$ is obtained with this model.

Thus for the sodium borate sample, the model fits hint at a single jump process. This concurs with results of NMR studies, which indicate that the Na dynamics in low alkali borates ($x < 15$ mole%) below T_g are of nonpercolative nature (Sen and Stebbins 1997).

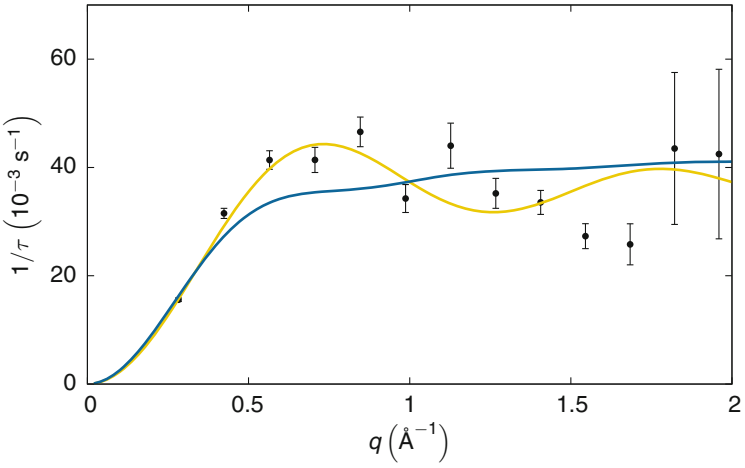

Fig. 6.9 Dependence of the inverse correlation time on the scattering vector for $(Na_2O)_5(B_2O_3)_{95}$ at 20 K. The *curves* show the fit of the single jump Chudley–Elliott model (*yellow*), the two-jump Chudley–Elliott model (*orange*) and the uniformly distributed jump model (*blue*) to the data

Fast atomic rearrangements were reported recently in a study of sodium diffusion in a silicate glass above room temperature by Ruta et al. (2014). Here it is found that in sodium borates, fast atomic diffusion is present even at much lower temperatures.

In an MD study of structural and dynamic properties of lithium and caesium, it was found that the velocities of different caesium ions show much more correlation than those of lithium ions (Verhoef and den Hartog 1995). This suggests a decreasing correlation with decreasing alkali size. Comparing the results of the alkali borate glasses studied in this thesis indicates that with decreasing alkali sizes, the jump process can be described with simpler models. It is interesting to note that no clear trend in diffusivity with decreasing alkali size is detectable. This could hint at competing processes being involved in the diffusion, where smaller ions can squeeze more easily through the network but are more tightly bound to sites than larger ions (Doremus 1994).

On a general level, the diffusion results obtained here show that even far below the glass transition temperature, fast ionic diffusion is present in alkali borate glasses. For a universal description of glassy behaviour, it seems that much deeper insight into the structure of glasses than available nowadays is required.

References

Baranovskii, S. D., & Cordes, H. (1999). On the conduction mechanism in ionic glasses. *Journal of Chemical Physics*, *111*(16), 7546.

Berkemeier, F., Voss, S., Imre, Á. W., & Mehrer, H. (2005). Molar volume, glass-transition temperature, and ionic conductivity of Na- and Rb-borate glasses in comparison with mixed Na-Rb borate glasses. *Journal of Non-Crystalline Solids*, *351*(52–54), 3816–3825.

Bunde, A., Ingram, M. D., & Maass, P. (1994). The dynamic structure model for ion transport in glasses. *Journal of Non-Crystalline Solids*, *172–174*, 1222–1236.

Button, D. P., Tandon, R., King, C., Veléz, M. H., Tuller, H. L., & Uhlmann, D. R. (1982). Insights into the structure of alkali borate glasses. *Journal of Non-Crystalline Solids*, *49*(1–3), 129–142.

Cormier, L., Calas, G., & Beuneu, B. (2007). Structure of single and mixed alkali Li-Rb borate glasses by neutron diffraction. *Journal of Non-Crystalline Solids*, *353*(18–21), 1779–1784.

Doremus, R. H. (1994). *Glass science*. New York: Wiley-Interscience.

Dyre, J. C. (2003). Is there a 'native' band gap in ion conducting glasses? *Journal of Non-Crystalline Solids*, *324*(1–2), 192–195.

Dyre, J. C., Maass, P., Roling, B., & Sidebottom, D. L. (2009). Fundamental questions relating to ion conduction in disordered solids. *Reports on Progress in Physics*, *72*(4), 046501.

Elliott, R. J., Perondi, L., & Barrio, R. A. (1994). Ionic conduction in $(1-x)B_2O_3{+}xLi_2O$. *Journal of Non-Crystalline Solids*, *168*(1–2), 167–178.

Ferlat, G., Charpentier, T., Seitsonen, A., Takada, A., Lazzeri, M., Cormier, L., et al. (2008). Boroxol rings in liquid and vitreous B_2O_3 from first principles. *Physical Review Letters*, *101*(6), 065504.

Funke, K. (1993). Jump relaxation in solid electrolytes. *Progress in Solid State Chemistry*, *22*(2), 111–195.

Funke, K., Banhatti, R. D., Laughman, D. M., Badr, L. G., Mutke, M., Santic, A., et al. (2010). First and second universalities: Expeditions towards and beyond. *Zeitschrift für Physikalische Chemie*, *224*(10–12), 1891–1950.

Goubeau, J., & Keller, H. (1953). Raman-Spektren und Struktur von Boroxol-Verbindungen. *Zeitschrift für Anorganische und Allgemeine Chemie*, *272*(5–6), 303–312.

Habasaki, J., & Ngai, K. L. (2006). Molecular dynamics simulation of ion dynamics in glassy ionic conductors: Evidence of the primitive ion hopping process. *Journal of Non-Crystalline Solids*, *352*(42–49), 5170–5177.

Hannon, A. C., Grimley, D. I., Hulme, R. A., Wright, A. C., & Sinclair, R. N. (1994). Boroxol groups in vitreous boron oxide: New evidence from neutron diffraction and inelastic neutron scattering studies. *Journal of Non-Crystalline Solids*, *177*, 299–316.

Imre, Á. W., Berkemeier, F., Mehrer, H., Gao, Y., Cramer, C., & Ingram, M. D. (2008). Transition from a single-ion to a collective diffusion mechanism in alkali borate glasses. *Journal of Non-Crystalline Solids*, *354*(2–9), 328–332.

Ingram, M. D. (1999). Towards a theory of ion transport in glass. *Physica A*, *266*(1–4), 390–399.

Inoue, H., Aoki, N., & Yasui, I. (1987). Molecular dynamics simulation of the structure of borate glasses. *Journal of the American Ceramic Society*, *70*(9), 622–627.

Jellison, G. E., Panek, L. W., Bray, P. J., & Rouse, G. B. (1977). Determinations of structure and bonding in vitreous B_2O_3 by means of B^{10}, B^{11}, and O^{17} NMR. *Journal of Chemical Physics*, *66*(2), 802.

Johnson, P. A. V., Wright, A. C., & Sinclair, R. N. (1982). A neutron diffraction investigation of the structure of vitreous boron trioxide. *Journal of Non-Crystalline Solids*, *50*(3), 281–311.

Jund, P., Kob, W., & Jullien, R. (2001). Channel diffusion of sodium in a silicate glass. *Physical Review B*, *64*(13), 134303.

Kamitsos, E. (1998). Alkali sites in glass. *Solid State Ionics*, *105*(1–4), 75–85.

Kamitsos, E. I., Patsis, A. P., Karakassides, M. A., & Chryssikos, G. D. (1990). Infrared reflectance spectra of lithium borate glasses. *Journal of Non-Crystalline Solids*, *126*(1–2), 52–67.

Kanert, O., Dieckhöfer, J., & Küchler, R. (1996). Recent progress in the area of NMR characterization of ionic transport and relaxation in glasses. *Journal of Non-Crystalline Solids*, *203*, 252–261.

Kelly, J. E, I. I. I., Cordaro, J. F., & Tomozawa, M. (1980). Correlation effects on alkali ion diffusion in binary alkali oxide glasses. *Journal of Non-Crystalline Solids*, *41*(1), 47–55.

Knödler, D., & Dieterich, W. (1992). Lattice-gas models of dispersive transport in disordered materials. *Physica A*, *191*(1–4), 426–432.

Krogh-Moe, J. (1969). The structure of vitreous and liquid boron oxide. *Journal of Non-Crystalline Solids*, *1*(4), 269–284.

Kunow, M., & Heuer, A. (2005). Coupling of ion and network dynamics in lithium silicate glasses: A computer study. *Physical Chemistry Chemical Physics*, *7*(10), 2131.

Lammert, H., & Heuer, A. (2010). Simplified Interpretation of transport in disordered inorganic ion conductors from vacancy dynamics. *Physical Review Letters*, *104*(12), 125901.

Maass, P., Bunde, A., & Ingram, M. (1992). Ion transport anomalies in glasses. *Physical Review Letters*, *68*(20), 3064–3067.

Mehrer, H. (2007). *Diffusion in solids*. Berlin: Springer.

Meyer, A., Horbach, J., Kob, W., Kargl, F., & Schober, H. (2004). Channel formation and intermediate range order in sodium silicate melts and glasses. *Physical Review Letters*, *93*(2), 027801.

Micoulaut, M., Kerner, R., & dos Santos-Loff, D. M. (1995). Statistical modelling of structural and thermodynamical properties of vitreous B_2O_3. *Journal of Physics: Condensed Matter*, *7*(42), 8035–8052.

Mozzi, R. L., & Warren, B. E. (1970). The structure of vitreous boron oxide. *Journal of Applied Crystallography*, *3*(4), 251–257.

Ngai, K. L. (1993). Difference between nuclear spin relaxation and ionic conductivity relaxation in superionic glasses. *Journal of Chemical Physics*, *98*(8), 6424.

Ngai, K. L. (1996). A review of critical experimental facts in electrical relaxation and ionic diffusion in ionically conducting glasses and melts. *Journal of Non-Crystalline Solids*, *203*, 232–245.

Roling, B., Happe, A., Funke, K., & Ingram, M. (1997). Carrier concentrations and relaxation spectroscopy: New information from scaling properties of conductivity spectra in ionically conducting glasses. *Physical Review Letters*, *78*(11), 2160–2163.

Ruta, B., Baldi, G., Chushkin, Y., Rufflé, B., Cristofolini, L., Fontana, A., et al. (2014). Revealing the fast atomic motion of network glasses. *Nature Communications*, *5*, 3939.

Sen, S., & Stebbins, J. F. (1997). Na-ion transport in borate and germanate glasses and liquids: A ^{23}Na and ^{11}B NMR spin-lattice-relaxation study. *Physical Review B*, *55*(6), 3512–3519.

Shelby, J. E. (2005). *Introduction to glass science and technology*. Cambridge: Royal Society of Chemistry.

Sidebottom, D., Green, P., & Brow, R. (1995). Two contributions to the ac conductivity of alkali oxide glasses. *Physical Review Letters*, *74*(25), 5068–5071.

Soper, A. (2005). Partial structure factors from disordered materials diffraction data: An approach using empirical potential structure refinement. *Physical Review B*, *72*(10), 104204.

Soules, T. F., & Varshneya, A. K. (1981). Molecular dynamic calculations of a sodium borosilicate glass structure. *The Journal of the American Ceramic Society*, *64*(3), 145–150.

Takada, A., Catlow, C. R. A., & Price, G. D. (1995). Computer modelling of B_2O_3. II. Molecular dynamics simulations of vitreous structures. *Journal of Physics: Condensed Matter*, *7*(46), 8693–8722.

Verhoef, A. H., & den Hartog, H. W. (1995). Structure and dynamics of alkali borate glasses: a molecular dynamics study. *Journal of Non-Crystalline Solids*, *182*(3), 235–247.

Voss, S., Imre, Á. W., & Mehrer, H. (2004). Mixed-alkali effect in Na-Rb borate glasses: A tracer diffusion and electrical conductivity study. *Physical Chemistry Chemical Physics*, *6*(13), 3669.

Xu, Q., Kawamura, K., & Yokokawa, T. (1988). Molecular dynamics calculations for boron oxide and sodium borate glasses. *Journal of Non-Crystalline Solids*, *104*(2–3), 261–272.

Zachariasen, W. H. (1932). The atomic arrangement in glass. *Journal of the American Chemical Society*, *54*(10), 3841–3851.

Chapter 7
Conclusion

In this dissertation, the new method of aXPCS was extended to the realm of amorphous materials.

The main goal of this thesis was to show how the atomic movements in glasses can be directly studied with aXPCS. This was achieved by conducting coherent X-ray scattering experiments in two lead silicate glasses with distinctly different mixing ratios, showing how the distances of atomic jumps and the according diffusivities change in this material class with composition. In the lead silicate studies conducted in the course of this thesis, it was found that a split of the dynamics occurs for the different lead compositions investigated. On the one hand, in low lead content glass longer-range single jump processes dominate the atomic motion. On the other hand, in high lead content glass the motion is dominated by at least two different jump processes, one on the short range and at least one other on the long range. This shows that lead diffusion can be envisioned as direct jumps within PbO clusters in low lead content glass and as a combination of short-range movements between connected clusters and longer-range direct jumps through voids in high lead content glass. The clearly recognisable change in atomic motion from a single jump process in low lead content glass to a two-jump process in high lead content glass coincides with the change in structure found by other authors. Two structural features can be deduced from the observed dynamic behaviour. Firstly, the existence of longer-range jumps indicates that a partial lead clustering still exists in high lead content silicate glass, which also results in voids between these clusters. Secondly, the fact that the short-range jumps are much more frequent hint at a percolation of the PbO network structure, which enables short-range diffusion along the strongly connected PbO clusters.

The second goal of this work was to show the practical application of aXPCS to a technically relevant material. The potential future impact of this technique was demonstrated in the study of fast ionic conductors. To gain insight into the very fast ionic diffusion processes, the experimentally accessible range of this method was expanded to very low temperatures, where still surprisingly fast ionic motion was found to be present. This enabled to gain a deeper understanding of the connection between the thermal history and the atomic diffusion mechanism in rubidium borate

M. Ross, *Atomic Diffusion in Glasses Studied with Coherent X-Rays*,
Springer Theses, DOI 10.1007/978-3-319-28646-4_7

glasses. It was shown that for low rubidium concentration, ionic motion depends on the cooling rate upon sample synthesis, which indicates that the conductivity of these materials can be tuned by the production process. This could have potential applications in areas such as energy storage solutions. At higher rubidium concentration, the diffusivities are not influenced by different thermal histories. This behaviour is explained by a percolation process of preferred sites, where random frozen-in percolations during fast quenching lead to higher conductivities at low alkali concentrations, while at higher concentrations the preferred sites are already arranged so tight that larger-scale fluctuations are not possible.

A wide range of elements in different glass systems was studied in this thesis (see Fig. A.11). The results obtained by investigating into the potassium and sodium borate glasses show promise for the feasibility of diffusion studies of very light elements. This pushes open the door for measurements of lithium borate glasses. Such fast ionic conductors are of increasing interest, as they are promising for future battery and energy storage applications. As a general approach, this method also promises to be applicable to a wide range of other fast ionic conductors. Potential future investigations in mixed alkali borate glasses could offer important insight into the conduction mechanism of this material type, which is a long-standing challenge in glass science (Mehrer 2007). The results presented here stress the need for advanced simulations of diffusion in glasses and a deeper structural understanding of glasses on intermediate length scales.

New methods related to XPCS, like X-ray Speckle Visibility Spectroscopy (XSVS) (Inoue et al. 2012; DeCaro et al. 2013) have been developed. There, the contrast visibility of speckles is studied and the exposure time of the frames is varied to gain information on the mean residence time. With this method, one of the main limitations of CCD cameras can be overcome, as it does not depend on the readout time but on shutter speeds, which can in turn be circumvented with the split and delay technique. Studying contrast diminishment in single shot experiments is feasible in new more intense light sources like the XFEL (Gutt et al. 2012; Hruszkewycz et al. 2012). This promises to enable measurements of fast dynamics on previously inaccessible time scales. It can be expected that aXPCS will benefit from the very high degree of coherence in XFEL sources. The pulsed time structure of these sources could provide a useful tool for studying atomic dynamics on very short time scales. However, the short pulse duration combined with the very high energy deposited in the sample will require careful experimentation to avoid shortcomings like sample destruction due to heating by the high-intensity beam. Similar considerations apply to the potential future ERL and DLSR light source projects (Bilderback et al. 2005; Shpyrko 2014). Complementary, faster detectors could expand the range of diffusion ranges accessible for study for aXPCS and thus allow to measure glass forming materials in the solid and the liquid state in a broader range of diffusivities, helping to better understand the atomic mechanisms of glass transition.

References

Bilderback, D. H., Elleaume, P., & Weckert, E. (2005). Review of third and next generation synchrotron light sources. *Journal of Physics B: Atomic, Molecular and Optical Physics*, *38*(9), 773–797.

DeCaro, C., Karunaratne, V. N., Bera, S., Lurio, L. B., Sandy, A. R., Narayanan, S., et al. (2013). X-ray speckle visibility spectroscopy in the single-photon limit. *Journal of Synchrotron Radiation*, *20*(2), 332–338.

Gutt, C., Wochner, P., Fischer, B., Conrad, H., Castro-Colin, M., Lee, S., et al. (2012). Single shot spatial and temporal coherence properties of the SLAC linac coherent light source in the hard X-ray regime. *Physical Review Letters*, *108*(2), 024801.

Hruszkewycz, S. O., Sutton, M., Fuoss, P. H., Adams, B., Rosenkranz, S., Ludwig, K. F., et al. (2012). High contrast X-ray speckle from atomic-scale order in liquids and glasses. *Physical Review Letters*, *109*(18), 185502.

Inoue, I., Shinohara, Y., Watanabe, A., & Amemiya, Y. (2012). Effect of shot noise on X-ray speckle visibility spectroscopy. *Optics Express*, *20*(24), 26878.

Mehrer, H. (2007). *Diffusion in solids*. Berlin: Springer.

Shpyrko, O. G. (2014). X-ray photon correlation spectroscopy. *Journal of Synchrotron Radiation*, *21*(5), 1057–1064.

Appendix A

Technical Drawings of Constructed Experimental Parts and Pictures of Experimental Setups

See Figs. A.1, A.2, A.3, A.4, A.5, A.6, A.7, A.8, A.9, A.10 and A.11.

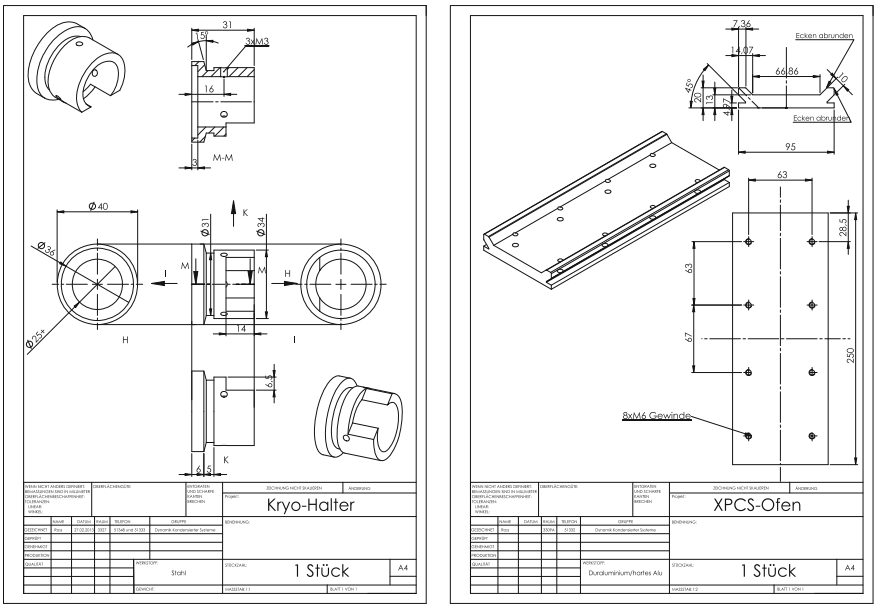

Fig. A.1 Technical drawings of cold finger clamping flange and ESRF adaptor plate

M. Ross, *Atomic Diffusion in Glasses Studied with Coherent X-Rays*,
Springer Theses, DOI 10.1007/978-3-319-28646-4

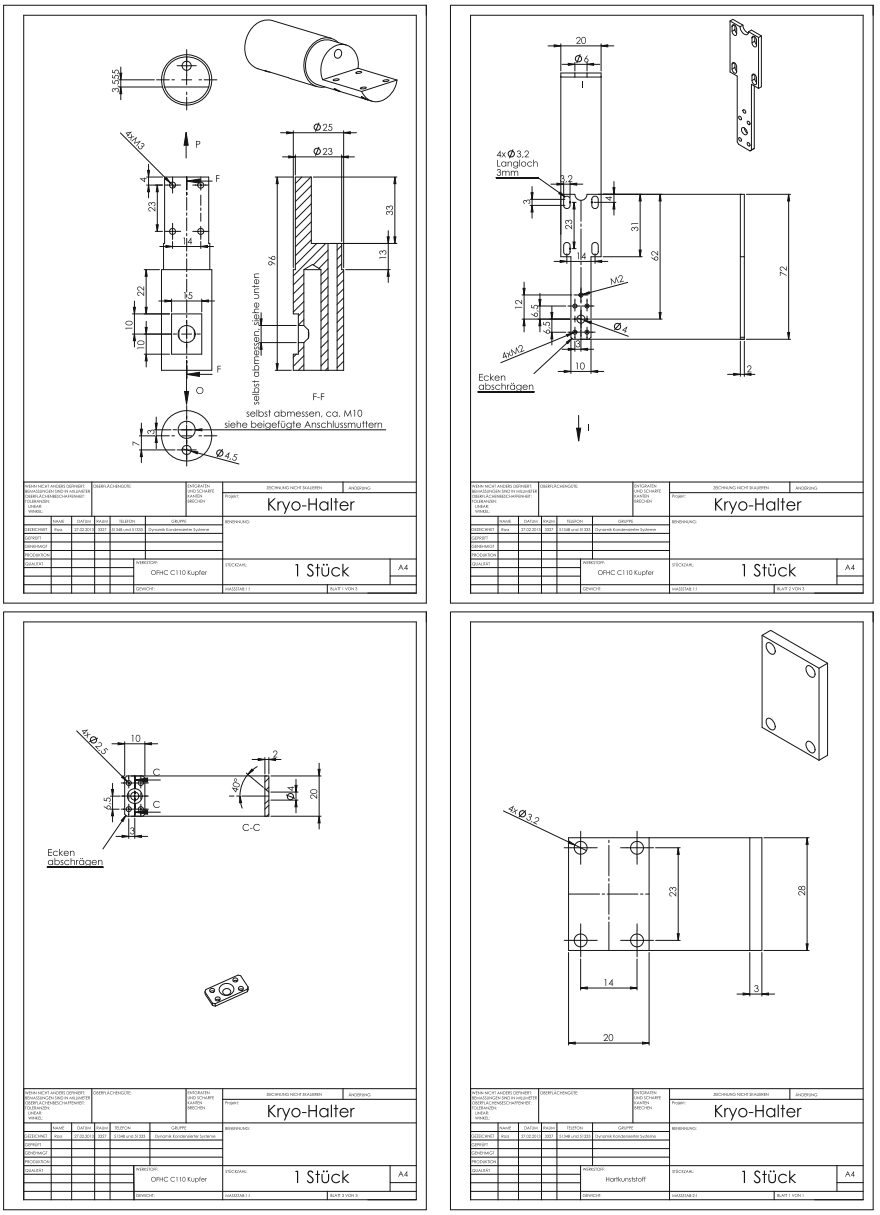

Fig. A.2 Technical drawings of cold finger components

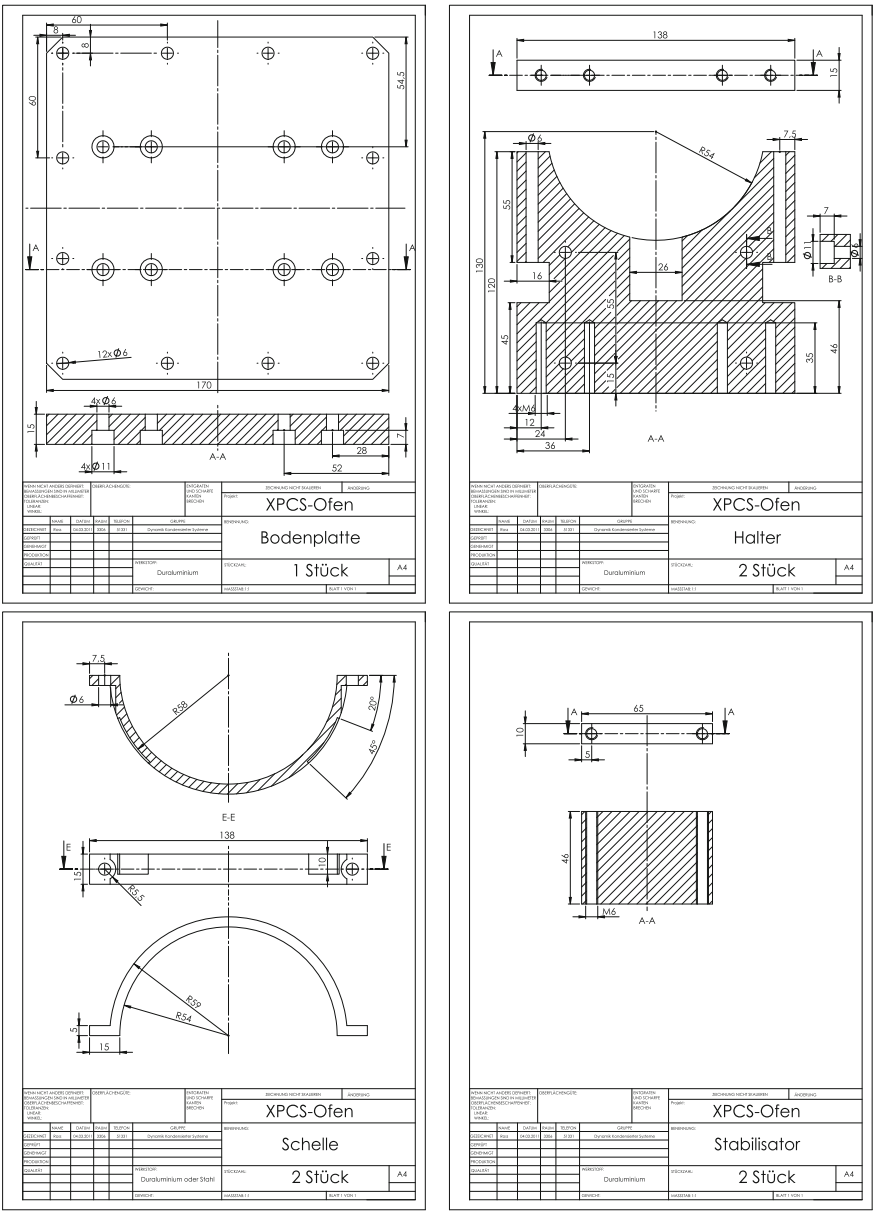

Fig. A.3 Technical drawings of sample cell stage components

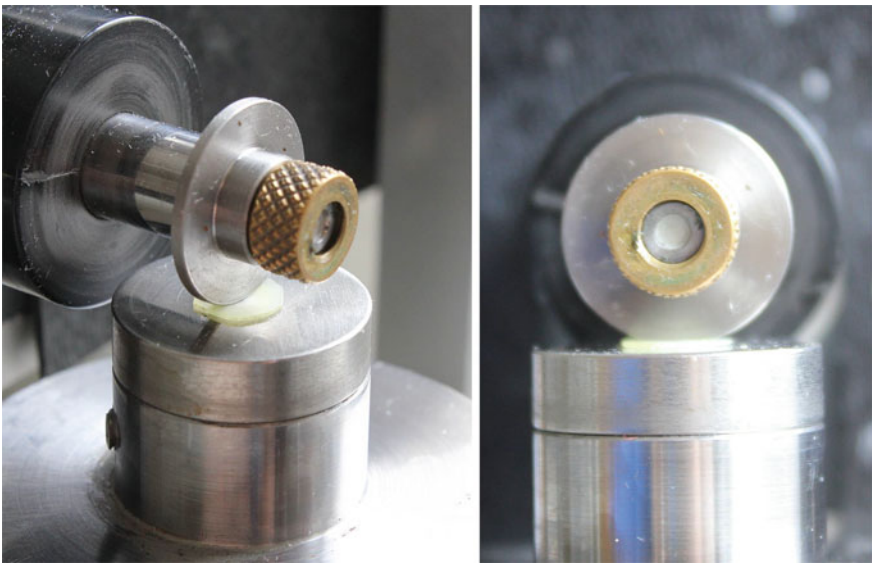

Fig. A.4 Close-up view of dimpling grinder wheel and turning table

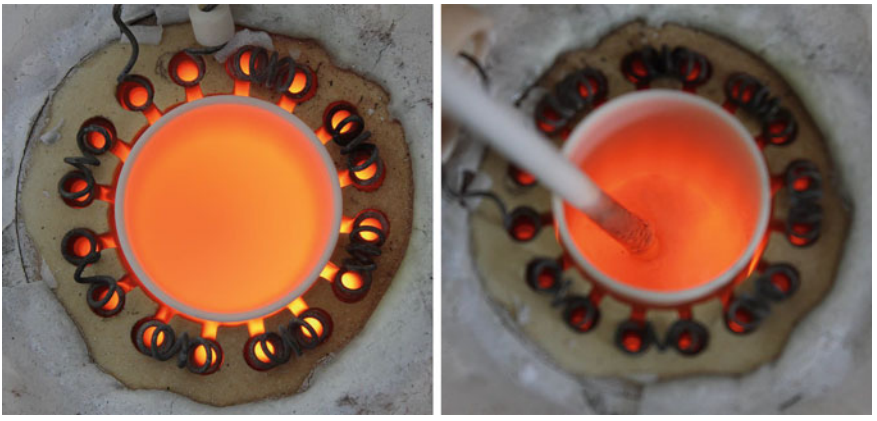

Fig. A.5 Top view on stir furnace. *Left* Pre-heated crucible. *Right* Stirring while melting alkali carbonate powder

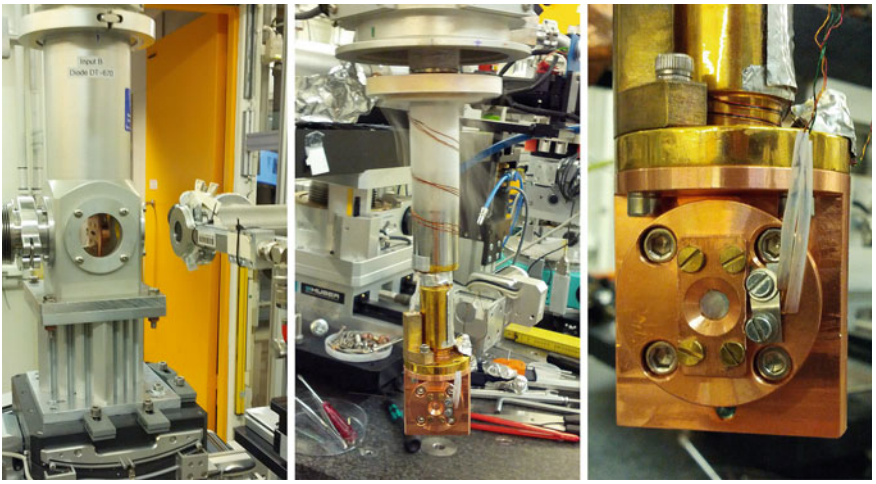

Fig. A.6 Cryostat at PETRA III. *Left* Closed cryostat with mounted sample. *Middle* Cryostat cold finger removed for sample switching. *Right* Close-up view of sample mounted on cryostat cold finger

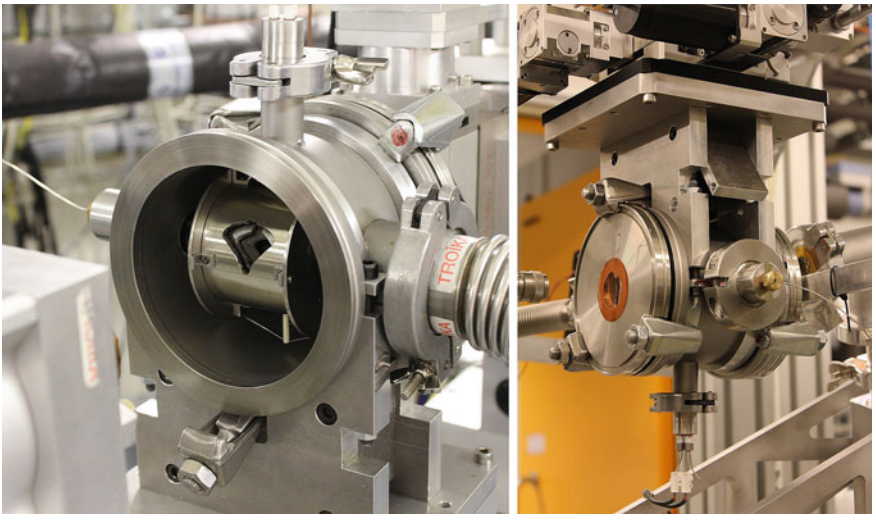

Fig. A.7 *Left* Upright standing opened sample cell setup at the ESRF. *Right* Sample cell in overhead hanging setup at the PETRA III

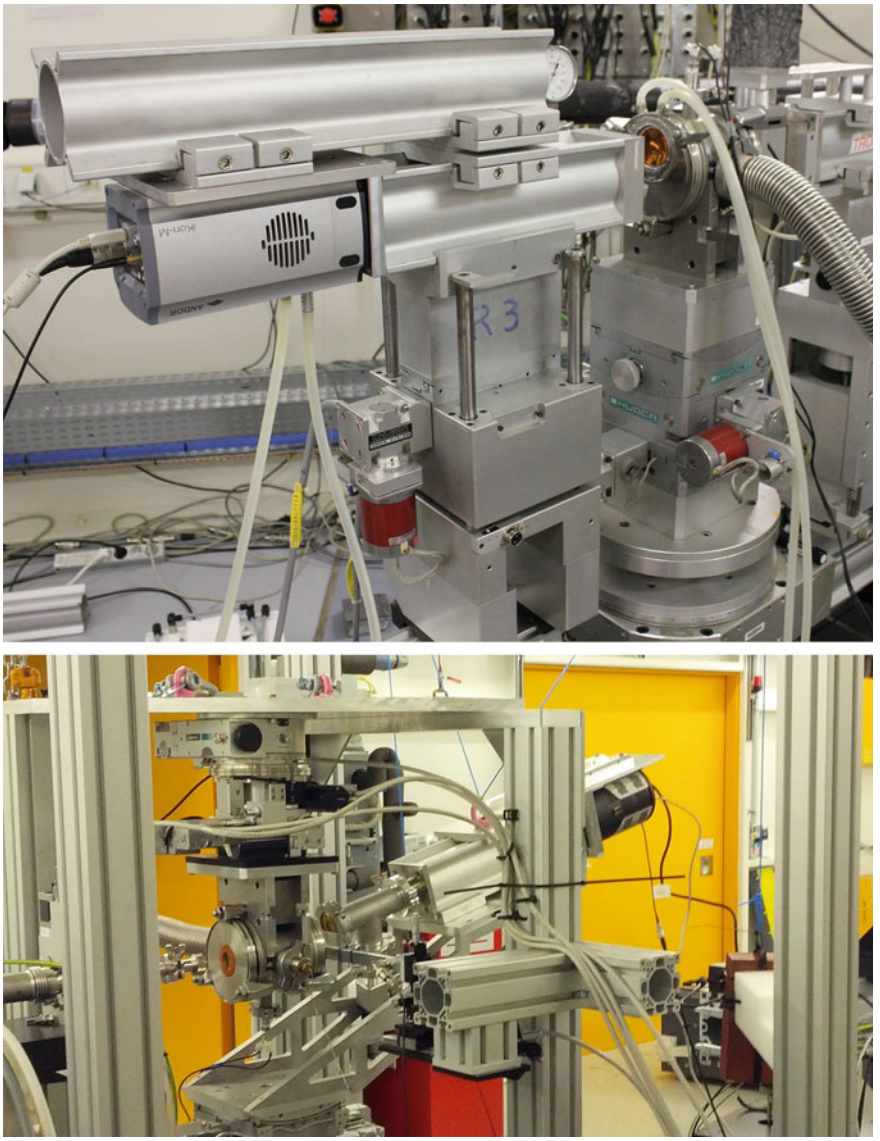

Fig. A.8 Detector and flight tube positioning relative to the sample cell. *Top* Setup at the ESRF. *Bottom* Setup at the PETRA III. The typical distance of the detector from the sample is about 0.5–1 m

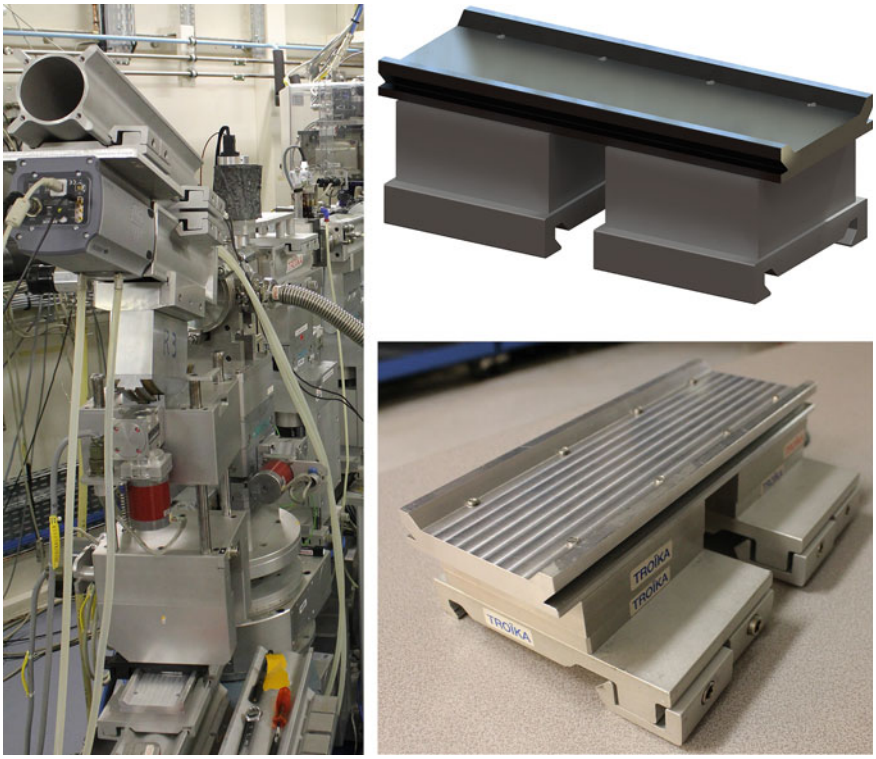

Fig. A.9 *Left* ESRF setup utilising adaptor plate. *Right* Adaptor plate in CAD view and technical realisation

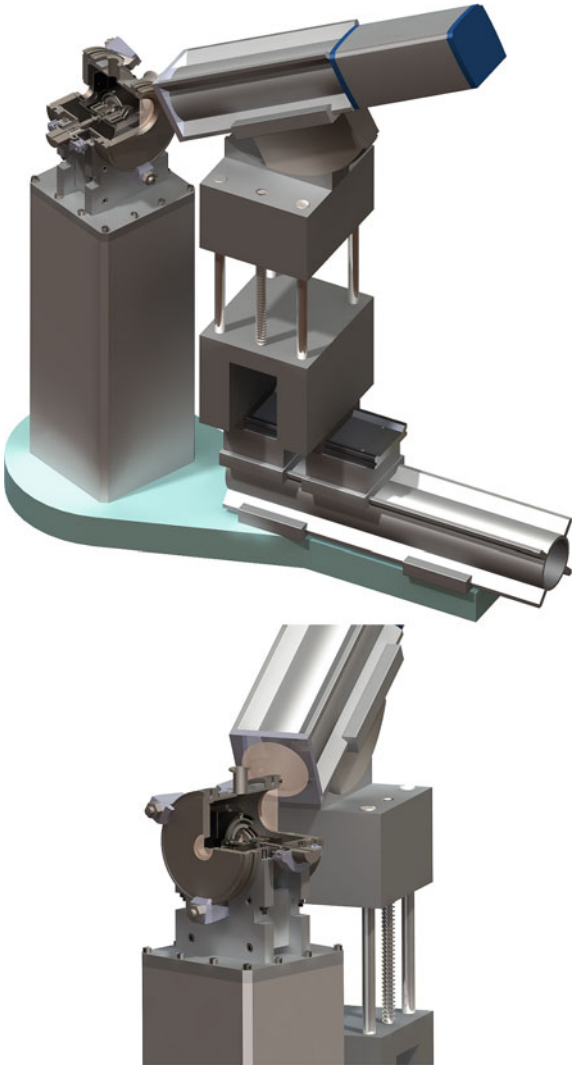

Fig. A.10 CAD renderings of ESRF sample cell and detector setup with sectioned sample cell

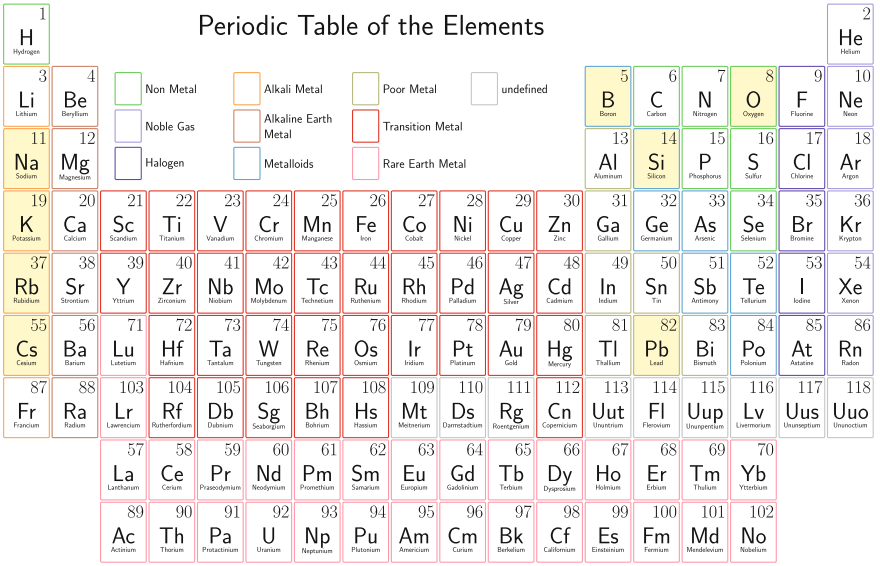

Fig. A.11 Elements studied in the course of this thesis (marked in *yellow*) as components of different glass systems